Bose-Einstein condensates on a magnetic film atom chip

A thesis submitted for the degree of

Doctor of Philosophy

by

Shannon Whitlock

Centre for Atom Optics and Ultrafast Spectroscopy

Faculty of Engineering and Industrial Sciences

Swinburne University of Technology

Melbourne, Australia

Declaration

I, Shannon Whitlock, declare that this thesis entitled:

"Bose-Einstein condensates on a magnetic film atom chip"

is my own work and has not been submitted previously, in whole or in part, in respect of any other academic award.

Shannon Whitlock

Centre for Atom Optics and Ultrafast Spectroscopy
Faculty of Engineering and Industrial Sciences
Swinburne University of Technology
Australia

Dated this day, April 23, 2007

Abstract

Atom chips are devices used to magnetically trap and manipulate ultracold atoms and Bose-Einstein condensates near a surface. In particular, permanent magnetic film atom chips can allow very tight confinement and intricate magnetic field designs while circumventing technical current noise. Research described in this thesis is focused on the development of a magnetic film atom chip, the production of Bose-Einstein condensates near the film surface, the characterisation of the associated magnetic potentials using rf spectroscopy of ultracold atoms and the realisation of a precision sensor based on splitting Bose-Einstein condensates in a double-well potential.

The atom chip itself combines the edge of a perpendicularly magnetised GdTbFeCo film with a machined silver wire structure. A mirror magneto-optical trap collects up to 5×10^8 ^{87}Rb atoms beneath the chip surface. The current-carrying wires are then used to transfer the cloud of atoms to the magnetic film microtrap and radio frequency evaporative cooling is applied to produce Bose-Einstein condensates consisting of 1×10^5 atoms.

We have identified small spatial magnetic field variations near the film surface that fragment the ultracold atom cloud. These variations originate from inhomogeneity in the film magnetisation and are characterised using a novel technique based on spatially resolved radio frequency spectroscopy of the atoms to map the magnetic field landscape over a large area. The observations agree with an analytic model for the spatial decay of random magnetic fields from the film surface.

Bose-Einstein condensates in our unique potential landscape have been used as a precision sensor for potential gradients. We transfer the atoms to the central region of the chip which produces a double-well potential. A single BEC is formed far from the surface and is then dynamically split in two by moving the trap closer to the surface. After splitting, the population of atoms in each well is extremely sensitive to the asymmetry of the potential and can be used to sense tiny magnetic field gradients or changes in gravity on a small spatial scale.

Acknowledgements

During this project I was fortunate enough to enjoy the help and company of many good colleagues and friends who deserve a great deal of thanks.

First of all, I must thank my supervisor Prof. Andrei Sidorov who has provided considerable direction, guidance and encouragement throughout, as well as giving support and insight into all our scientific pursuits: you have been a great instructor. Next I wish to thank the director of our centre and my second supervisor Prof. Peter Hannaford for his amazing commitment to staff and students, his valuable contributions to our work and the support he continues to provide.

It is hard to describe sufficiently the thanks owed to Dr. Brenton Hall, who arrived at Swinburne one year after my start and began us on the path to BEC. Without his sizeable skills and experience I doubt we would have got as far. I will fondly remember our days (and nights) together in the lab. This extends also to Falk Scharnberg, an original member of our BEC on a chip team and someone I will always consider a great friend. Our time constructing and operating the experiment together was most productive and enjoyable.

Next, thanks to the others who I have worked with over the last four years who helped to make this project successful. This has included: Sven Teichmann, David Gough, Dr. James Wang, Prof. Russell McLean, Prof. Timothy Roach, Russell Anderson and Dr. Michael Volk who all deserve credit for their contributions. This must obviously also extend to Mark 'The Magnificent' Kivinen for his technical skills, a man who worked as hard as anyone to get us going and always finished the job long before we knew it was humanly possible.

On a personal note, I wish to acknowledge my friends and family for their understanding on those numerous occasions when I wasn't around. Lastly, a huge thanks goes to my best friend and partner Ange. Your encouragement and support has been invaluable from the very beginning.

Contents

List of Figures

Chapter 1

Introduction

1.1 Bose-Einstein condensation and atom chips

Since the advent of laser cooling techniques in the 1980s, atom optics has emerged as a flourishing and competitive field of research. In particular the ultralow temperatures of laser cooled atom clouds has made it possible to study the wave-like behaviour of matter and realise atom-optical elements, analogous to those used in classical optics for light. A specific method for manipulating and confining laser cooled clouds of atoms involves the interaction between the magnetic moment of an atom and an inhomogeneous magnetic field. Magnetic traps in combination with evaporative cooling techniques finally opened the path to even lower temperatures, at which the atoms can undergo a phase transition to form a Bose-Einstein condensate (BEC), a phase in which a macroscopic number of atoms occupy the same quantum state. The achievement of Bose-Einstein condensation and early fundamental studies of the new state of matter were subsequently recognised through the award of the 2001 Nobel prize in physics [1, 2]. Since that time the field of atom optics has continuously advanced and diversified with an ever increasing variety of atomic and molecular species being cooled to quantum degeneracy, while other experimental efforts have been directed toward developing compact apparatus and robust techniques for creating BECs, and studying the properties of BECs in more intricate and exotic potentials.

As for robustness and portability, the success of microelectronic devices is an

excellent example for scaling down the dimensions of a BEC apparatus and integrating its components. In 1995, the 'atom chip' was proposed as a simple method for confining and manipulating clouds of ultracold atoms within 100 μm of a micro-fabricated surface of conductors [3–5]. These devices exploit the large magnetic field gradients possible near current-carrying wires to produce tightly confining magnetic potentials for creating Bose-Einstein condensates in a compact, robust, versatile and efficient way. Tight traps lead to large elastic collision rates and rapid rethermalisation which allows the evaporative cooling phase to be faster, thereby relaxing the vacuum requirements, decreasing the experimental cycle time and increasing the cooling efficiency to produce larger condensates for the same initial conditions. Furthermore, the close proximity of the atoms to the field sources allows intricate, micron-sized magnetic potentials to be realised. As this length scale is comparable to the typical size of the ground state of a BEC, atom chips open new possibilities for studying the behaviour of quantum systems in custom-made potentials.

Bose-Einstein condensates were first produced using atom chips in 2001 by the groups of T. Hänsch [6] and C. Zimmermann [7] and now there are more than 20 active BEC on a chip experiments world wide. These experiments are aimed at a range of topics which include: the realisation of microfabricated atomic waveguides and transport devices for BECs [8–10], BEC in a portable vacuum cell [11], quantum degenerate Fermi gases and atomic mixtures [12], the integration of sensitive or minimally destructive detection techniques [13], novel magnetic field microscopy using BECs [14], and the demonstration of on-chip atom interferometry based on coherently splitting a single BEC in a double-well potential [15, 16].

Although this is an already impressive list of achievements, several limitations currently challenge the true potential of atom chips. In particular, small spatial deviations in current-flow cause fragmentation of ultracold atom clouds within about 100 μm of the wire surface [8, 17]. This was subsequently traced to small imperfections in the current-carrying wires [18, 19]. Although a lot of work has already been done to minimise this effect through high quality fabrication techniques [20, 21], new limits

to the quality of wires may be due to impurities or the granular structure of the conducting metal itself [20]. Recently, dynamic methods to suppress fragmentation have been applied with some success by modulating the wire current [22]. In addition to fragmentation, thermal current fluctuations associated with Johnson noise in the conductors are responsible for a fundamental loss mechanism when atoms are moved closer to the surface [23, 24]. This effect may be reduced by keeping the wires thin and by optimising the type of conducting material; however the best results are expected for non-conductors [25]. As a possible solution to some of the problems associated with current-carrying wires we are investigating permanent magnetic materials for use on atom chips.

1.2 Permanent magnet atom chips

The advantages of permanent magnet atom chips are both technical and scientific in nature. Specifically, permanent magnet atom chips:

- require no resistive power dissipation, which for wires operated at high current density can cause excessive heating, broken circuits and current leakage,
- lack technical current noise which minimises in-trap heating and loss of atoms and extends the lifetime of a trapped BEC,
- can be patterned using well known and established microfabrication techniques such as metal vapour deposition, lithography, ion beam milling and laser ablation, but also have the potential to be written and re-written using magnetic heads or magneto-optical recording techniques,
- provide large magnetic field gradients allowing tight confinement and access to low-dimensional regimes, opening the possibility of exploring new physics,
- are typically thin and relatively high in resistance, two properties known to suppress thermal Johnson noise,

- do not require electrical lead wires, allowing unique magnetic field geometries to be produced such as large arrays of microtraps or ring-shaped potentials, and
- allow new and precise measurements of atom-surface interactions near magnetic materials.

In 2005 two groups succeeded in producing Bose-Einstein condensates using permanent magnet atom chips as an alternative to current-carrying wires alone. In the group of Prof. E. A. Hinds, the atom chip consists of a sinusoidally magnetised video tape [26,27]. Atom clouds trapped near the video tape were shown to have long lifetimes due to the inherently low Johnson noise in the non-conducting surface [27]. Soon after, Bose-Einstein condensates of rubidium 87 atoms were produced using a magnetic film atom chip at Swinburne University of Technology in Melbourne [28, 29]. For this project we used a perpendicularly magnetised GdTbFeCo film which was tailor made for the application [30]. Since then, Bose-Einstein condensates have also been produced in the group of Prof. D. E Pritchard near a periodically magnetised film [31], and in the group of Prof. R. J. C. Spreeuw using a magnetic foil structure as a self-biased magnetic trap. Interestingly, the above magnetic atom chip experiments have all indicated the presence of significant fragmentation, most-likely caused by variations of the material magnetisation rather than imperfect patterning; a topic thoroughly investigated in this project. In addition to these experiments, permanent magnet atom chips have also been built using transparent materials to combine magnetic and optical potentials [32] and using soft magnetic materials in combination with current-carrying sheets to allow dynamic control of the magnetic potentials [33].

1.3 Organisation of the thesis

This thesis describes the implementation of the first magnetic film atom chip and experiments with ultracold atoms and Bose-Einstein condensates near the film surface. The experimental apparatus and the atom chip were newly developed, and the proceeding experimental results were obtained during this PhD work and are therefore

described in detail. The text consists of three main parts: the introductory section (Chapters 1 and 2), a technical section (Chapters 3 and 4) and an experimental section (Chapters 5, 6 and 7). The specific content of each chapter is outlined here.

In Chapter 2 the principle of magnetostatic trapping of neutral atoms is introduced with particular emphasis on permanent magnetic microtraps. The magnetic film microtrap used in the following experimental studies is introduced here. The magnetic field produced near the edge of the magnetic film and the associated magnetic trapping potentials are derived. A summary of important thermodynamic properties of ultracold atom clouds is given as a reference for later chapters. This includes the use of the Boltzmann distribution function to calculate static and dynamic properties of the cloud. The chapter ends with some background theory of Bose-Einstein condensates in magnetic microtraps which is used in the experimental chapters.

The development, construction and characterisation of the magnetic film atom chip is described in Chapter 3. A high quality GdTbFeCo film is deposited on a specially prepared substrate for the atom chip. Analysis indicates the film has high remanent magnetisation, high coercivity, high perpendicular anisotropy and excellent homogeneity. The magnetic film is then combined with a machined current-carrying wire structure to complete the atom chip. The wire structure is necessary to load laser cooled atoms into the magnetic microtrap and as a radio frequency (rf) antenna for evaporative cooling (described in Chapter 5) and for spatially resolved rf spectroscopy of ultracold atoms used to profile small magnetic field variations; a new technique introduced in Chapter 6.

In Chapter 4 a summary is given of the apparatus and techniques used for studying laser cooled and magnetically trapped atom clouds. This includes details of the ultra-high vacuum (UHV) chamber, the optical setup used to laser cool the atoms, the high resolution imaging system and computer control for synchronising of the experiment.

Chapter 5 describes the steps taken to produce and characterise Bose-Einstein condensates created using the atom chip. This includes a laser cooling stage, loading and compression of the magnetic trap, the forced rf evaporative cooling stage and the

transfer of atoms to the magnetic film microtrap. Bose-Einstein condensates can be produced using the current-carrying wire structure or the magnetic film microtrap, allowing a direct comparison between the two technologies. The magnetic field produced by the film is characterised using the BEC as a probe and is in good agreement with the model presented in Chapter 2.

A quantitative study of the fragmentation of ultracold atoms in the magnetic film microtrap is presented in Chapter 6. Fragmentation is caused by a random magnetic field component near the film surface that corrugates the potential. A new technique which incorporates radio frequency spectroscopy and high resolution optical imaging of the atoms is applied to accurately profile the magnetic field landscape. The results indicate that the variations originate from long range inhomogeneity in the film magnetisation. A model which takes into account two-dimensional random variations of the film magnetisation is developed and compared with the observations. After these measurements the atom chip is removed from the vacuum chamber and analysed using a magneto-resistive probe which supports the experimental findings.

Chapter 7 deals with experiments involving Bose-Einstein condensates in a double-well potential identified at the central region of the corrugated potential. A single condensate is produced far from the film surface and is then dynamically split by moving the trap closer to the surface. After splitting, the relative population of atoms in each well is extremely sensitive to small magnetic field gradients and can be applied to sense tiny gravitational forces on a small spatial scale. The experimental results can be understood through a simple steady-state model for the probability distribution of the split condensate.

Chapter 2

Ultracold atoms and magnetic microtraps

In this chapter a theoretical framework is provided with emphasis on the concepts relevant to the proceeding experimental chapters. Specific attention is paid to magnetostatic trapping of neutral atoms. We then introduce the permanent magnetic film microtrap which is used in experimental studies throughout this thesis. The magnetic field produced near the edge of the film is first derived and some details on the associated magnetic potentials are provided. The chapter finishes with a summary of important thermodynamic properties of ultracold atom clouds and the relevant theory of Bose-Einstein condensates in magnetic microtraps.

2.1 Magnetostatic trapping of neutral atoms

Magnetic trapping of neutral atoms was first proposed in the early 1960s after pioneering work on focusing cold neutral atom beams by means of the Stern-Gerlach force (see [34] for a historical perspective). This relatively weak force originates from the interaction between the magnetic moment of an atom and a non-uniform magnetic field. The first magnetic trap for neutral atoms was made in 1985 [35], soon after the development of modern laser cooling techniques. Laser cooled atom clouds have sufficiently low energy that their motion is strongly affected by modest laboratory magnetic fields. The magnetic contribution to the potential energy of an atom at position x, y, z, to first order, is simply equal to the effective magnetic moment times

the magnitude of the local magnetic field [36],

$$U(x, y, z) = m_F g_F \mu_B |B(x, y, z)|, \tag{2.1}$$

where m_F is the magnetic quantum number, g_F is the Landé g factor for the atomic state and μ_B is the Bohr magneton. The potential energy of an atom with magnetic moment anti-aligned with the local magnetic field ($m_F g_F > 0$) increases with increasing field strength and the atom can therefore be confined at a minimum of the magnetic field. To magnetically trap neutral atoms for long periods of time it is important that the magnetic state of the atoms is preserved. Throughout this thesis we deal with ^{87}Rb atoms in the $|F = 2, m_F = +2\rangle$ magnetically trapped state ($m_F g_F = +1$).

The simplest magnetic field configuration for confining neutral atoms is realised with a quadrupole trap [35, 37, 38], produced for example between two parallel coils carrying current in opposite directions. The field from the coils cancels to zero at the centre and the amplitude of $|B|$ increases linearly with distance in all directions. The most significant limitation of the quadrupole magnetic trap is that the atoms can undergo non-adiabatic transitions to untrapped magnetic states due to orbital motion [39]. The magnetic moment of an atom precesses around the magnetic field at the Larmor frequency given by $\omega_L = m_F g_F \mu_B B/\hbar$. If this frequency is not large compared to the rate at which the magnetic field changes with respect to the moving atom then there is a large probability of a spin-flip transition to an untrapped magnetic state resulting in loss from the trap. The transition probability is therefore high at the centre of a quadrupole trap in the vicinity of the zero field ($\omega_L \to 0$). For ultracold atoms with temperatures in the microkelvin regime, spin-flip loss typically limits the trap lifetime to several seconds [40–42].

To avoid this problem more advanced magnetic field configurations can be devised such as the Ioffe-Pritchard trap potential [37, 43]. The standard Ioffe-Pritchard trap consists of four 'Ioffe bars' in combination with two pinch coils. The bars produce a two-dimensional quadrupole field geometry and the pinch coils add a non-uniform field oriented along the length of the bars to complete the full three-dimensional trap. The

field of the pinch coils defines the magnetic field minimum B_0, from which $|B|$ increases approximately quadratically to provide harmonic confinement of the atoms.

The spin-flip loss rate for a cloud of atoms in the ground state of a harmonic magnetic trap with a non-zero field minimum and the subsequent generalisation to a thermal Boltzmann distribution at temperature T has been calculated by Sukumar and Brink [44]. While at zero temperature this loss rate can be made negligibly small, in the high temperature limit ($\frac{1}{2}k_BT > \hbar\omega$) the spin-flip transition rate Γ can be significant

$$\Gamma \simeq \frac{\pi\hbar\bar{\omega}^2}{k_BT}\,\exp\!\left(-\frac{2m_Fg_F\mu_BB_0}{k_BT}\right), \tag{2.2}$$

where $\bar{\omega}$ is the mean trap frequency and T is the cloud temperature. For some typical experimental parameters: a cloud of ^{87}Rb atoms in the $|F = 2, m_F = 2\rangle$ state with $T = 10$ μK and $\bar{\omega} = 2\pi \times 100$ Hz has a spin-flip limited trap lifetime of $\Gamma^{-1} \approx 60$ s for $B_0 \simeq 0.03$ mT. For tighter traps with $\bar{\omega} \sim 2\pi \times 1000$ Hz, and higher cloud temperatures $T > 15$ μK, the field strength at the trap bottom may need to be increased to $B_0 > 0.1$ mT to maintain an equivalently long trap lifetime.

In addition to spin-flip transitions, the magnetic trap lifetime is affected by several other loss mechanisms. The three main mechanisms are inelastic collisions with background gas atoms, dipolar relaxation and three-body recombination. Dipolar relaxation is suppressed for a spin-polarised sample in the $|F = 2, m_F = 2\rangle$ [45], whereas the two other loss mechanisms can be significant.

When a cloud of laser cooled atoms is transferred to a magnetic trap the dominant loss mechanism is typically through collisions with room temperature background gas atoms. The background collision rate scales linearly with background pressure and is independent of the atomic density, causing the number of trapped atoms to decay exponentially over time (Figure 2.1). If we assume the background vapour consists mainly of residual Rb atoms then the the loss rate is $\Gamma_{bg} \approx n_{bg}\,\sigma_{Rb}\,\sqrt{2k_BT/m}$. For an ideal gas the background atom density $n_{bg} = {}^{P}\!/_{k_BT}$ depends on the pressure P and temperature T. The background total collision cross section for Rb, assuming $T = 300$ K, is $\sigma_{Rb} \approx 2.5 \times 10^{-13}$ cm^2 [46]. For a pressure of $P = 2 \times 10^{-11}$ Torr the

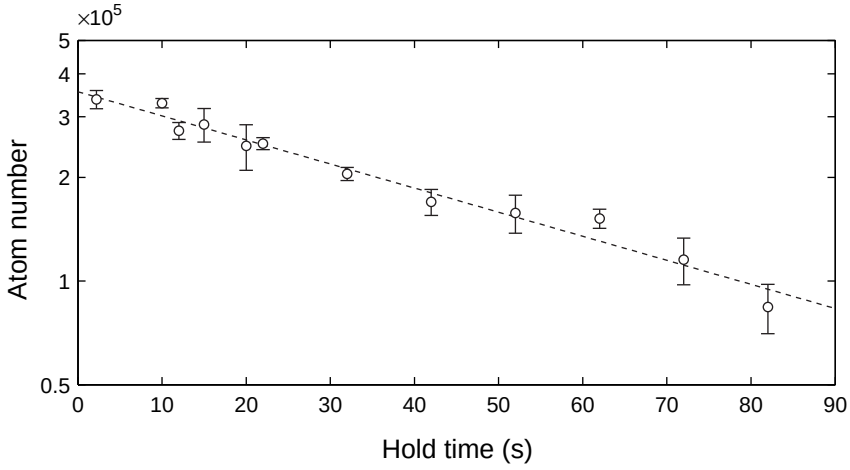

Fig. 2.1: Exponential decay of atoms held in a magnetic film microtrap positioned 200 μm from the surface for $\bar{\omega} = 2\pi \times 50$ Hz. The dominant cause of loss is collisions with residual ^{87}Rb atoms in the hot background vapour. The exponential fit (dotted line) indicates a trap lifetime of $\Gamma^{-1} = 60$ s.

background collision limited lifetime is around 250 s.

Once the atoms are magnetically trapped it is possible to begin evaporative cooling. This lowers the cloud temperature and increases the cloud density to the point where three-body recombination may dominate the loss rate. Three-body losses are proportional to the average atomic density squared $\Gamma = K_3\langle n^2\rangle$, where $K_3 = 4.3\times10^{-29}$ cm^{-6}s^{-1} is the three-body rate constant for ^{87}Rb [47] and for a harmonically trapped thermal cloud $\langle n^2\rangle = n_0^2/3\sqrt{3}$ where n_0 is the peak atomic density. We find that at the beginning of the evaporative cooling stage $n_0 = 1.5 \times 10^{12}$ cm^{-3} and the three-body lifetime is $\Gamma^{-1} \approx 5.4 \times 10^4$ s. For temperatures approaching the BEC transition however ($T \approx T_c$) the peak atomic density is much higher $n_0 = 1.0 \times 10^{14}$ cm^{-3} and three-body loss dominates over other loss processes $\Gamma^{-1} \approx 10$ s. For a Bose-condensed gas the three-body rate constant is a factor of 6 smaller due to higher order coherence [48], but the associated high density of a Bose-Einstein condensate can result in lifetimes of only a few seconds. A more complete overview of loss and heating mechanisms for magnetically trapped atom clouds can be found in [49].

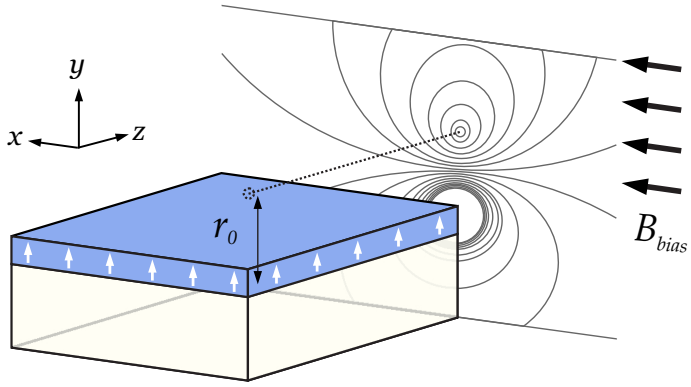

Fig. 2.2: (Colour) The magnetic field produced by a perpendicularly magnetised half-plane thin film in combination with a uniform bias magnetic field, B_{bias}, creates a magnetic minimum for confining ultracold atoms.

2.2 Magnetic film microtraps

For efficient evaporative cooling it is necessary to produce tightly confining magnetic traps which increase the inter-atomic collision rate and allow rapid thermalisation. Simple scaling arguments can be used to show that tight magnetic traps can be realised by miniaturising the magnetic field producing elements and bringing the atoms close to the field source [3]. This concept ultimately led to the development of 'atom chips' where planar geometries of microfabricated current-carrying wires are designed to trap and manipulate laser cooled clouds of atoms in close proximity to a surface [50–52]. A basic trap configuration makes use of the large field gradient produced by a current-carrying wire in combination with a homogeneous bias magnetic field to produce a very tight and elongated potential. Atom chips can also be implemented using permanently magnetised materials [26,28,29]. We focus specifically on the magnetic micro-potentials formed by high quality perpendicularly magnetised magnetic films [30, 53].

Consider a semi-infinite magnetic film of thickness δ lying in the $x-z$ plane with one edge aligned along the z axis at $x = y = 0$ (Figure 2.2). The associated magnetic field can be obtained through evaluation of the magnetic scalar potential Φ [54], which

is related to the magnetisation $\boldsymbol{M}$ by

$$\Phi(\boldsymbol{r}) = -\frac{\mu_0}{4\pi}\int_V d^3r' \frac{\nabla' \cdot \boldsymbol{M}(\boldsymbol{r}')}{|\boldsymbol{r}-\boldsymbol{r}'|} + \frac{\mu_0}{4\pi}\oint_S \frac{\boldsymbol{M}(\boldsymbol{r}')}{|\boldsymbol{r}-\boldsymbol{r}'|}\, da', \tag{2.3}$$

where V and S are the volume and surfaces of the film respectively, $\boldsymbol{r}' = \{x', y', z'\}$ denotes the coordinate within the film and $\boldsymbol{r}$ is the free space co-ordinate. The film is assumed to be uniformly magnetised perpendicular to the film surface $M(x, y, z) = M_y$ such that the first term vanishes, leaving only a surface integral that simply involves the difference between the magnetic field contributions from the top and bottom surfaces of the film,

$$\Phi(x, y, z) = -\frac{\mu_0}{4\pi}\int_0^{+\infty} dx' \int_{-\infty}^{+\infty} dz' \frac{M_y}{\sqrt{(x-x')^2 + (y-y')^2 + (z-z')^2}}\Bigg|_{y'=-\delta}^{y'=0}. \tag{2.4}$$

A Taylor series expansion is first performed by assuming that the film thickness is small compared to the distance from the surface ($\delta \ll y$). The integrals can then be evaluated to give

$$\Phi(x, y, z) = -\delta M_y\big[\pi + 2\arctan(x/y)\big], \tag{2.5}$$

with the magnetic field components given by $\boldsymbol{B} = -\nabla\Phi$

$$B_x = -\frac{\mu_0}{2\pi}\frac{\delta M_y y}{x^2+y^2}, \quad B_y = \frac{\mu_0}{2\pi}\frac{\delta M_y x}{x^2+y^2}, \quad B_z = 0. \tag{2.6}$$

The total magnetic field strength B_{film}, and the field gradient B'_{film}, are more conveniently expressed using radial co-ordinates

$$B_{film}(r) = \frac{\mu_0}{2\pi}\frac{\delta M}{r}, \qquad B'_{film}(r) = \frac{\mu_0}{2\pi}\frac{\delta M}{r^2} \tag{2.7}$$

where $B_{film} = \sqrt{B_x^2 + B_y^2}$ and $r = \sqrt{x^2+y^2}$ with the film edge located at $r = 0$.

We note here that the magnetic field produced by the perpendicularly magnetised

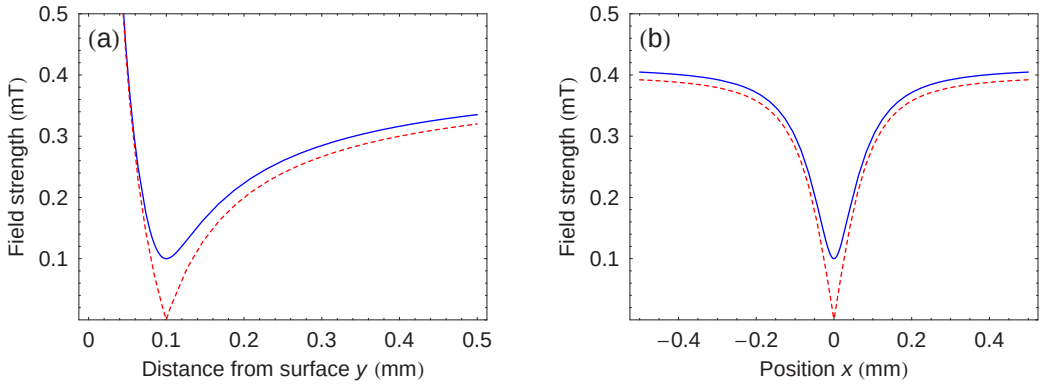

Fig. 2.3: (Colour) Magnetic field cross-sections along $y-$ (a) and $x-$coordinates (b) for the magnetic film microtrap. The bias magnetic field $B_{bias} = 0.4$ mT is oriented along x to produce a magnetic quadrupole potential $y = 0.1$ mm from the surface (dotted lines). An additional offset field $B_z(0) = 0.1$ mT is applied along the z axis to lift the field minimum and create an Ioffe-Pritchard trap which is approximately harmonic at the centre (solid lines).

film given by Equation (2.6) and Equation (2.7) is equivalent to that produced by a thin current carrying wire aligned perpendicular to the magnetisation direction (along z) at $r = 0$. This equivalence can be understood by considering the magnetic film as comprised of many small magnetic domains. The magnetic field produced by each domain is equivalent to the one produced by an imaginary surface current flowing along the domain borders, perpendicular to the magnetisation vector [54]. For a uniformly magnetised film the effective currents of neighbouring domains cancel within the body of the film. At the edge of the film however a net effective current exists with magnitude given by the product of the magnetisation and the film thickness ($I_{eff} = \delta M$). In our experiments the effective current of the magnetic film is approximately 0.2 A.

The field from the magnetic film alone cannot be used to produce a magnetic trap as it does not possess a magnetic minimum. We therefore add a uniform bias magnetic field B_{bias} oriented along x. The two fields cancel to produce a magnetic field zero at the position r_0

$$r_0 = \frac{\mu_0}{2\pi}\frac{\delta M}{B_{bias}}. \tag{2.8}$$

Near the minimum the field strength increases linearly in a two-dimensional quadrupole geometry $|B(r)| \approx |B'_{film}(r_0)(r - r_0)|$. Away from the minimum, $r \gg r_0$ the field strength is given by the amplitude of B_{bias}. Cross sections of the magnetic field at the trap position are shown in Figure 2.3.

To avoid spin-flip loss at the field zero it is then necessary to apply a second magnetic field $B_z(z)$ aligned along the z axis. The magnetic field near the trap minimum $r \to r_0$ is then given by

$$\begin{aligned} B(r,z) &\simeq \sqrt{B'_{film}(r_0)^2(r-r_0)^2 + B_z(z)^2} \\ &\simeq B_z(z) + B'_{film}(r_0)^2(r-r_0)^2/2B_z(z) \\ U(r,z) &\simeq U_z(z) + \frac{1}{2}m\omega_r^2(r-r_0)^2 \end{aligned} \tag{2.9}$$

where $U_z(z) = m_F g_F \mu_B |B_z(z)|$, m is the atomic mass and the radial harmonic trap frequency is

$$\omega_r = B'_{film}(r_0)\sqrt{\frac{m_F g_F \mu_B}{m B_z(z)}} \tag{2.10}$$

In practice the field $B_z(z)$ is applied through two current-carrying 'end wires' positioned beneath and aligned perpendicular to the film edge which act as the pinch coils of an Ioffe-Pritchard trap. Modest currents (< 10 A) can be applied through the end wires which add a small offset field to the trap bottom as well as providing weak axial confinement of the atoms to form a three dimensional trap. The trap position r_0 and the radial trap frequency ω_r are both controlled with B_{bias} by varying the current through external magnetic field coils.

2.3 Properties of thermal atom clouds

Throughout this thesis the Boltzmann distribution function is used to describe the properties of cold atom clouds above the BEC transition temperature. The Boltzmann distribution function, $f(\boldsymbol{p}, r, z, t)$, represents the position and momentum distribution

of atoms within the cloud. From this it is straightforward to calculate many properties of the cloud such as the the average energy of atoms in the cloud, the phase space density and the atomic density distribution, both in the magnetic trap and during ballistic expansion. The Boltzmann distribution function is written as

$$f(\boldsymbol{p}, r, z) = \frac{N}{Z} \exp\left(-\left[\frac{\boldsymbol{p}^2}{2m} + U(r,z)\right]/k_B T\right), \tag{2.11}$$

where N is the total number of atoms in the cloud, the momentum $\boldsymbol{p} = \{p_x, p_y, p_z\}$ and Z is the partition function given by

$$Z = \iiint \exp\left(-\left[\frac{\boldsymbol{p}^2}{2m} + U(r,z)\right]/k_B T\right) d\boldsymbol{p}\; dr\; dz. \tag{2.12}$$

For a harmonic potential, the partition function is easily evaluated and the Boltzmann distribution function is

$$f(\boldsymbol{p}, r, z) = \frac{N\omega_r^2\omega_z m^3}{(2\pi k_B T)^3} \exp\left(-\left[\frac{\boldsymbol{p}^2}{2m} + \frac{1}{2}m\omega_r^2 r^2 + \frac{1}{2}m\omega_z^2 z^2\right]/k_B T\right), \tag{2.13}$$

where as previously $r = \sqrt{x^2 + y^2}$. The in-trap density distribution $n(r, z)$ is then found by integrating $f(\boldsymbol{p}, r, z)$ over $\boldsymbol{p}$ to give

$$n(r,z) = n_0 \exp\left(-\frac{r^2}{2\sigma_r^2} - \frac{z^2}{2\sigma_z^2}\right) \tag{2.14}$$

where n_0 is the peak atomic density, and we have defined the cloud widths $\sigma_{r,z}$

$$n_0 = \frac{N}{(2\pi)^{3/2}\sigma_r^2\sigma_z}, \qquad \sigma_{r,z}^2 = \frac{1}{\omega_{r,z}^2}\frac{k_B T}{m}. \tag{2.15}$$

The thermal expansion rate of atom clouds after sudden release from the microtrap is commonly used to measure the cloud temperature and is also used to calibrate the optical imaging system by monitoring the acceleration of the cloud under gravity. At time $t = 0$ the confining potential is completely switched off so the cloud expands ballistically and begins to fall under gravity. Using the simple evolution law for

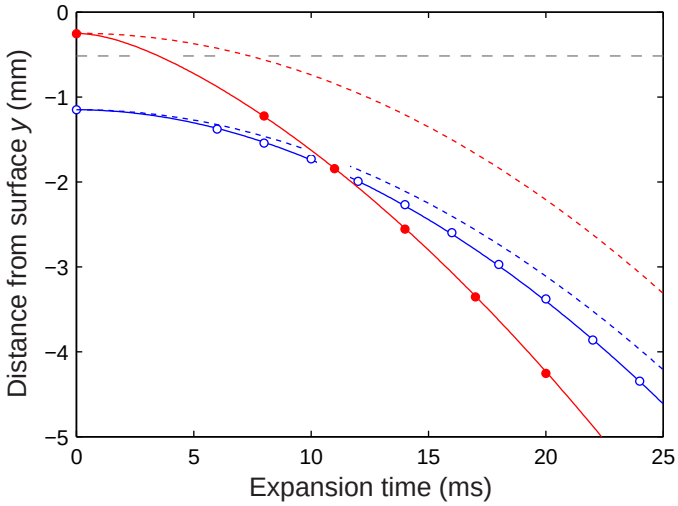

Fig. 2.4: (Colour) Time evolution of the cloud position after switching off B_{bias}. Experimental data (circles), the gravitational acceleration (dotted lines) and the results of numeric Monte-Carlo calculations which include the effect of the magnetic film (solid lines) are shown. Data is for a cloud initially positioned ∼0.24 mm (solid circles) and ∼1.2 mm (open circles) from the film surface. The dashed horizontal line corresponds to $m_F g_F \mu_B B'(r) = mg$.

a particle accelerated under gravity, we substitute $y(t) = y(0) - p_y t/m + \frac{1}{2}gt^2$ into Equation (2.13). Integrating the Boltzmann distribution function over $\boldsymbol{p}$ and calculating the first and second moments of the density distribution gives the time evolution of the cloud position and width respectively

$$y(t) = y(0) + \frac{1}{2}gt^2 \tag{2.16}$$

$$\begin{aligned}\sigma(t)^2_{r,z} =& \sigma(0)^2_{r,z}(1 + \omega^2_{r,z}t^2) \\ =& \sigma(0)^2_{r,z} + \frac{k_B T}{m}t^2.\end{aligned} \tag{2.17}$$

where $g = 9.8$ m/s^2. We note here that for short times ($\omega^2 t^2 \ll 1$) the distribution of atoms in expansion strongly reflects the in-trap density distribution $\sigma(0)$, while for longer expansion times the atomic distribution is closely related to the in-trap momentum distribution.

For expansion of clouds near the permanent magnetic film the situation can be slightly more complex. When the bias magnetic field (B_{bias}) is removed to release the atoms, the remaining permanent magnetic field gradient contributes an additional force during expansion. For atom clouds released at a position where the field gradient is comparable or larger than the gravitational force ($m_F g_F \mu_B B'(r_0) \geq mg$) the additional acceleration and the modification to the expansion rate needs to be considered. For ^{87}Rb in the $|F = 2, m_F = +2\rangle$ state the critical value of the field gradient is 0.15 T/m which is found approximately 0.5 mm from the film surface. Atoms released further from the surface feel only a small additional force and the effect of the film can usually be neglected. A quantitative description of the cloud expansion in the presence of the $1/r$ potential produced by the film can be obtained using numeric Monte-Carlo calculations, as an analytic solution to this problem is difficult. In Figure 2.4 experimental data and Monte-Carlo calculations of the centre-of-mass position of two atom clouds are shown after release from magnetic traps located at two distances from the film surface. A cloud released far from the film surface, $r_0 > 1$ mm falls at a rate expected for gravitational acceleration with only a small modification (less than 10%) due to the permanent magnetic field gradient. A cloud released from the permanent magnetic film microtrap located ~ 0.2 mm from the film experiences a dramatic acceleration generated by the relatively high field gradient.

In Figure 2.5 similar data and calculations are shown for the evolution of the cloud width during expansion. Far from the film surface the expansion rate is simply related to the cloud temperature by Equation (2.17). Closer to the film surface however the expansion is strongly affected by the permanent magnetic field gradient. This can be understood as atoms with a velocity component toward the surface experience a larger magnetic field gradient than atoms travelling away from the surface which causes a focusing effect in one dimension. The actual cloud temperature is inferred from the axial expansion rate which is unaffected by the field from the film.

There are several ways to minimise the effect of the magnetic film on the cloud expansion. A simple method used throughout this thesis is to reposition the cloud far

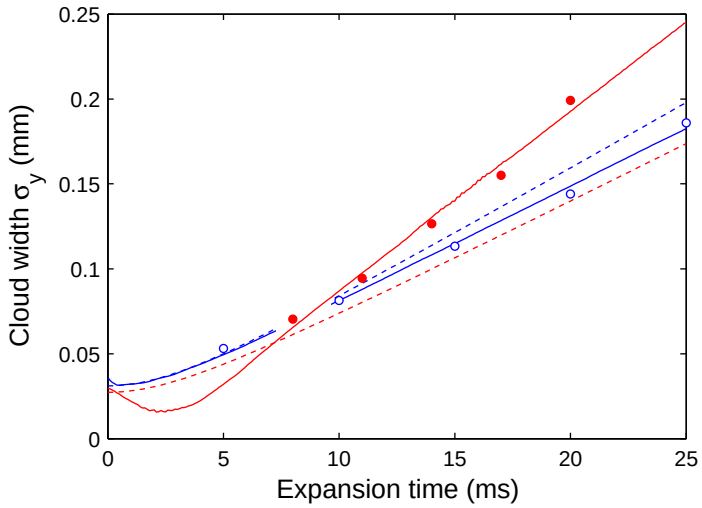

Fig. 2.5: (Colour) Time evolution of the vertical cloud width after switching off B_{bias}. Experimental data (circles), free ballistic expansion (dotted lines) and the results of Monte-Carlo calculations (solid lines) are shown for the expansion of atoms away from the film surface. Results are shown for a cloud initially positioned ∼0.24 mm (solid circles) and ∼1.2 mm (open circles) from the magnetic film surface.

from the surface ($\sim$ 1 mm) where the permanent magnetic field gradient is significantly reduced. In cases where this is not possible it is also sufficient to analyse the axial expansion rate which is unaffected by the radial field gradient. Other possibilities that haven't been explored in this work but may be the topic of future studies are to transfer the atoms to a magnetic field insensitive state or to apply a large additional field during expansion. Atoms can be outcoupled from the trap using a rf sweep to transfer the atoms to $m_F = 0$ after which they can expand freely. Alternatively, a large offset magnetic field along z during expansion acts to reduce the absolute field gradient by a factor of $(1 + B_z^2/B_{film}^2)^{\frac{1}{2}}$. A field strength $B_z \sim 5$ mT would suppress the effect of the film on expansion by a factor of 10 for even the closest approaches.

2.4 Bose-Einstein condensates

According to the Bose-Einstein statistics of an ideal quantum gas of bosonic atoms, a phase transition occurs when the atomic de Broglie wavelength becomes comparable to the mean interatomic separation. Under these conditions, the quantum ground state of the system becomes macroscopically populated, corresponding to the onset of Bose-Einstein condensation. At finite temperature, only a fraction of the atoms (N_c/N) occupies the ground state, with the rest distributed over the excited states. A standard approach involves assuming $k_B T \gg \hbar\omega$, and describing the system in two components [55–57], one the macroscopically populated ground state and a thermal component given by the classical Boltzmann distribution.

Using a semiclassical description of the excited states (the thermodynamic or large-N limit) for a system of non-interacting atoms in a harmonic oscillator potential, one finds for the number of condensate atoms N_c [55]

$$N - N_c = \zeta(3)\left(\frac{k_B T}{\hbar\omega}\right)^3 \tag{2.18}$$

where $\zeta(x)$ is the Riemann Zeta function and $\zeta(3) = 1.202$. From this result it is possible to write the critical temperature for the Bose-Einstein condensation transition,

$$T_c = \left(\frac{N}{\zeta(3)}\right)^{\frac{1}{3}} \frac{\hbar\bar{\omega}}{k_B}, \tag{2.19}$$

which can be inserted into Equation (2.18) to obtain the condensate fraction for $T < T_c$

$$\frac{N_c}{N} = 1 - \left(\frac{T}{T_c}\right)^3 \tag{2.20}$$

Finite size effects have been neglected in this treatment as they are insignificant for the size of typical systems, $N > 1 \times 10^4$ [58].

At zero temperature, a condensate is a system of particles all occupying the same single-particle state. The many-body wavefunction can then be written as a product of the single-particle condensate wavefunction Ψ. In the absence of interactions Ψ

satisfies the time-dependent Schrödinger equation. In a sufficiently dilute and cold gas, the interactions can be dealt with by considering only low energy binary collisions characterised by the s-wave scattering length a_0. In this case, each atom experiences an additional potential due to the mean field effect of the other atoms which is proportional to the local atomic density. With this included, the result is the Gross-Pitaevskii (GP) equation [56, 57]

$$i\hbar\frac{\partial}{\partial t}\Psi(r,z,t) = \left(-\frac{\hbar^2\nabla^2}{2m} + U(r,z,t) + gN|\Psi(r,z,t)|^2\right)\Psi(r,z,t), \tag{2.21}$$

which has the form of a nonlinear Schrödinger equation, with the coefficient of the nonlinear term $g = 4\pi\hbar^2 a_0/m$. The interaction term can be positive or negative depending on the sign of a_0. When a_0 is positive the condensate atoms repel each other and when a_0 is negative they attract. The GP equation is valid assuming the mean separation between the atoms is smaller than the s-wave scattering length $n|a_0|^3 < 1$.

The ground state properties of the system for $U(r,z,t) = U(r,z)$ are of particular interest. In the stationary state, $\Psi(r,z,t) = \psi(r,z)\mathrm{e}^{i\mu t}$, and the GP equation can be written in time independent form

$$\mu\psi(r,z) = \left(-\frac{\hbar^2\nabla^2}{2m} + U(r,z) + gN|\psi(r,z)|^2\right)\psi(r,z) \tag{2.22}$$

where μ is the chemical potential of the condensate.

For repulsive interactions and large N, the kinetic energy term in the GP equation ($\frac{\hbar^2\nabla^2}{2m}$) can often be neglected. In this, the Thomas-Fermi limit ($Na_0/a_{ho} \gg 1$, with $a_{ho} = \sqrt{\hbar/m\bar{\omega}}$), the ground state density distribution $n(r,z) = N|\psi(r,z)|^2$ is simply

$$n(r,z) = \frac{1}{g}\big(\mu - U(r,z)\big) = \frac{1}{g}\big(\mu - \frac{m}{2}(\omega_r^2 r^2 + \omega_z^2 z^2)\big), \tag{2.23}$$

for $\mu > U(r,z)$ and zero elsewhere. The density profile for a condensate in a harmonic

potential is therefore an inverted parabola with radii given by

$$R_{r,z} = \sqrt{\frac{2\mu}{m\omega_{r,z}^2}}. \tag{2.24}$$

The normalisation condition on $n(r)$ then gives the relationship between the chemical potential and the number of particles in the trap. For a harmonic potential

$$\mu = \frac{\hbar\bar{\omega}}{2}\left(\frac{15Na_0}{a_{ho}}\right)^{\frac{2}{5}}, \tag{2.25}$$

with the atomic density at the centre of the trap given by $n(0,0) = \mu/g$.

Chapter 3

A magnetic film atom chip

This chapter describes the development, construction and characterisation of a hybrid atom chip that combines a perpendicularly magnetised GdTbFeCo film with a current-carrying wire structure. This device constitutes the first permanent magnetic film atom chip based on the novel magnetic materials originally developed for high density magnetic storage media [59]. The current-carrying wire structure was fabricated using a machined silver foil technique [60] which has proven to be a very simple, effective and convenient method to rapidly develop atom chips at low cost. These two technologies provide new opportunities for the study of ultracold atoms and Bose-Einstein condensates.

Modern magnetic materials and thin-film deposition systems allow high quality films to be produced with excellent magnetic properties by simply varying the atomic composition and the deposition parameters. We have chosen the rare earth-transition metal alloy $Gd_{10}Tb_6Fe_{80}Co_4$ and carefully studied different deposition conditions to tailor the magnetic properties for the atom chip. Analysis of the films is performed using a variety of techniques including the magneto-optical Kerr effect, Superconducting Quantum Interference Device (SQUID) and magnetic force microscopy. The analysis indicates the films can be prepared with large perpendicular anisotropy, high remanent magnetisation, large coercivity and excellent magnetic homogeneity. A multilayered film is deposited on a glass substrate with a polished edge and is then uniformly magnetised to form the permanent magnet layer of the

atom chip. This is fixed to a machined silver foil current-carrying wire structure and mounted in an ultra-high vacuum chamber. The results of this chapter have also appeared in the Journal of Physics D [30] and in the Journal of Physics B [29].

3.1 Properties of permanent magnetic films

Magnetic materials are routinely classified according to their behaviour as diamagnetic, paramagnetic, ferromagnetic, antiferromagnetic or ferrimagnetic. In the absence of an external magnetic field, diamagnets, paramagnets and antiferromagnets have no net magnetisation, while ferromagnets and ferrimagnets can maintain a permanent magnetisation. Ferromagnetic materials exhibit a long-range order which causes individual electron spins (or atomic magnetic moments) to align in parallel within a region called a domain. When a magnetic field is applied, the domains aligned with the field direction grow at the expense of the others to produce a large net magnetic field. Ferrimagnets, unlike ferromagnets, typically consist of two (or more) subnetworks of different elements (or ions) with an anti-parallel spin alignment such that the difference in magnetic moment of the two subnetworks produces a large net magnetic field. A significant advantage of ferrimagnetic materials is the control available over the magnetic properties through changes to material composition or through the differing response of the subnetworks to external conditions such as temperature. The characteristic properties of a permanent magnetic material are described with a hysteresis loop (Figure 3.1) which provides the relation between the magnetisation of the material and an applied magnetic field. Important properties include:

- the saturation magnetisation M_s: the maximum magnetisation of the material when exposed to a large saturating magnetising field,
- the remanent magnetisation M_r: the magnetisation of the material after the magnetising field is removed,

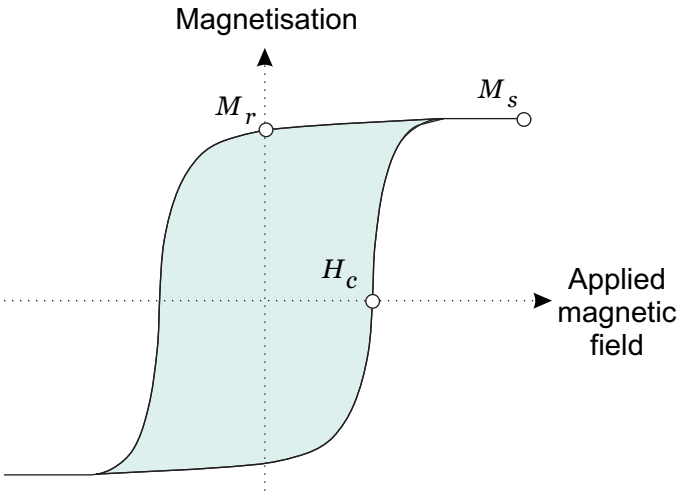

Fig. 3.1: A typical hysteresis loop of a permanent magnetic material. Characteristic properties such as the saturation magnetisation M_s, the remanent magnetisation M_r and the intrinsic coercivity H_c are indicated.

- the intrinsic coercivity H_c: the field strength required to bring the magnetisation back to zero, and
- the uniaxial anisotropy constant K_u, which characterises the dependence of the above magnetic properties on the magnetisation angle.

3.1.1 Requirements for atom chips

Thin magnetic films are appealing because of the various means of deposition and accurate control over composition which allows high uniformity and optimisation of important characteristic properties such as the uniaxial anisotropy, remanent magnetisation and coercivity. The recent development of novel magnetic materials has been primarily targeted at recordable media for use in large capacity information storage devices [59]. In particular, magneto-optical materials for data storage were developed to allow very small magnetic features, minimise the magnetisation reversal time and provide good signal readout. These materials typically exhibit a large magneto-optical Kerr effect, and have a high value of H_c but do not require a large

value of M_s or large film thickness δ. Permanent magnetic materials intended for use in atom optics also have certain requirements due to the unique operating environment and because the magnetic field strength above the surface is an important physical parameter. The magnetic film developed for our atom chip is an amorphous rare earth-transition metal alloy consisting of Gd, Tb, Fe and Co which can have:

- large magnetisation and film thickness (high effective current, $\delta \times M$) to produce large field gradients and tight trapping potentials,
- high remanence ratio ($M_r/M_s \approx 1$) and a smooth surface to allow good magnetic field uniformity,
- large coercivity to preserve the integrity of recorded magnetic patterns and to withstand the external magnetic fields used in an experiment ($\mu_0 H_c > 0.1$ T),
- excellent thermal stability and a high Curie temperature to maintain the magnetisation at elevated temperatures and over long periods of time, and
- large perpendicular magnetic anisotropy to allow small scale magnetisation patterns and complex magnetic field configurations.

3.1.2 Rare earth-transition metal GdTbFeCo films

In the early 1970s, the amorphous rare earth-transition metals (RE-TM) were discovered as a potential way to avoid grain noise caused by defects in crystalline materials [61, 62]. These films can have a large magnetic anisotropy allowing the magnetisation to be oriented perpendicular to the film plane despite their amorphous structure. Amorphous RE-TM films are used today as magnetic recording media for magneto-optical disks and modern high density hard disk drives and are ideal for atom chips because they are homogeneous, can be patterned with small magnetic features and their properties can be varied considerably by tuning composition and deposition parameters.

A RE-TM film [59, 63, 64] consists of a RE spin subnetwork coupled antiferromagnetically to a TM spin subnetwork. Alloys consisting of heavy rare-earth elements such as Gd and Tb exhibit ferrimagnetic order and align antiparallel to transition metals such as Fe or Co. This reduces the saturation magnetisation of the film but helps increase the coercivity, resulting in a square hysteresis loop.

The effect of temperature on the magnetic properties of a RE-TM film can be categorised in terms of reversible, irreversible, or structural changes. Reversible changes are simply due to different temperature dependencies of the RE and TM magnetic moments: at low temperature the RE moment dominates over the TM moment, at higher temperatures the net magnetisation reverses, and at the compensation temperature (T_{comp}) the net magnetisation reduces to zero and subsequently the coercivity increases. Irreversible changes occur beyond the Curie temperature (T_{Curie}) where the thermal energy acts to destabilise and break up the magnetisation into randomly oriented magnetic domains. After returning to low temperatures, the original magnetisation can be restored by re-applying the magnetising field. Structural changes are usually associated with the onset of crystallisation which can permanently modify the bulk magnetic properties. Oxidisation and diffusion of various elements are also significant forms of structural change.

A RE-TM film can be tailored for a particular application by choosing a suitable composition [65]. Listed in Table 3.1 are key properties of several compositions which exhibit large perpendicular anisotropy and a high remanence ratio at room temperature. We summarise some general trends. T_{comp} decreases rapidly as the transition metal content is increased and at the compensation composition (RE/TM$\sim$ 0.78) T_{comp} is close to room temperature resulting in small saturation magnetisation but large intrinsic coercivity. The Curie temperature T_{Curie} can be tuned independently of T_{comp} by selecting the Co/Fe ratio. For example T_{Curie} is about 150 °C for an Fe rich film but can increase up to 500 °C with increasing Co content. For a constant RE/TM ratio, the intrinsic coercivity is expected to increase with the ratio of Tb/Gd. The perpendicular anisotropy of RE-TM films also depends on composition

Table 3.1: Properties of GdTbFeCo films of variable composition.

Sample ID	Composition (% at.)	$\mu_0 H_c$	$\mu_0 M_s$	T_{Curie}
M531	$Tb_{24}Fe_{76}$	1.60 T	0.038 T	150°C
M532	$Tb_{11}Gd_8Fe_{81}$	0.49 T	0.126 T	190°C
M712	$Gd_{12}Tb_3Fe_{85}$	0.05 T	0.157 T	190°C
M721	$Tb_{15}Fe_{79}Co_6$	0.11 T	0.239 T	220°C
M529	$Tb_{14}Gd_5Fe_{73}Co_8$	0.34 T	0.251 T	300°C
M530	$Gd_{10}Tb_6Fe_{80}Co_4$	0.12 T	0.377 T	300°C

Magnetic film properties courtesy of W. Challener, Imation Corp.

but has a strong dependence on sputtering conditions such as the buffer gas pressure and the target voltage. The composition $Gd_{10}Tb_6Fe_{80}Co_4$ (sample M530) was chosen for a combination of large magnetisation, high coercivity and high Curie temperature.

3.2 Deposition procedure

This section details the procedure used to deposit the GdTbFeCo film on a polished glass substrate. A systematic study of the deposition parameters was performed in order to optimise the shape of the hysteresis loop, to maximise the total film thickness and increase the coercivity.

3.2.1 Substrate preparation

Careful preparation of the edge and top surface of the substrate is critical to ensure the deposited film produces smooth magnetic potentials and is suitable for an atom chip. A glass coverslip with a thickness of 0.3 mm was chosen as the substrate and cut to dimensions of 40 mm by 24 mm. A stack of 30 coverslips was bonded with wax to provide rigidity while the long edges were polished to optical quality ($\sim \lambda/20$) with an aluminium oxide grit using a commercial polishing apparatus. The wax was then removed and the individual substrates were cleaned for approximately 30 minutes in an ultrasonic bath with a nitric acid solution (30% *vol.*). The acid is then replaced with

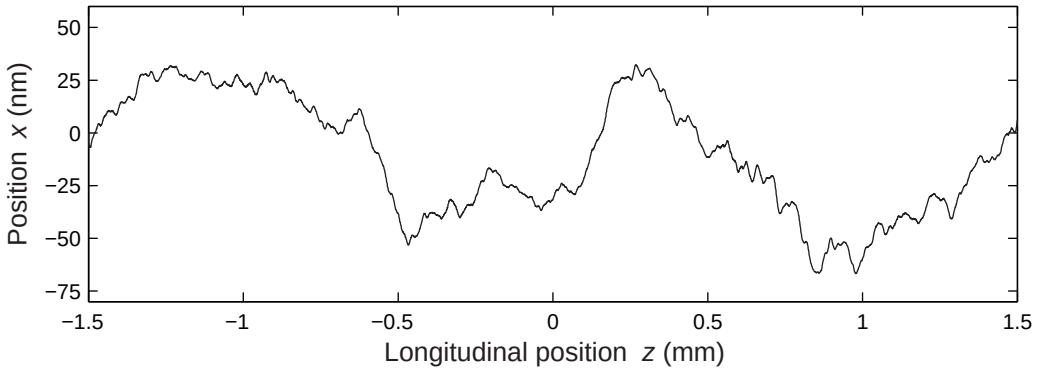

Fig. 3.2: The edge profile of a polished glass slide substrate measured using a scanning stylus profilometer. The edge is extremely smooth with an *rms* roughness of 30 nm.

a non-etch alkaline solution (2% *vol*. Extran MA03) for a further 15 minutes. Finally the substrate is thoroughly rinsed with deionised water and is ready for the deposition process. Scanning electron microscope (SEM) analysis of a substrate prepared in this way indicates very few defects and an extremely sharp and excellent quality edge. A stylus profilometer (Tencor Alphastep) scanned along the polished edge indicates the residual edge roughness is less than 10 nm *rms* over short length scales (< 400 μm) while the dominant component has a periodicity of $\sim$1400 μm and an *rms* amplitude of 30 nm (Figure 3.2).

3.2.2 Sputter deposition

The GdTbFeCo films were produced using a computer controlled cryo-pumped thin film deposition system (Kurt J. Lesker CMS-18) capable of multiple magnetron sputtering and e-beam evaporation. The base pressure of the system is 5×10^{-8} Torr, and the deposition temperature can be set between room temperature and 800 °C. Argon is used as a sputtering gas with a pressure between 2×10^{-3} Torr and 2×10^{-2} Torr. Up to 4 substrates are mounted on a 150 mm diameter stainless steel holder attached to a rotating stage. The distance between the deposition source and the sample is 0.2 m.

The CMS-18 system was operated by Dr. James Wang. After loading the substrates

the system temperature is set and the deposition chamber is evacuated overnight. Prior to deposition the sample is shielded and the targets are sputter-cleaned. The sample holder is rotated at 5 rpm to ensure the film is deposited uniformly. A high purity Cr target (as an underlayer) and a composite $Gd_{10}Tb_6Fe_{80}Co_4$ target are DC magnetron sputtered with deposition rates of 10 nm/min and 3 nm/min for Cr and GdTbFeCo respectively.

After deposition we studied the effect of the deposition parameters to obtain square hysteresis loops, large coercivity and high remanence ratio. An Ar buffer gas pressure of 4 mTorr and a DC discharge power of 150 W were found to be optimum values [30]. The magnetic properties of the films also vary considerably with the Cr underlayer thickness, deposition temperature and GdTbFeCo thickness. Magneto-optical Kerr effect (MOKE) measurements of a series of films deposited with varying Cr underlayer thickness indicate the coercivity is relatively small for films with no underlayer ($\mu_0 H_c$=0.07 T) and increases beyond 0.25 T for a Cr thickness of greater than 60 nm. We find the optimal deposition temperature is 100 °C, whereas at 200 °C the coercivity decreases by about 50%. As the thickness of GdTbFeCo is increased beyond 250 nm the magnetic properties deteriorate rapidly; characterised by a sharp decrease in coercivity and a reduction in the remanence ratio. This is most likely caused by the competition between the fixed magnetic anisotropy energy which works to maintain perpendicular alignment of magnetic domains and the demagnetisation energy which increases with the film thickness and acts to rotate the easy axis in-plane. In order to increase the thickness beyond 250 nm we have produced a multilayer film for the atom chip. The multilayer film consists of 6 alternating layers of Cr (120 nm) and GdTbFeCo (150 nm) films deposited over 6.5 hrs. After deposition, one of the four samples is removed from the system for later MOKE analysis. Finally, a thin bonding layer of Cr (10 nm) and a reflective Au overlayer (100 nm) is applied to the top surface of the film. The film has a total thickness of GdTbFeCo of 900 nm and good magnetic properties.

3.3 Film characterisation

The properties of the magnetic films have been analysed using a home-built magneto-optical Kerr effect (MOKE) magnetometer, a commercial superconducting quantum interference device (SQUID) magnetometer and an atomic and magnetic force microscope (AFM/MFM).

3.3.1 Hysteresis measurements

The magneto-optical Kerr effect manifests itself as a small polarisation rotation when linearly polarised light reflects from a magnetised surface. The degree of rotation is proportional to the magnetic moment at the film surface but is also strongly dependent on other parameters such as the magnetic composition, the angle of incidence, the probe wavelength and any material surrounding the film such as protective coatings. Because of this, MOKE is used only for qualitative analysis of films allowing measurements of the coercivity, the remanence ratio and the shape of the magnetic hysteresis.

The MOKE setup is arranged in polar configuration to measure perpendicular magnetisation hysteresis loops. It consists of two air-cooled 400 W electromagnetic coils, a diode laser source (780 nm), polarising optics and a sensitive photodiode. The sample is mounted between the coils with a plastic holder and non-magnetic BeCu fasteners. The electromagnets are manually operated with a current supply (Xantrex XFR 600-2) to provide a magnetic field perpendicular to the sample (0.82 T/A) with a maximum strength of ± 1 T. The laser is incident on the film at approximately 45° from the surface normal. The Kerr rotation ($\approx \pm 0.3$ degrees) and the subsequent change in photodiode signal is proportional to the perpendicular magnetic moment. The photodiode signal and the coil current are simultaneously recorded to a digital oscilloscope over a complete hysteresis cycle and the data is post-processed to extract the hysteresis loop. For a quantitative measure of the magnetisation we calibrate the amplitude of the MOKE signal against a measurement made using a superconducting quantum interference device (SQUID).

Quantitative information on the bulk properties of the material, the magnetisation

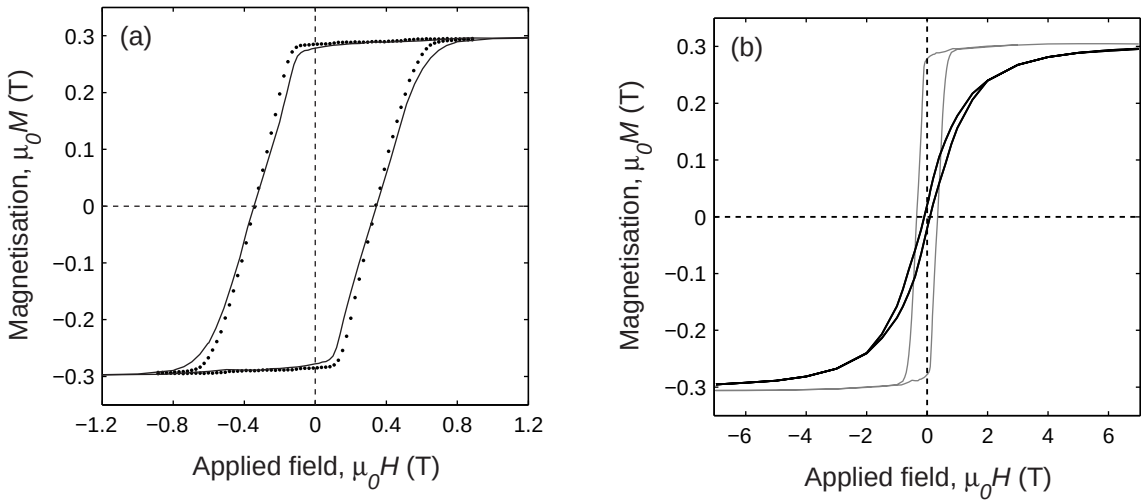

Fig. 3.3: Perpendicular (a) and in-plane (b) hysteresis loops of the multilayer GdTbFeCo magnetic film. In (a) the hysteresis loop is measured using MOKE (dots) and SQUID (solid line) magnetometry. The saturation magnetisation of the film is obtained with SQUID and is used to calibrate the amplitude of the MOKE hysteresis loop. Both loops shown in (b) are measured by SQUID as a direct comparison between the perpendicular hysteresis (solid grey line) and the in-plane hysteresis (solid line).

and the in-plane hysteresis are provided by measurements with a superconducting quantum interference device (SQUID, Quantum Design MPMS5) carried out by Dr. James Wang. SQUID magnetometry is a time consuming and expensive process, but provides an absolute measure of the bulk magnetic moment of the film. To perform a SQUID measurement the samples were coated with a photoresist for protection from cooling liquids before being diced into eleven 4 mm×4 mm pieces. The volume of magnetic material is accurately determined from the film thickness and optical microscope images of the remaining surface area. After dicing the magnetic film occupies about 80% of the full 4 mm×4 mm surface. The 11 pieces are stacked to fit into the SQUID and hysteresis measurements are made perpendicular and parallel to the film plane at room temperature (Figure 3.3). From the hysteresis loop we determine the perpendicular remanent magnetisation to be $\mu_0 M_r = 0.28$ T and the saturation magnetisation to be $\mu_0 M_s = 0.31$ T ($M_r/M_s = 0.91$). The coercivity is $\mu_0 H_c = 0.32$ T in good agreement with the MOKE result. The small discrepancy between the shape of

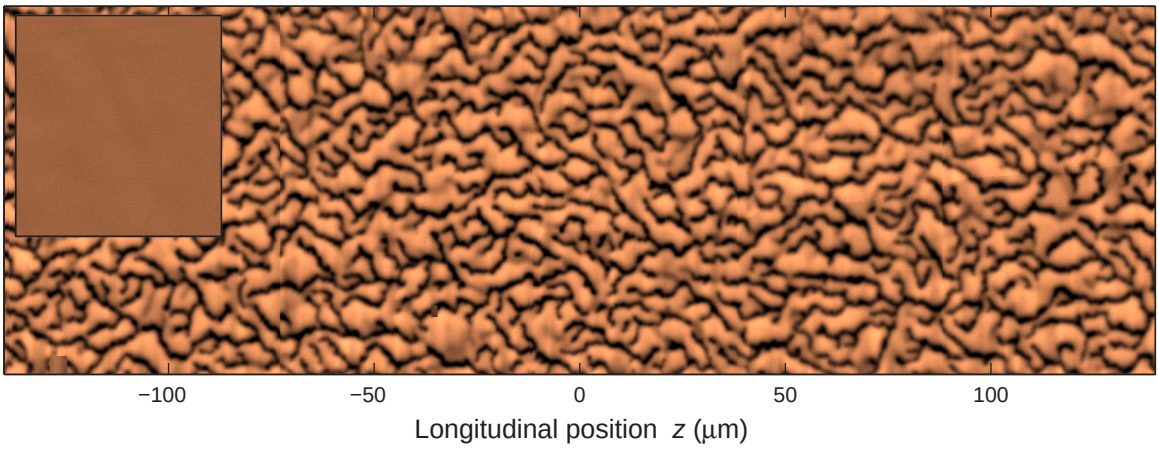

Fig. 3.4: (Colour) Magnetic force microscope (MFM) image of the multilayer GdTbFeCo magnetic film after being demagnetised at high temperature. The full image is stitched together from nine individual MFM measurements to cover a 90×550 μm^2 area of which the central 90×280 μm^2 is shown. The inset shows a 50×50 μm^2 region of the film after magnetisation.

the hysteresis loops obtained using MOKE and SQUID magnetometry are attributed to a difference in surface and bulk magnetic properties of the multilayer magnetic film.

3.3.2 Scanning probe microscopy

In addition to the hysteresis measurements, the deposited films are analysed in-house using an atomic and magnetic force microscope (AFM/MFM). The AFM (NT-MDT SPM Solver P7LS microscope) is fitted with an acoustic hood, active vibration isolation and a closed loop equivalent scanner. The longitudinal scanning range is 90 μm×90 μm and the vertical range is 5 μm. The ultimate vertical resolution is 0.1 nm. The cantilevers are high resolution silicon probes with a 40 nm CoCr magnetic coating. The AFM is operated in two passes. First the surface topology is measured in semi-contact mode. A phase sensitive second pass in non-contact mode is performed at a constant height to provide the magnetic force signal.

The surface morphology of the GdTbFeCo films is found to accurately follow that of the Cr underlayer with round grains of approximately 40 nm diameter and a *rms*

roughness of 3.2 nm. A MFM image of an unmagnetised film showing the magnetic domain structure is shown in Figure 3.4. The magnetic domains are clearly visible as stripes with a typical domain width of 1 μm. Spectral analysis of the domain structure indicates nearly white noise characteristics (uncorrelated positions) which roles off for features smaller than $d = 5$ μm. The film is then uniformly magnetised using the MOKE and re-analysed with the MFM. After magnetisation the film is extremely homogeneous with no evidence of residual magnetic domains (Figure 3.4-inset). The ratio of the magnetised to unmagnetised MFM signal amplitude is 0.07 indicating low levels of residual inhomogeneity although the measurement appears to be limited by the intrinsic noise of the MFM.

3.4 A hybrid atom chip

The magnetic field produced by the GdTbFeCo film is well suited to tight confinement of ultracold atoms close to the surface, but is too short ranged to effectively load atoms from the background atomic vapour. To support the magnetic film microtrap and facilitate good loading efficiency, a high current wire structure is incorporated. The wire structure is produced using the micromachined silver foil technique using readily available materials and machinery. This structure is used initially for a mirror magneto-optical trap (MMOT) and as a magnetic trap which can be positioned between 0.1 mm and 2 mm from the film surface. After preliminary evaporative cooling the atoms can be transferred to the magnetic film microtrap by reducing the current to zero.

3.4.1 Construction of the atom chip

A schematic diagram and photo of the complete atom chip is shown in Figure 3.5. The atom chip is made entirely of ultrahigh vacuum compatible components and was constructed in a clean room environment.

A Shapal-M machineable ceramic baseplate with dimensions 54×54×2 mm^3 is made with four 3.0 mm diameter mounting holes and eight 2.0 mm diameter holes

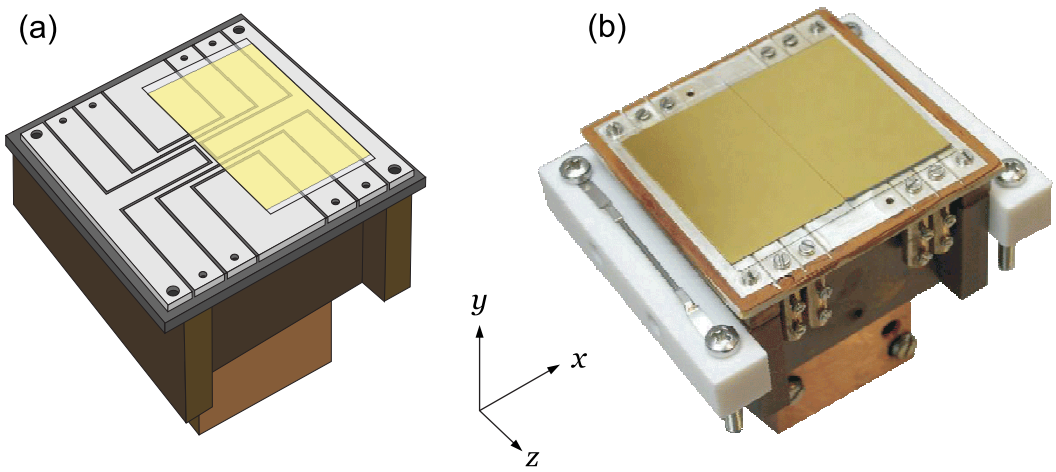

Fig. 3.5: (Colour) A schematic (a) and a photograph (b) of the constructed atom chip. From the top down: adjacent glass substrates, machined silver foil structure with end wires, Shapal-M baseplate and Cu heat sink.

for electrical connections. A 50×50×0.5 mm^3 silver foil (Goodfellow AG000465) is first sputter coated with a Cr bonding layer. Ultrahigh vacuum compatible epoxy (Epotek-H77) is then evenly applied to both the Cr surface of the silver foil and the ceramic baseplate and left to cure for 6 hrs on a hotplate at 150 °C. The wire structure was programmed using Isopro software and loaded to a computer controlled PCB mill (T-Tech Quick-Circuit 5000). The cutting speed was set to 50 mm/min and the spindle speed was 10,000 rpm. Insulating channels of 0.5 mm width were cut into the 0.5 mm thick foil in 0.1 mm steps to avoid damage to the ceramic baseplate, the mill-bit or the wire structure. Each wire has a width of 1 mm and is broadened to 6 mm at the ends to facilitate good electrical connections. The H-shaped structure allows both U-wire and Z-wire configurations by choosing the appropriate electrical connections, while two additional end-wires act as a radio-frequency antenna and provide longitudinal confinement for the magnetic film trap.

After milling, the channels are backfilled with epoxy to provide structural integrity and improve the thermal power dissipation. Through-holes are made in the machined silver foil and the surface is hand polished to support the magnetic film substrate. The

top layer of the atom chip consists of two 0.3 mm thick polished glass slide substrates that are sturdy enough to prevent warping (Section 3.2.1). One substrate is coated with a multilayer GdTbFeCo/Cr film and a Au overlayer using the procedure outlined in Section 3.2. The second substrate is coated with a Cr bonding layer and a Au overlayer. The glass surfaces are thinly coated with epoxy (< 50 μm) and are carefully positioned by hand to the centre of the H-wire. The gold top surface forms a large reflective area (40 mm $\times$ 46 mm) for use with a mirror magneto-optical trap. The threads of screws used to mount the chip are first filed along one side to allow trapped gas to escape during vacuum bake-out. The magnetic film layer, the silver foil and ceramic baseplate are then fixed to a copper block holder. The electrical connections are made using copper tabs clamped to the silver foil using 2.0 mm screws. The tabs insert into BeCu barrel connectors to join with 1.6 mm diameter bare copper wire and a 12 pin vacuum feedthrough (Ceramaseal 55 A rated). The completed atom chip was first pre-baked in an external vacuum chamber to ensure vacuum compatibility and then tested with a continuous current of 30 A. The total resistance is 4.6 mΩ and the associated temperature rise is less than 40°C. Under these conditions we observe no degradation of the ultrahigh vacuum environment.

Chapter 4

Experimental apparatus

This chapter deals with the technical aspects of the experiment such as the apparatus and techniques used daily for studying the ultracold atoms. Specifically, the ultrahigh vacuum (UHV) chamber, the lasers and optical layout, diagnostic and imaging techniques, and the computer control are described. The UHV chamber is necessary to isolate the trapped atoms from the environment and to prevent collisions with hot background gas atoms. Several frequency stabilised laser sources are required for the initial laser cooling and trapping stage and used to collect and precool a cloud of Rb atoms. We monitor fluorescence from the atoms on a photodiode during laser cooling and use resonant absorption imaging to analyse magnetically trapped atom clouds. Some aspects of the experimental setup have been described elsewhere [66] and as such this chapter serves simply to summarise the apparatus and update the reader on recent modifications.

4.1 Ultra-high vacuum setup

The vacuum system that houses the atom chip is based on a single stainless steel (304SS) chamber design which contains the chip mount, the electrical feedthroughs for the chip wires and the Rb source, viewports for optical access and additional flanges for the vacuum pumps and gauges. In the following, inches (denoted ″) are used to describe vacuum dimensions for consistency with the manufacturer's specifications. The main

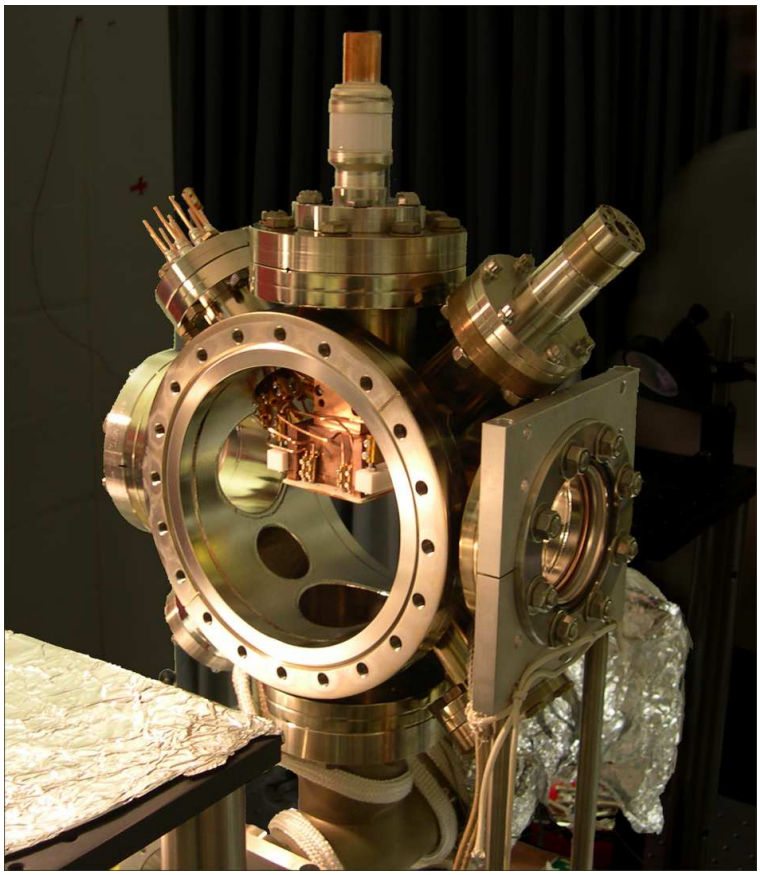

Fig. 4.1: (Colour) Photograph showing the ultra-high vacuum setup and mounted atom chip.

chamber itself has an inner diameter of 6″ and a total of 10 flanges (Figure 4.1). This includes two large 8″ diameter flanges with anti-reflection coated viewports, four 4.5″ flanges (two of which have viewports attached: one is used for mounting the atom chip, and one is attached to a 4-way cross used for vacuum pumps) and four 2.75″ flanges (two with viewports, one with the 12 pin electrical feedthrough and one with the cold cathode vacuum gauge). Two 4.5″ 3-way crosses attached below the main chamber are used to connect the three main vacuum pumps. A turbo-molecular pump (Pfeiffer TMU065) backed by a two stage diaphragm pump (Pfeiffer MD4T) is used for the bake-out and initial vacuum preparation and is connected to the rest of the vacuum system via an all-metal gate valve. Also used during the vacuum preparation is a four-filament titanium-sublimation pump (Physical Electronics TSP) positioned to deposit Ti over

a relatively large surface area below the main chamber. Although the Ti-sublimation pump is only activated during the bake-out it remains attached to the system and contributes to the overall pumping rate. After bake-out the main vacuum pump is a 75 L/s ion pump (Varian Tricell).

The main vacuum chamber houses the atom chip which is clamped upside-down to a 19 mm diameter solid copper feedthrough (Ceramaseal, 800 A rating) attached to the top-most 4.5″ flange which provides structural support as well as the capability for external cooling. The chip itself is too large to fit through the 4.5″ port with the copper post and is therefore inserted into the chamber through one 8″ port and electrical connections to the feedthrough are made *in-situ*. The rubidium source consists of two resistively heated Rb dispensers with 25 mm active length (SAES getters AMD) mounted on either side of the chip.

The base pressure before bake-out is $\sim 3 \times 10^{-7}$ Torr. Four thermocouples are clamped to the vacuum chamber at various positions to monitor the bake-out temperature and minimise any temperature gradients. Specifically, we ensure that the heating rate is relatively low (< 20 °C/Hr) to avoid damage to the glass viewports and that the temperature difference across the gate valve remains below ~ 20 °C. The chamber is heated using four 400 W flexible armoured heating tapes (Hemi Heating) roughly positioned to coincide with the locations of the thermocouples. The turbo pump and the ion pump are heated separately with their own commercial heating elements. The tapes are powered by four variable transformers to allow independent control over each part of the vacuum system. The bake-out temperature was increased steadily from room temperature to 140 °C over a period of 24 Hrs, which increases the vacuum pressure from 3×10^{-7} to 3×10^{-6} Torr. The temperature was maintained at 140 °C for 24 Hrs while the pressure decreased. We then activate the Ti-sublimation filaments and condition the Rb dispensers by running 5 A continuous current. The bake-out continues for a further 72 Hrs before we turn off the heating tapes, activate the ion pump and close the all-metal gate valve to shut off the turbo pump. We found that after bake-out each decrease in temperature of 25 °C corresponds roughly to one

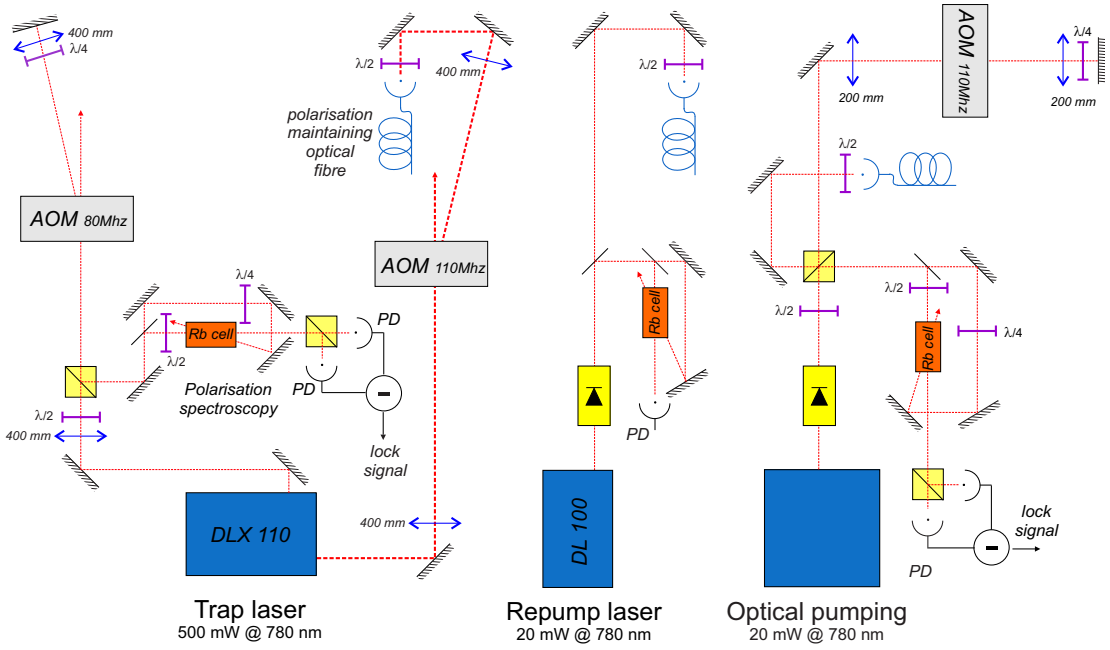

Fig. 4.2: (Colour) Schematic diagram of the optical setup showing components and simplified beam paths. The approximate position of each component reflects the actual position on the optical table.

order of magnitude decrease in vacuum pressure. The cold cathode gauge indicates $< 7.5 \times 10^{-12}$ Torr at room temperature; however the typical pressure when operating the experiment is approximately 2×10^{-11} Torr.

4.2 Lasers and optical layout

The experiment is housed on two optical tables. A simplified schematic of the optical setup on table 1 is shown in Figure 4.2. This consists of three 780 nm frequency stabilised diode laser systems which are fibre coupled and transferred to the second optical table. The laser light for the mirror magneto-optical trap is provided by a high-powered diode laser Toptica DLX110 (the so called 'trap' laser) operated at 500 mW. A low intensity locking beam provided by the DLX110 is double-passed through a frequency tuneable acousto-optical modulator (AOM) centred at +(2×)55 MHz before

entering a dither-free polarisation spectroscopy setup [67]. In this setup a Rb vapour cell is pumped using circularly polarised light and the differential refractive index (birefringence) is measured for two orthogonal polarisation components of the probe light. The locking signal is linear over approximately 10 MHz and is used as the error signal for piezo and current feedback of the laser frequency. The laser is locked to the $F = 2 \rightarrow 3$ cycling transition and the system responds to a shift of the AOM frequency within 0.5 ms. The main output of the DLX110 is passed through a second fixed frequency AOM at +110 MHz to shift the laser frequency back to resonance. The laser detuning can be adjusted via the first AOM between +15 and -60 MHz without affecting the beam alignment and the second AOM acts as a fast shutter for extinguishing the laser light. At the end of the fibre the beam has a power of approximately 100 mW, where 2 mW is taken for the optical absorption beam and the rest split evenly over four beams for the magneto-optical trap.

A second laser (Toptica DL100), the 'repumper' provides $\sim$ 20 mW of frequency stabilised laser light peak-locked to the $F = 1 \rightarrow 2$ repumping transition. At the output of the fibre we have 12 mW of resonant light of which 5 mW is taken and mixed with the optical pumping beam while the rest is mixed with the four trap beams. A third laser (home built) is frequency stabilised to the $F = 2 \rightarrow 3$ transition using current feedback derived from a polarisation spectroscopy signal. This laser is double-passed through an AOM so that the laser frequency is tuned close to the $F = 2 \rightarrow 2$ transition. After fibre coupling this laser provides 3 mW of optical pumping light.

4.3 Diagnostics and imaging

Two main techniques are used in optimising each stage of the experimental sequence and diagnosing possible problems. For characterising and optimising the parameters of the mirror magneto-optical trap (MMOT) we monitor the fluorescence of the atoms as they scatter light from the trap laser on a photodiode. We also use fluorescence to characterise the initial transfer of atoms to the magnetic trap by subsequently recapturing the magnetically trapped cloud into the MMOT. For further measurements

of magnetically trapped atoms we use absorption imaging which can be accurately calibrated to provide the absolute number of trapped atoms and spatial information on the atom cloud.

4.3.1 Fluorescence

Fluorescence is a powerful technique because it provides a continuous measure of the number of atoms in the MMOT while the trap laser is on. Fluorescence is collected via a 1″ diameter lens (focal length 100 mm) placed 140 mm from the MMOT which is as close as possible given the dimensions of the vacuum system. Directly after the lens a mirror is used to align the collected fluorescence to a large area photodiode positioned roughly where the collected fluorescence is focused. The photodiode circuit is a home-built low noise design specifically suited for high gain applications, the output of which is monitored on a digital oscilloscope. Because of the large area of the photodiode, the signal is mostly insensitive to small shifts of the cloud position and provides accurate feedback for optimising the parameters of the MMOT. In addition, fluorescence is used to optimise the efficiency of the transfer from the MMOT to the the U-wire MMOT, the polarisation gradient cooling stage and the transfer to the initial magnetic trap. The absolute number of atoms can be inferred from the fluorescence signal by [68]

$$N = \left[\frac{\Gamma/2 \; I/I_s}{1 + I/I_s + 4(\Delta/\Gamma)^2} \; \frac{hc}{\lambda} \; \frac{r^2}{4d^2} \; \eta R \right]^{-1}. \tag{4.1}$$

The first term inside the brackets is the photon scattering rate in photons per second per atom, where I is the total laser intensity at the MMOT, $I_s = 1.67$ mW/cm^2 is the saturation intensity (the stretched transition is usually taken as a representative value), $\Gamma = 2\pi \times 6.07$ MHz is the natural linewidth and $\Delta \sim 2\pi \times 18$ MHz is the laser detuning from resonance. The second term is the energy per photon, 2.55×10^{-19} J for λ =780 nm, which when combined with the first term gives the total fluorescence power in Watts. The third term is the fraction of light collected by the lens, approximated for $r \ll d$, where $r = 12.7$ mm is the radius of the collection lens and $d = 140$ mm is the

distance of the lens from the MMOT. The fourth term is the detection efficiency of the photodiode ($\eta \approx 0.47$ A/W for silicon) and the photodiode gain R, in Volts/Ampere. Although the calculation is straight-forward, accurately determining the total number of atoms using fluorescence is complicated by possible uncertainties in the intensity at the MMOT, the exact distance of the collection lens from the MMOT and the appropriate value of the saturation intensity which depends on the light polarisation and the atomic alignment which is not well defined in a magneto-optical trap [69]. Ultimately we overcome problems with calibrating the fluorescence signal by comparing the signal to an integrated absorption image which provides more reliable results for the total number of atoms with an estimated accuracy of about 10%.

4.3.2 Absorption imaging

Once atoms are magnetically trapped we use resonant absorption imaging for analysis. A single lens imaging system was used for most experiments described in this thesis; however in the past we have also implemented a two lens system to adjust the magnification and in one experiment we made use of two probe beams and two CCD cameras to simultaneously measure the longitudinal and transverse atomic cloud distributions (Chapter 6). The probe laser beam is split with approximately 2 mW from the main trap laser directly after the optical fibre and is then passed through a mechanical shutter to allow independent control from the trap laser. The beam is then expanded using a telescope arrangement to a diameter of approximately 50 mm. The intensity at the centre of the beam is approximately 80 μW/cm^2. The probe beam is aligned parallel to and centred with the chip surface, perpendicular to the trap axis (along x) using 50 mm diameter optical components. Before entering the vacuum chamber the beam is circularly polarised, σ^+ with respect to a small quantisation field applied along x during imaging. The beam passes through the atomic cloud and exits the vacuum chamber where an achromatic lens (50 mm diameter, focal length 100 mm) is placed against the viewport (approximately 140 mm from the centre of the vacuum chamber). The shadow image is recorded by a Peltier cooled CCD camera (Princeton

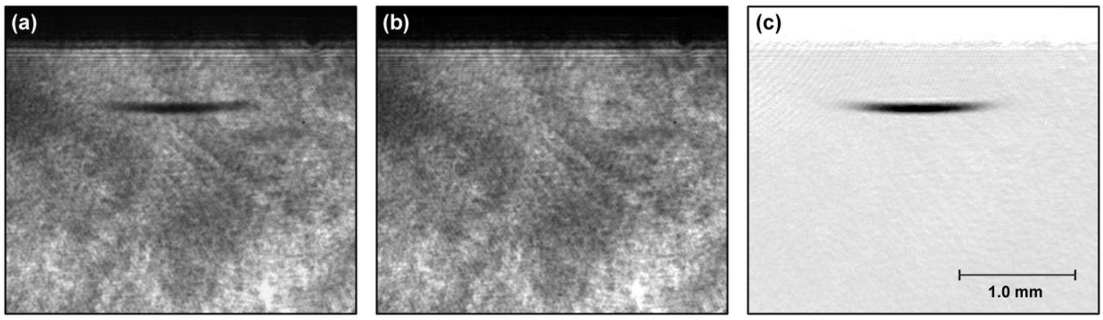

Fig. 4.3: A typical absorption image of a magnetically trapped cloud of ultracold atoms showing (a) the image frame, (b) the background frame and (c) the processed image.

Instruments 1024 × 1024 with shutter and ST-138 controller) located about 350 mm from the lens. Initially the optimum focus and the magnification of the imaging system was determined by placing a small gold coated glass slide between the lens and the viewport at 45° to image a calibration rule external to the vacuum chamber. Once atoms were loaded into the magnetic trap and evaporately cooled, a precise calibration was made against the measured acceleration of the ultracold atom cloud falling freely under gravity (Section 5.4). The measured magnification is ×2.6 corresponding to an effective pixel size of $A_{px} = 5.0 \times 5.0$ μm^2/pixel.

A typical image of the cloud consists of two frames which are post-processed using LabVIEW software (Figure 4.3). First we pre-trigger the CCD buffer by taking a clear frame which is needed to eliminate the effect of charge buildup during the previous loading cycle. After 1.2 s* the clear frame is read out to the computer and an actual absorption image I_{abs} can be recorded as the first frame. This involves first opening the absorption laser shutter, tuning the trap laser AOM to resonance, triggering the CCD and pulsing the second trap AOM on for 0.2 ms. During this time the average charge on the CCD reaches roughly 50,000 counts (the well depth is 64,000 counts). A background image frame, I_{bg}, is recorded 1.2 s later after any remaining trapped atoms are deliberately removed by switching off the trapping fields. For most purposes the

*the read-out time of 1.2 s can be reduced to ∼0.4 s if only a subset of the full frame is required.

CCD charge accumulated in the absence of probe light (the so-called dark count) is small enough ($\simeq 200$, corresponding to 0.004 I_{bg}) to be neglected in the analysis. The background noise levels on a processed image are close to the Poissonian limit.

The two-dimensional atomic density distribution (integrated over x) and the total number of atoms can be calculated from the images as

$$n(y,z) = -\frac{1}{\sigma_{abs}} \ln\big(I_{abs}/I_{bg}\big) \tag{4.2}$$

$$N = -\frac{A_{px}}{\sigma_{abs}} \sum \ln\big(I_{abs}/I_{bg}\big) \tag{4.3}$$

where the atomic absorption cross section σ_{abs} is [68]

$$\sigma_{abs} = \frac{\sigma_0}{1 + I/I_s + 4(\Delta/\Gamma)^2} \tag{4.4}$$

and σ_0 is the on-resonant absorption cross section in the low intensity limit. Typically we consider on-resonant absorption with circularly polarised σ^+ light for which σ_0 is conveniently written

$$\sigma_0 = \frac{3\lambda^2}{2\pi} = 2.905 \times 10^{-13}\ \mathrm{m}^2 \tag{4.5}$$

4.4 Computer control

The basic operation of the experiment is in three main stages. First, atoms need to be collected and cooled in a magneto-optical trap. Second, the atoms are optically pumped to $|F = 2, m_F = 2\rangle$, current is applied to the atom chip and the trap light is shut off to produce a magnetic trap. At this point various external magnetic fields are used to manipulate the position and compression of the trap. Finally, radio frequency (rf) radiation is applied via the chip wires in order to perform forced evaporative cooling, thereby reducing the temperature of the cloud to the BEC transition. Computer control is required to accurately control the parameters and timing of each of these stages.

4.4.1 Hardware

A standard personal computer with a full sized motherboard (accommodating 5 PCI slots) is used for control and synchronisation of most experimental parameters. The computer uses three identical analog output boards (National Instruments PCI 6733 with 8 analog outputs) in a Master-Slave configuration to provide 24 independent analog outputs between -10 V and 10 V. These boards are buffered and allow an ultimate time resolution of 1 μs and timing error of less than 50 ns, but are typically operated with a timing resolution of 100 μs as a trade off between the size of the buffer and the timing resolution. Of the 24 analog outputs, 8 channels are used for controlling laser sources such as the mechanical shutters and the AOM voltages. Our current drivers for the magnetic field coils are not bipolar so instead 6 channels are used for producing small magnetic fields ($0 \rightarrow 1$ mT) in each direction through 6 pairs of coils positioned around the vacuum chamber. In addition, 2 channels are used to control the quadrupole coils for the MMOT and the large bias field coils for the magnetic microtrap. Another 4 channels are used to independently control the current in the U-wire, the Z-wire and the two end-wires. The remaining channels are used for triggering the CCD, the radio frequency sources and the rubidium dispensers.

To control the magnetic field sources, 12 rack-mounted home-made current controllers have been built with current capacities of 10 A, 20 A or 30 A depending on the specific application. They are based on a simple feedback circuit with a comparator plus integrator op-amps to drive air cooled MOSFET (MTW30N20E) or IGBT (IRG4PSH71K) devices in series with the load resistance. For feedback, the circuit monitors the voltage drop across several thermally stable sense resistors (wirewound Al housed resistor, 1 Ω, 75 W, HS751RJ) in series with the load. For inductive loads such as the magnetic field coils we also place a Zener diode (200 V) across the coil terminals as a voltage clamp to protect the MOSFET/IGBT and reduce the switch-off time [70]. For most coils the field switching time is < 1 ms.

Three radio frequency (rf) generators are used regularly in the experiment. First, a logarithmic frequency sweep is applied between 20 MHz and $\sim$1 MHz over 10 s for initial

evaporative cooling. A second generator sweeps between 1.5 MHz and 0.7 MHz over ∼2 s and is used for evaporative cooling once the trapped atoms are transferred to the magnetic film (Chapter 5) and for rf spectroscopy (Chapter 6). A third generator is not capable of frequency sweeping, but instead is a constant frequency source mainly used for pulsed rf outcoupling or as an rf shield to minimise in-trap heating. Each rf source is programmed manually from the front panel but triggered by the computer. The three sources are combined using simple BNC T-pieces and are then applied to the end wires on the chip very close to the trapped atoms. This arrangement is advantageous because the rf power required is relatively small, minimising interference with other equipment. Because the end-wires have dual purposes as both an rf antenna and the end-caps for the magnetic film trap we also built a simple coupling circuit to allow rf signals to be applied in an anti-parallel wire configuration simultaneously with DC currents in a parallel configuration for creating the axial potential.

4.4.2 Software

The flexible user interfaces for programming the analog output timing sequences and for performing initial data analysis on the absorption images is written in the LabVIEW programming environment (National Instruments) under Microsoft Windows and can easily be ported to other experiments. In addition to the LabVIEW programs, detailed data analysis is typically performed using additional software for specialised tasks in Microsoft Excel, Mathematica and Matlab.

As described above, the computer control hardware operates by buffering an array of voltage levels for each time interval and output channel over the experimental sequence. Therefore, to conserve memory, the control software is implemented with two main sections with independent timing resolution. The first section of the program is defined as a loading sequence with relatively low timing resolution of 100 ms and is used for the loading sequence which takes approximately 30 s. The second section is the BEC sequence which operates at higher time resolution (100 μs) and is required to control complicated tasks such as the transfer of atoms from the initial MOT to the compressed

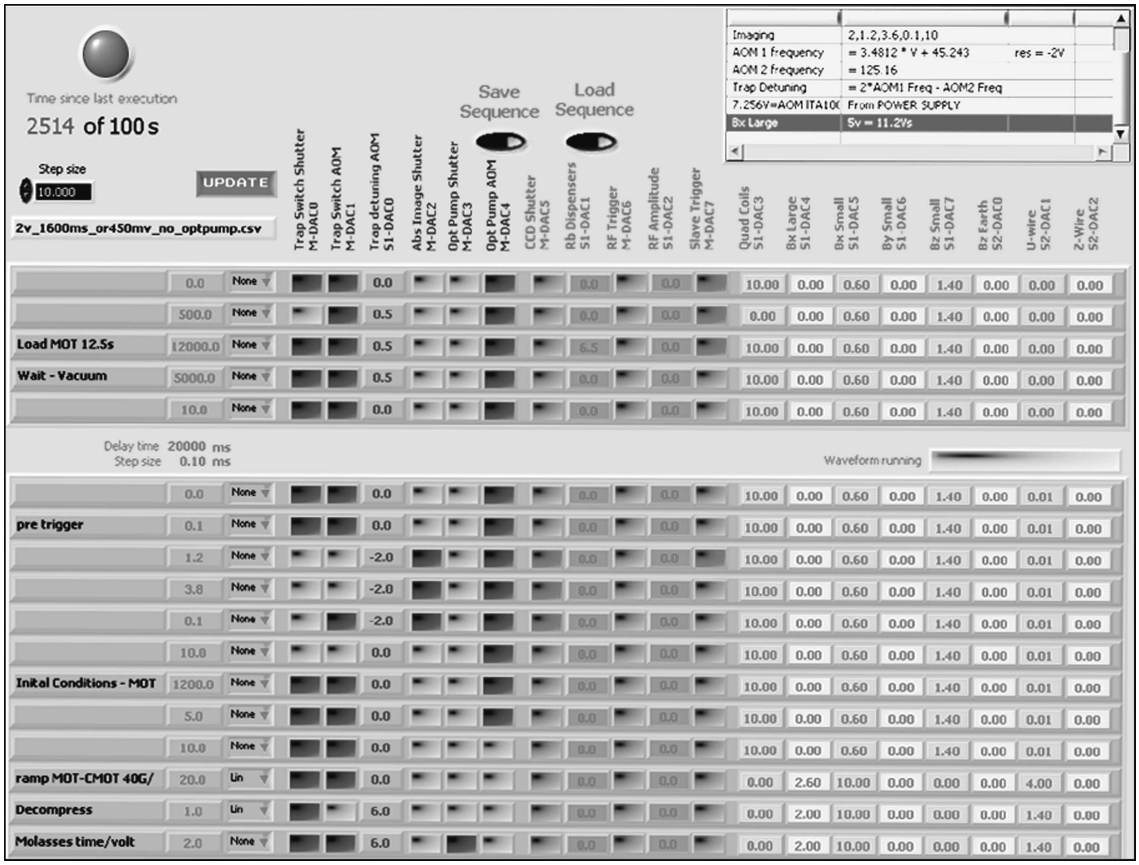

Fig. 4.4: A screenshot of the experiment control software written in LabVIEW programming environment. Columns of the interface array correspond to individual analog output channels responsible for controlling the laser shutters and AOMs as well as various magnetic field sources. Each row corresponds to a particular time interval or experimental stage in the sequence.

U-wire MOT, molasses cooling and optical pumping, magnetic trapping, evaporative cooling and absorption imaging. Also associated with each time step is a ramp option which dictates how the transition from the previous time step should be performed (options are: step, linear ramp and logarithmic ramp).

The software for analysing absorption images is also written in the LabVIEW programming environment. The software accesses the image data from the WinView image acquisition software (Princeton Instruments) via the LabVIEW WinX32 automation interface. WinView is used to acquire multiple frames in a single file which is then

read into LabVIEW and processed to give the atomic density distribution (Figure 4.3). The processed image is displayed and allows the user to zoom, alter the pseudo-colour range, integrate absorption counts to determine the total number of atoms and fit one-dimensional gaussian cross-sections. Using this software one can easily log most of the important parameters from an experiment in real time and transfer the values to common spreadsheet software to extract trends over multiple runs of the experiment.

Chapter 5

Bose-Einstein condensation on a magnetic film atom chip

This chapter deals with the production and characterisation of Bose-Einstein condensates in the Z-shaped wire magnetic trap and the magnetic film microtrap. To produce a BEC each stage of the experimental sequence is optimised. We begin by collecting ^{87}Rb atoms in a mirror magneto-optical trap. The ultracold atom cloud is brought within 1.6 mm of the chip surface by turning on a current through the U-shaped wire. After polarisation gradient cooling the U-wire is switched off so that the atoms can be optically pumped and transferred to the Z-wire magnetic trap. We adiabatically compress the magnetic trap to increase the elastic collision rate before evaporative cooling begins. Evaporative cooling consists of a 10 s rf sweep from 20 MHz to 0.78 MHz which decreases the cloud temperature by three orders of magnitude and increases the phase space density by six orders of magnitude. The BEC transition is observed by switching off the Z-wire current and recording a resonant absorption image on a CCD camera. We observe the appearance of a narrow anisotropic peak in the cloud distribution typical of the growth of a Bose-Einstein condensate. Bose-Einstein condensates have also been produced in the magnetic film microtrap. To transfer atoms to the magnetic film microtrap we truncate the rf sweep and ramp the Z-wire current to zero to move the atoms to 100 μm from the surface. A second evaporative cooling stage is accompanied by the unexpected onset of a double Bose-

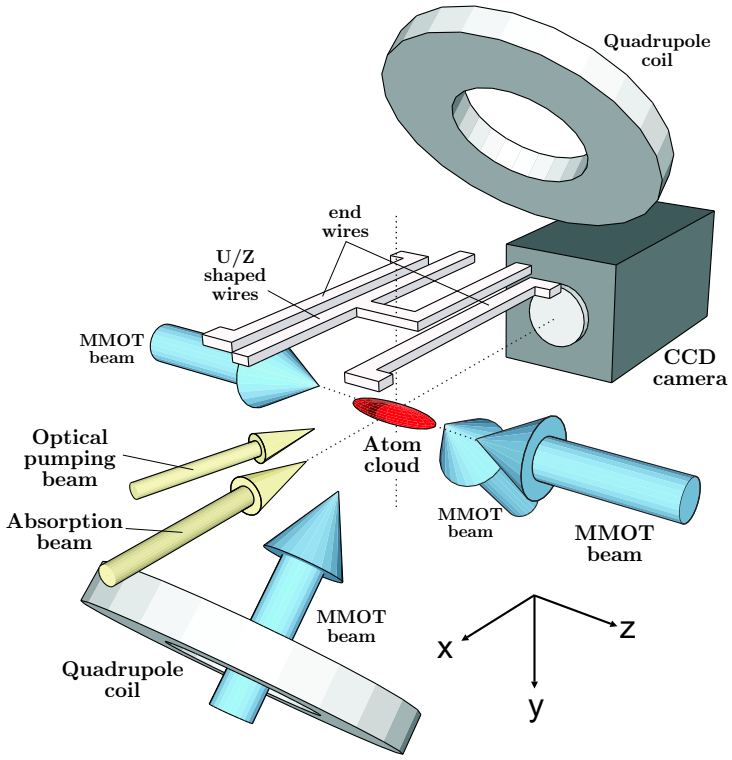

Fig. 5.1: (Colour) Schematic diagram of the setup used for collecting and laser cooling atoms in a mirror magneto-optical trap (MMOT), and for transferring atoms to the Z-wire magnetic trap ready for radio frequency evaporation.

Einstein condensate. The magnetic field produced by the film is determined from the position and oscillation frequencies of the BECs and is in good agreement with the simple model for the magnetic film (Chapter 2). We find the heating rate for atom clouds in the magnetic film microtrap is significantly lower than for those in the Z-shaped wire.

5.1 Collection, cooling and magnetic trapping

Loading the mirror magneto-optical trap. A schematic diagram of the experimental setup used to collect and laser cool a cloud of ^{87}Rb atoms and to then transfer the ultracold cloud to the atom chip is shown in Figure 5.1. We use the large reflective

surface of the chip (40 mm×46 mm) as part of a four-beam mirror magneto-optical trap (MMOT) [4]. The MMOT beams have a relatively large diameter of 30 mm limited by the size of the optical viewports and the quadrupole magnetic field is produced by a pair of external coils, to rapidly collect a large number of atoms near the atom chip surface [71]. The operating parameters of the MMOT, such as the power in each of the laser beams, the beam alignment, the trap laser detuning, the quadrupole field gradient and the centre position, have been optimised to achieve peak steady-state atom number. The trapping laser is detuned 18 MHz below the resonance of the D_2, $F = 2 \rightarrow F' = 3$ cooling transition of ^{87}Rb and is split into four separate beams, each with an intensity of 8 mW/cm^2. Two beams are aligned parallel to and centred ∼5 mm below the chip surface, while the other two are reflected from the gold coated surface of the chip at 45°. The repumping laser is locked to the D_2, $F = 1 \rightarrow F' = 2$ transition and is mixed with the four trapping beams, each with an intensity of 1 mW/cm^2. The quadrupole magnetic field is provided by two water-cooled coils (10 A/400 turns) positioned external to the vacuum chamber at 45° with respect to the atom chip surface. The field gradient along the axis of the coils is 0.1 T/m. The centre of the quadrupole field is then positioned 4.6 mm below the chip surface by applying small uniform magnetic fields ($0 - 0.2$ mT) produced by three additional sets of current-carrying coils in Helmholtz configuration (0-10 A/20 turns).

To load the MMOT we employ an alkali metal dispenser (SAES getters) in pulsed mode as a simple Rb source [72]. A typical MMOT loading curve is shown in Figure 5.2, measured by monitoring fluorescence from the MMOT with a sensitive photodiode. The experimental sequence begins at $t = 0$ when one Rb dispenser is resistively heated by a current of 6.5 A for 9.5 s. The partial pressure of Rb temporarily increases to $\sim 2 \times 10^{10}$ Torr and 4×10^8 atoms are collected over 15 s. The peak loading rate is 1.3×10^8 atoms/s. The dispenser current is then reduced to zero and the atoms are held in the MMOT for 25 s while the UHV pressure recovers to 2×10^{11} Torr. The

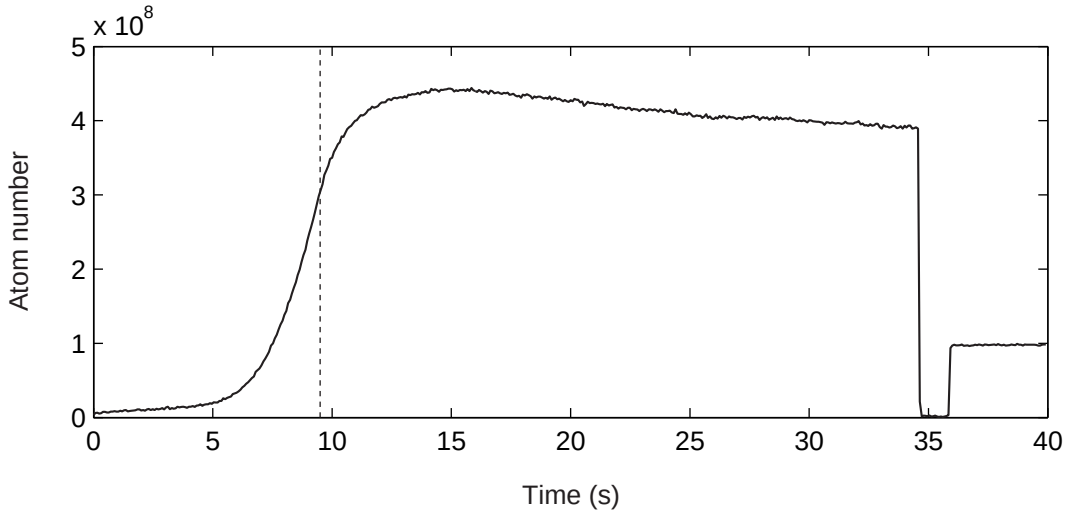

Fig. 5.2: A typical loading curve for the mirror magneto-optical trap (MMOT). The Rb dispenser is pulsed on with 6.5 A at $t = 0$ and off again at $t = 9.5$ s (dotted line) and the atoms are held in the MMOT for 25 s while the vacuum pressure recovers. At $t = 34.5$ the trapping light is shut off and the atoms are transferred to the Z-wire magnetic trap. After 1.2 s the atoms are recaptured into the MMOT where the fluorescence can again be monitored. The transfer efficiency to the magnetic trap is about 25 %.

overall loading time is 35 s and the experimental cycle can be repeated every 60 s*. An exponential fit to the decay curve of the trapped atoms for long hold times indicates that the MMOT lifetime is longer than 100 s. After the loading stage is complete the atom cloud has dimensions of $\sigma_{r,z} = 1.2$ mm. The cloud temperature is 90 μK, determined from ballistic expansion and absorption imaging.

The compressed U-wire magneto-optical trap. Transfer to the atom chip begins by substituting the quadrupole magnetic field produced by the external coils with the quadrupole magnetic field produced by current through the U-shape wire. This is performed by ramping off the external coils over 50 ms and by simultaneously ramping on the current through the U-shaped wire to 8 A and ramping on the uniform magnetic

*It is sometimes convenient to operate with a shorter loading time by applying a low current ($\sim$ 2 A) to the dispenser in a continuous mode (to maintain an elevated temperature below the Rb dispenser threshold) and by reducing the vacuum recovery time. In this way is possible to operate the experiment with a cycle time as short as 30 s.

field, B_{bias}, to 0.73 mT. The U-wire MMOT has three main roles targeted at obtaining a high transfer efficiency to the Z-wire magnetic trap. Firstly, the atoms are now confined by the wires on the atom chip which allow rapid switching of the magnetic field. Secondly, the U-wire MMOT is located 1.6 mm of the chip surface where it is possible to produce sufficiently large field gradients for the magnetic trap. Finally, the field gradient produced by the U-shaped wire ($\sim$0.4 T/m) is significantly larger than that produced by the external quadrupole coils. This reduces the size of the MMOT to $\sigma_y = 0.34$ mm and $\sigma_z = 0.74$ mm to provide better overlap and mode-match the transfer to the Z-wire magnetic trap. The increased density of the atom cloud in the compressed MMOT however heats the cloud to a temperature of 140 μK and reduces the MMOT lifetime to approximately 10 s.

Polarisation gradient cooling. To reduce the cloud temperature we apply a polarisation gradient cooling stage [73]. Polarisation gradient cooling works best in the absence of a magnetic field, so the proximity of the permanent magnetic film can potentially limit the cooling efficiency. Instead we leave the quadrupole magnetic field on and perform polarisation gradient cooling in the vicinity of the zero field position. To increase the volume over which polarisation gradient cooling is effective we turn off the trapping light for 1 ms and rapidly reduce the magnetic field gradient to 0.11 T/m (I_u=2.8 A, $B_{bias} = 0.25$ mT) while ensuring the centre of the quadrupole field does not shift. The cloud is then cooled by red detuning the trap laser by 56 MHz and reapplying the light for 2 ms. This procedure rapidly reduces the cloud temperature from 140 μK down to 40 μK. After this, the MMOT light is shut off and the U-wire current is switched to zero, leaving the atoms in a uniform magnetic field of $B_{bias} = 0.25$ mT.

Optical pumping. After polarisation gradient cooling, a 0.2 ms optical pumping pulse is applied to drive the atoms to the $|F = 2, m_F = +2\rangle$ magnetically trappable state. This pulse originates from a third laser, locked to the $F = 2 \rightarrow F' = 3$ cooling transition but frequency shifted by 217 MHz via a double-pass AOM. The actual laser frequency is close to the $F = 2 \rightarrow F' = 2$ resonance, where the detuning was chosen empirically to optimise the number of magnetically trapped atoms. We have found

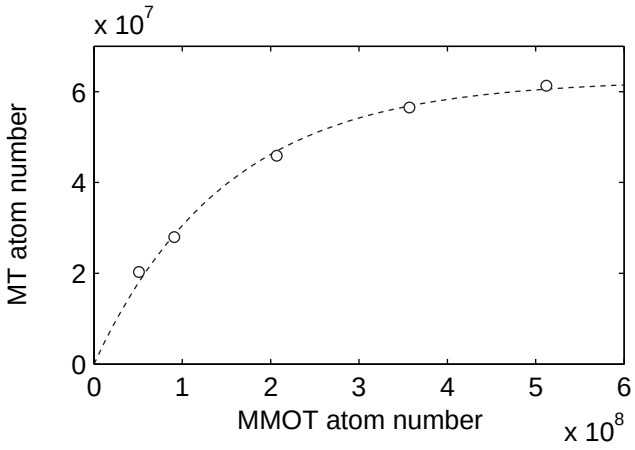

Fig. 5.3: Number of atoms transferred to the initial Z-wire magnetic trap. The number of atoms in the MMOT is varied and the number of magnetically trapped atoms is determined after 1 s through a resonant absorption image. The dashed curve is an empirical polynomial fit to the data.

our optimum conditions correspond to a detuning of +50 MHz. The optical pumping beam is 4 mm in diameter with a power of 2 mW, mixed with 5 mW of repumper light. The optical pumping pulse is applied along the x axis and has σ^+ polarisation with respect to the quantisation axis defined by B_{bias}. Typically the application of optical pumping increases the total number of magnetically trapped atoms by a factor of 5.

Transfer to the Z-wire magnetic trap. Next an Ioffe-Pritchard magnetic trap (MT) is formed 1.6 mm from the chip surface by passing 21.5 A through the Z-shaped wire and increasing B_{bias} to 1.3 mT. The magnetic field minimum of the initial Z-wire trap is approximately 0.3 mT to prevent spin-flip loss and to ensure the potential is roughly harmonic. Approximately 5×10^7 atoms remain trapped at a temperature of 50 μK. In Figure 5.3 the total number of atoms transferred to the initial MT is shown as a function of the total number of atoms in the MMOT. The data was taken by comparing integrated absorption images of atoms in the MMOT and then in the magnetic trap after 1 s. The transfer efficiency is limited mainly by the small volume and finite depth of the Z-wire magnetic trap and ranges between 10 % and 40 % for high initial atom numbers and low initial atom numbers respectively.

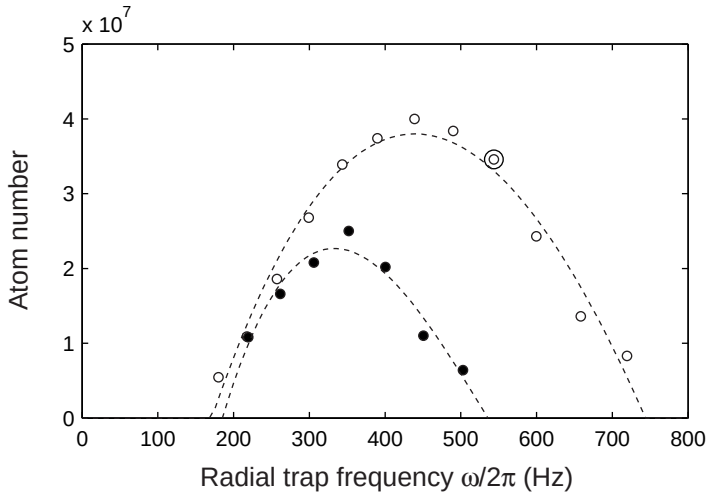

Fig. 5.4: Number of atoms held after 5 s in the Z-wire magnetic trap after compression by increasing the radial trap frequency. The compression stage moves the trap centre closer to the surface and ultimately limits the trap depth causing trap loss. The solid circles correspond to data for a Z-wire current of 25 A while the open circles are for a Z-wire current of 31 A. The double circle indicates the optimal conditions for maximising the elastic collision rate and evaporative cooling efficiency.

Compression of the magnetic trap. After the transfer to the initial magnetic trap, we compress the cloud by ramping the Z-wire current to 31 A and increase B_{bias} to 4.0 mT over 100 ms. This heats the cloud but also increases the elastic collision rate so that rethermalisation is rapid enough for evaporative cooling. The MT is approximately harmonic over the volume occupied by the trapped atoms as $m_F g_F \mu_B B_z(0) > k_B T$. The cloud averaged elastic collision rate is given by

$$\gamma_{el} = \bar{n}\sigma_{el}\bar{v}, \tag{5.1}$$

where $\bar{n}$ and $\bar{v}$ are the cloud averaged atomic density and mean thermal velocity respectively and in the s-wave collisional regime ($T < 300$ μK) $\sigma_{el} = 8\pi a_0^2$ is the elastic scattering cross section. Adiabatic compression increases both $\bar{n}$ and $\bar{v}$; however the phase space density of the cloud should remain constant. The compression is adiabatic if the rate of change of the trap frequency is small compared to the trap frequency

squared,

$$\epsilon = \frac{d\omega_{r,z}}{dt}\left(\frac{1}{\omega_{r,z}^2}\right) << 1. \tag{5.2}$$

For a 100 ms ramp of B_{bias}, the change of the axial trap frequency can be neglected and the radial trap frequency changes sufficiently slowly to satisfy the adiabatic criteria ($\epsilon \simeq 0.05$). Scaling laws can be easily derived that relate the relative increase in the radial trap frequency (ω_r'/ω_r) to the corresponding increase in cloud temperature, density and elastic collision rate [74, 75]. The scaling of the cloud temperature, atom density and elastic collision rate after two-dimensional adiabatic compression of the Z-wire magnetic trap is

$$\frac{T'}{T} = \left(\frac{\omega_r'}{\omega_r}\right)^{\frac{2}{3}}, \qquad \frac{\bar{n}'}{\bar{n}} = \frac{N'}{N}\left(\frac{\omega_r'}{\omega_r}\right), \qquad \frac{\gamma_{el}'}{\gamma_{el}} = \frac{N'}{N}\left(\frac{\omega_r'}{\omega_r}\right)^{\frac{4}{3}}. \tag{5.3}$$

In Figure 5.4 the total number of atoms remaining in the MT after a fixed hold time of 5 s is shown as a function of the radial trap frequency. For low values of B_{bias} ($\omega_r < 2\pi \times 300$ Hz) the trap depth is comparable to the cloud temperature and the total number of magnetically trapped atoms remains small. Increasing B_{bias} beyond 4.0 mT however ($\omega_r > 2\pi \times 550$ Hz) also results in a significant loss of atoms. This has been identified as a unique loss mechanism due to the presence of the relatively thick glass substrate (0.3 mm) situated between the trapped atoms and the Z-wire. Loss of atoms to the surface of an atom chip is usually prevented by the large field produced at the surface of the wire; however at the surface of the glass substrate this field is relatively small (about 1 mT) which limits the trap depth to approximately 700 μK. Although loss to the surface can be considered as a form of evaporative cooling as it preferentially removes energetic atoms from the trap [4], we find it to be inefficient compared to rf evaporation, leading to an excessive loss of atoms and a decrease in the elastic collision rate. The parameters of the compressed magnetic trap have been characterised and from Equation (5.3) we maximise the collision rate prior to the evaporative cooling stage. This is achieved for the compressed MT located 550 μm from the film surface

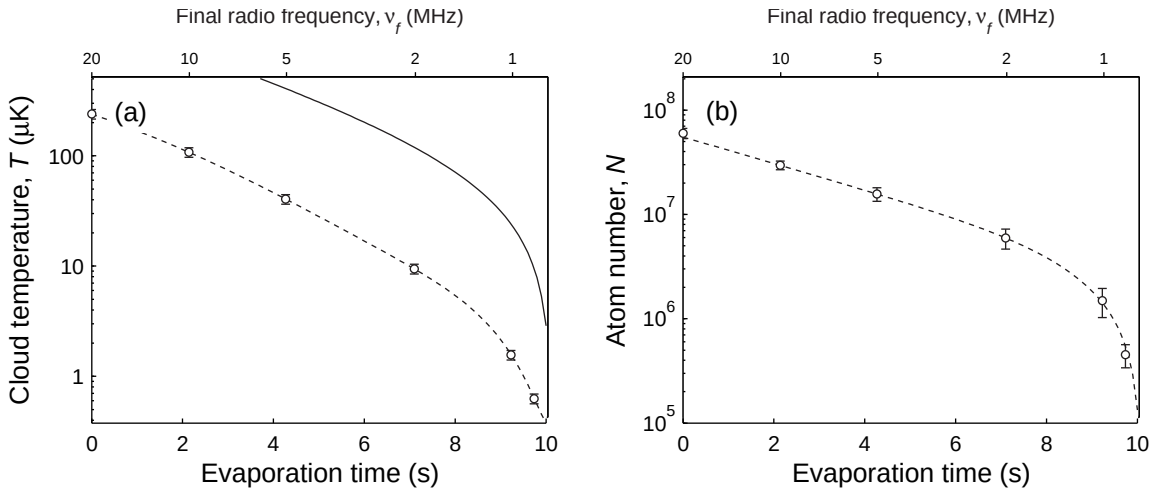

Fig. 5.5: Evolution of atom cloud parameters during evaporative cooling. (a) Cloud temperature measured using ballistic expansion and the trap depth (solid line) and (b) the total number of trapped atoms.

for I_z=31 A and $B_{bias} = 0.4$ mT. The radial and axial trap frequencies are $2\pi \times 530$ Hz and $2\pi \times 18$ Hz respectively. The cloud temperature is 240 μK with a peak density of $n_0 = 1.5 \times 10^{18}$ m^{-3}. The elastic collision rate is $\gamma_{el} = 160$ s^{-1}.

5.2 Radio frequency evaporation

Evaporative cooling. After compression, a preliminary radio frequency evaporative cooling stage is performed to lower the cloud temperature before the eventual transfer of atoms to the magnetic film microtrap. The rf antenna is formed with the two atom chip end-wires connected in series such that the currents are antiparallel to form a partial current loop. The rf magnetic field produced is oriented in the y direction, perpendicular to the trap axis to drive $\Delta m_F = \pm 1$ transitions. The proximity of the antenna to the magnetic trap means minimal rf power is required to outcouple the atoms. The radio frequency field for the evaporative cooling stage is generated by an unamplified 30 MHz rf synthesiser (Stanford Research Systems DS345), triggered to

produce a logarithmic frequency sweep of the form

$$\nu(t) = \nu_i \exp\left[-R \ln\left(\nu_i/\nu_f\right) t\right], \tag{5.4}$$

where ν_i is the initial radio frequency, ν_f is the final radio frequency and the duration of the ramp is R^{-1}. These parameters are programmed via the front panel of the DS345 with the values $\nu_i = 20$ MHz, $\nu_f = 0.78$ MHz and $R = 0.1$ s^{-1}. This provides a sweep from 20 MHz to 0.78 MHz over a 10 s period. The minimum of the trapping potential is $B_0 = 0.11$ mT (ν_0=0.77 MHz) such that the trap depth at the end of the rf ramp is ~ 1 μK. The rf signal applied to the end-wires begins at 2 V *rms* but is reduced to 0.5 V *rms* near the end of the ramp so that the power-broadened rf linewidth is smaller than the spectral width of the cloud. The calibrated Rabi frequency of the rf transition is $2\pi \times 1.43$ kHz/V, which is about 50 times less than the value expected from a simple calculation taking into account the load resistance, the geometry of the antenna and the position of the trap. This discrepancy is attributed to poor impedance matching of the rf source to the end-wire antenna as this was given no special consideration. During the 10 s radio frequency ramp we also compress the Z-wire trap by reducing I_z to 25 A, moving the trap to within 300 μm of the surface and increasing the radial trap frequency to $2\pi \times 650$ Hz. Surface induced loss does not play a significant role here as the trap depth is already limited by the rf field. After the rf ramp the frequency of the synthesiser jumps back to 20 MHz and the amplitude is set to zero.

In Figure 5.5 experimental data is presented for the evolution of the cloud temperature and the remaining number of atoms in the compressed Z-wire trap during evaporation. The final data point at $t = 9.75$ s corresponds to $\nu_f = 0.85$ MHz (trap depth ~ 7.7 μK). The cloud temperature would typically be measured by switching off the trap at various intervals during the rf sweep and measuring the ballistic expansion rate. This is complicated however by the presence of relatively large field gradients from the film at the trap position which accelerates the cloud away from the surface (Section 2.3). To overcome this, we first adiabatically decrease B_{bias} over 50 ms to move the cloud to a new trap 1 mm from the surface where the

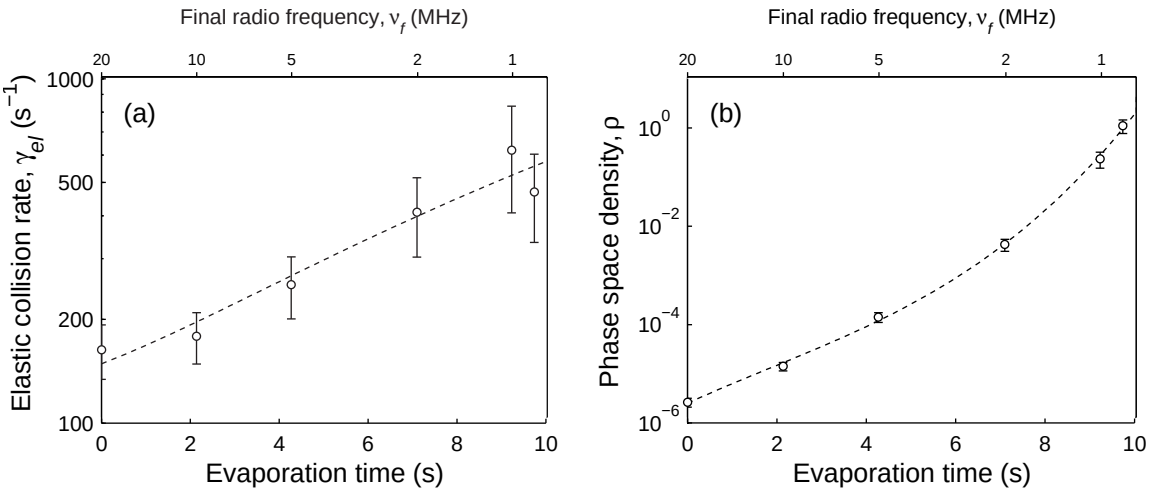

Fig. 5.6: Evolution of atom cloud parameters during evaporative cooling. (a) Cloud averaged elastic collision rate and (b) the phase space density of the cloud.

permanent magnetic field gradients are negligible. This 'imaging trap' is characterised by a radial trap frequency of $2\pi \times 300$ Hz and the cloud temperature after adiabatic decompression is easily related from Equation (5.3) to that in the original compressed trap ($\omega_r'/\omega_r = 0.46$). After transfer to the imaging trap the Z-wire is switched off and the cloud is allowed to expand. A series of absorption images for different expansion times is recorded and axial cloud cross-sections fit to a gaussian distribution to calculate the ballistic expansion rate. We also determine the total number of atoms from the integrated absorption. We find that the cloud temperature decreases steadily as the trap depth is decreased and corresponds to a truncation parameter $\eta > 10$ [74].

In addition to the cloud temperature and atom number during evaporative cooling it is also possible to calculate several other useful properties of the cloud. For example in Figure 5.6 the evolution of the atomic elastic collision rate and the phase space density of the cloud are shown, as derived from measurements of the trap frequency, cloud temperature and the total atom number. Notably, the collision rate begins at approximately 160 s^{-1} but increases to about 500 s^{-1} as the evaporation proceeds. This is indicative of run-away evaporative cooling and therefore the cooling efficiency remains high throughout the sweep [74]. The primary parameter of interest is the phase

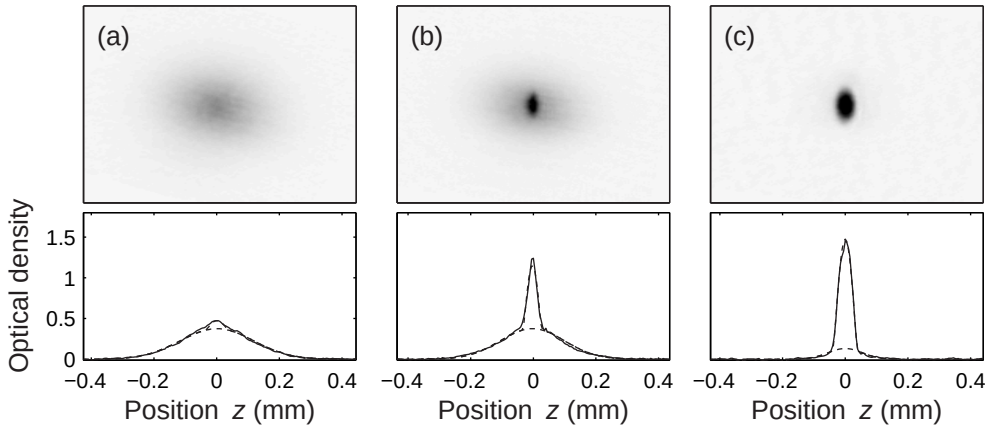

Fig. 5.7: Observation of Bose-Einstein condensation in the Z-shaped wire magnetic trap. (a) A thermal cloud is produced for a trap depth of 6.7 μK, (b) a bimodal distribution at a trap depth of 3.4 μK and (c) a Bose-Einstein condensate for a trap depth of 1 μK.

space density of the cloud, ρ. This increases continuously during the 10 s evaporation sweep, by almost six orders of magnitude, to a final value of > 1 where the Bose-Einstein condensation transition occurs. The efficiency of evaporative cooling ($-\log(\rho)/\log(N)$) is 3.2 ± 0.1 [12].

5.3 Bose-Einstein condensation

The Bose-Einstein condensation transition. To form a BEC using the Z-shaped wire magnetic trap the 10 s rf ramp is uninterrupted and allowed to continue to a final frequency of $\nu_f = 0.78$ MHz. With our parameters the critical temperature for condensation is $T_c = 530$ nK, which is reached with $N = 2 \times 10^5$ atoms. Figure 5.7 shows absorption images of clouds following 15 ms of ballistic expansion from the imaging magnetic trap. The three images show atom clouds after ballistic expansion for rf ramps interrupted at trap depths of 6.7 μK ($\nu_f - \nu_0$=70 kHz), 3.35 μK (35 kHz) and 1 μK (10 kHz), revealing a thermal cloud, a partially condensed cloud (characterised by a bimodal density distribution) and an almost pure Bose-Einstein condensate respectively. Each image has also been fit to a two-dimensional

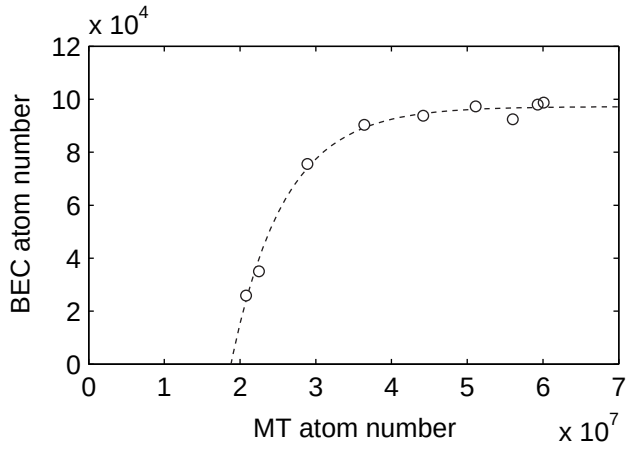

Fig. 5.8: Effect of initial magnetic trap atom number on the number of condensed atoms. Strong asymptotic behaviour is associated with three-body recombination loss which stabilises the total number of condensed atoms.

bimodal distribution consisting of a gaussian 'thermal' component and a Thomas-Fermi 'condensate' component integrated in one-dimension. In Figure 5.8 we show the total number of atoms in the condensate after evaporation as a function of the initial number of magnetically trapped atoms. The strong asymptotic behaviour which saturates at 1.0×10^5 Bose-condensed atoms is attributed to the high three-body loss rate (Γ^{-1} <3 s) near the end of the evaporation sweep which stabilises the final number of condensed atoms. The chemical potential of the condensate in the Z-wire trap is $\mu/h = 3.9$ kHz. We find that 2×10^7 atoms in our magnetic trap before starting evaporation is sufficient to reach the run-away evaporative cooling regime; however larger numbers do improve the shot-to-shot reproducibility of the experiment. By increasing the rf ramp rate at the end of the sweep or by weakening the trapping potential to reduce the peak atomic density during evaporation it is also possible to reduce the effect of three-body loss and thereby produce larger condensates [76, 77], although this technique has not yet been pursued for this experiment. The BEC lifetime in the Z-wire magnetic trap is approximately 100 ms while the total number of atoms in the trap remains constant over this time indicating that the decay is mainly limited by in-trap heating. The BEC lifetime can be extended to approximately 1 s by limiting the trap depth to

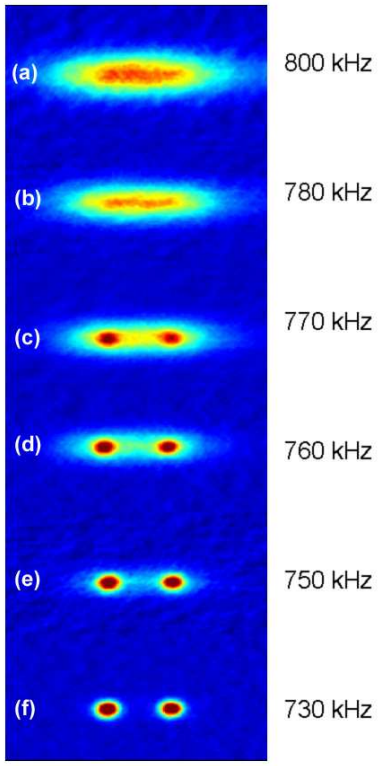

Fig. 5.9: Observation of double Bose-Einstein condensates formed in the permanent magnetic film trap. As the final radio frequency is reduced from 800 kHz we observe (a-b) a single thermal cloud distribution, (c-e) a double peaked bimodal distribution and (f) two nearly pure Bose-Einstein condensates separated by 170 μm.

approximately 5 μK with an rf shield [48].

Transfer to the magnetic film microtrap. Transferring the ultracold atom cloud to the magnetic film microtrap is relatively simple. First preliminary evaporative cooling of the atom cloud is performed in the Z-wire magnetic trap. The sweep is truncated at 8.8 s (1.15 MHz) at which point the total number of trapped atoms is 2×10^6 and the cloud temperature is approximately 3 μK. Over 100 ms the Z-wire current and B_{bias} is ramped down to 2.5 A and ~ 0.8 mT respectively while the current to the end wires is increased to 6 A to maintain axial confinement. The ramp weakens the trap potential and positions the atom cloud ~ 100 μm from the film surface. Here the field strength (~ 0.4 mT) and field gradient (~ 4 T/m) produced by the film in combination with B_{bias} is expected to hold the atoms against gravity. Over another 50 ms the Z-

wire current and B_{bias} are ramped to 0 A and 0.47 mT respectively, during which the position of the atom cloud does not significantly change. Finally the ultracold atom cloud is confined by the potential formed using the permanent magnetic film. Once the atom cloud is transferred to the magnetic film microtrap we trigger a second rf evaporative cooling sweep from 1.5 MHz to 0.73 MHz over 2 s. Strikingly, as the cloud temperature reduces below the transition temperature we observe the growth of *two* high density peaks in the axial density distribution (Figure 5.9). This surprising observation is further discussed in Chapter 6 where we explore the effect of magnetic field corrugations discovered near the film surface on the trapped atoms. By the end of the rf sweep two pure Bose-Einstein condensates are produced, each consisting of 1×10^5 atoms and separated by 170 μm.

5.4 Characterising the magnetic film microtrap

Probing the magnetic field of the film. A magnetically trapped cloud of cold atoms or a BEC can behave as a sensitive probe to the local magnetic field. For example the field from the film as a function of the trap position $B_{film}(y)$ can be inferred by calibrating the applied bias field B_{bias} and measuring the cloud position using absorption imaging. In addition the magnetic field gradient of the film $B'_{film}(y)$ can be inferred by measuring the trap oscillation frequency $\omega_r(y)$ related by Equation (2.10).

Neglecting non-magnetic sources of potential energy, the trap minimum (and subsequently the BEC) is located at the position where the uniform bias magnetic field is equal in magnitude to and cancels with the field from the film ($B_{bias} = -B_{film}$). The uniform magnetic field can be increased (decreased) to move the trap minimum closer to (further from) the film surface. A measurement of $B_{film}(y)$ can then be compared with a simple model for the magnetic field produced by the magnetic film to determine the magnetisation-thickness product δM.

To perform the measurement we first ensure the magnification of absorption images is well known by first calibrating the effective pixel size against the acceleration of a BEC after release under gravity from the Z-wire magnetic trap. To avoid any systematic

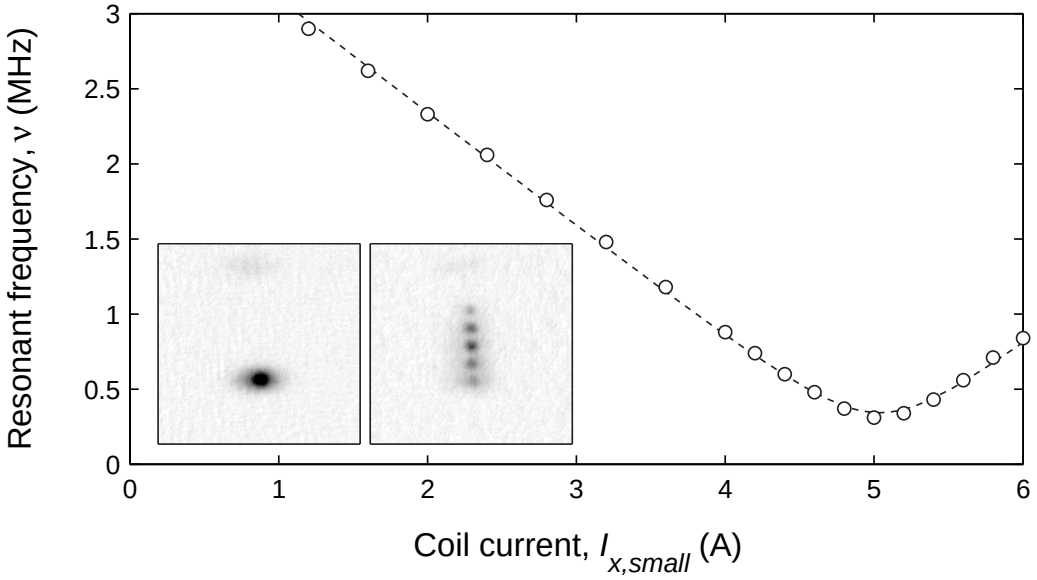

Fig. 5.10: Stern-Gerlach calibration of the bias magnetic field. The atom cloud is released from the trap and falls under gravity in a uniform bias field controlled by $I_{x,small}$ (inset-1). The Zeeman energy is found by tuning the rf source to the required resonant frequency ν to couples the five Zeeman levels. A field gradient is then applied using the Z-wire to spatially separate each component (inset-2). The dashed line is a fit to the data used to extract the magnetic field strength as a function of $I_{x,small}$.

contribution to the acceleration caused by the permanent magnetic field gradient we leave the Z-wire current on but release the atoms by first pulsing a resonant rf field in order to transfer a fraction of the BEC to the $m_F = 0$ magnetically insensitive state. Absorption images record the position of the cloud at various time intervals after the rf pulse and the pixel size is constrained such that the measured acceleration (originally in pixels/s^2) matches the known gravitational acceleration (9.8 m/s^2). The pixel size determined in this way (5.0 μm/pixel) is also consistent with a calibration performed by imaging a reference rule external to the vacuum apparatus.

It is also important to accurately calibrate the strength of B_{bias}. Usually the field strength at the centre of the vacuum chamber can be calculated using the Biot-Savart law with the known coil dimensions, however, we have observed a systematic discrepancy between the expected and observed field strengths in our system. This has

subsequently been attributed to the Kovar (NiFe alloy) magnetic sleeves used in the UHV optical view ports which in our setup results in a ∼20% attenuation of the actual field strength. In order to accurately measure the field near the atom chip we measure the resonant frequency of a rf pulse for a BEC falling through a uniform magnetic field set by an external set of current-carrying coils. In our experiments we use two sets of coils to produce fields in the $+x$ and $-x$ directions, labelled B_{bias} and $B_{x,small}$ respectively. B_{bias} is typically used as the uniform bias field to produce the magnetic trap, which can produce a field strength greater than 5 mT but has a long time constant and is difficult to switch rapidly. $B_{x,small}$ is used to produce smaller fields with rapid switching times which can be used to reduce the total field strength along x for fine tuning of B_{bias}. It is necessary to calibrate both sets of coils.

Shown in Figure 5.10 is the calibration of $B_{x,small}$. First a BEC is produced in the Z-wire trap, which is subsequently switched off to release the BEC. Once the BEC drops to a position where the field of the film can be neglected, current is applied to both coils; one is oriented along the $+x$ direction with a constant magnitude of $B_{bias} = 0.55$ mT to offset the local field strength to a convenient value, and a second is produced by a well defined variable current $I_{x,small}$ applied to the coils which control $B_{x,small}$. After 5 ms a 40 μs resonant rf pulse is applied to couple the various Zeeman states. The resonant frequency depends on the total field strength at the atoms location. Immediately, the uniform fields are switched off and the Z-wire is switched back on at 31 A to produce a magnetic field gradient which causes the various Zeeman components to separate via the Stern-Gerlach force. Finding the resonant frequency of the rf pulse requires some patience, but can be accurately determined to within $\sim$ 1 kHz which for ^{87}Rb in $|F = 2, m_F = 2\rangle$ corresponds to a magnetic field resolution of 0.14 μT. The resonant frequency ν is found for a range of $I_{x,small}$ values (Figure 5.10) and is fit to the dependence $B_{x,small} = m_F h\nu/\mu_B = \left((aI_{bias} + 0.55 \times 10^{-3})^2 + b^2\right)^{1/2}$ to accurately determine the magnetic field calibration factor $a = -109$ μT/A. The fit parameter $b = \sqrt{B_y^2 + B_z^2} = 49$ μT is the combined stray magnetic field in the y and z directions. The calibration of B_{bias} is also performed using this technique and yields a calibration

factor of $a = +174\ \mu$T/A.

With B_{bias} and an accurate measurement of the image magnification it should be possible to determine $B_{film}(y)$ and δM. However two additional considerations complicate the result. First, the absolute position of the magnetic film with respect to the absorption image is uncertain, as the magnetic film-coated substrate is not directly visible in the absorption images, a consequence of unevenly cured epoxy and the resultant overhang of the blank substrate. The distance between the film edge and the blank substrate (which is visible in the images) must therefore be treated as a free parameter. Second, the calibration factor for B_{bias} is accurately known from the Stern-Gerlach measurement below the chip but any residual magnetic field at the chip surface (for $I_{bias} = 0$) is unknown and is also treated as a free parameter. With these additional free parameters we found it impossible to unambiguously extract $B_{film}(y)$ and δM through measurement of the trap position alone.

To overcome this problem, we make a second set of measurements to provide more information about the field from the film. Small centre of mass oscillations of a BEC at frequencies up to 10 kHz can be measured accurately over many periods due to the inherently low damping rate and small spatial extent of the cloud [78]. Here we measure the radial trap frequency to within 10 Hz ($\sim 1\%$ accuracy) after 'kicking' the BEC. To do this we increase B_{bias} by approximately 5%, which displaces the BEC and then return to the original value within 2 to 5 ms (chosen to be approximately half the estimated trap period). After waiting a variable time for oscillations the cloud is released from the trap for 10 ms by switching B_{bias} to zero and the cloud position is recorded via imaging. In this measurement the influence of the magnetic film is advantageous as the subsequent acceleration from the surface depends strongly on the position of the cloud before release, amplifying the oscillation amplitude after expansion. A typical measurement of the oscillation frequency is shown in Figure 5.11. The trap oscillation frequency was accurately measured for values of B_{bias} ranging from approximately 0.2 mT to 0.7 mT, covering the same range as the trap position measurements. In addition to the radial trap frequency, the magnetic field minimum

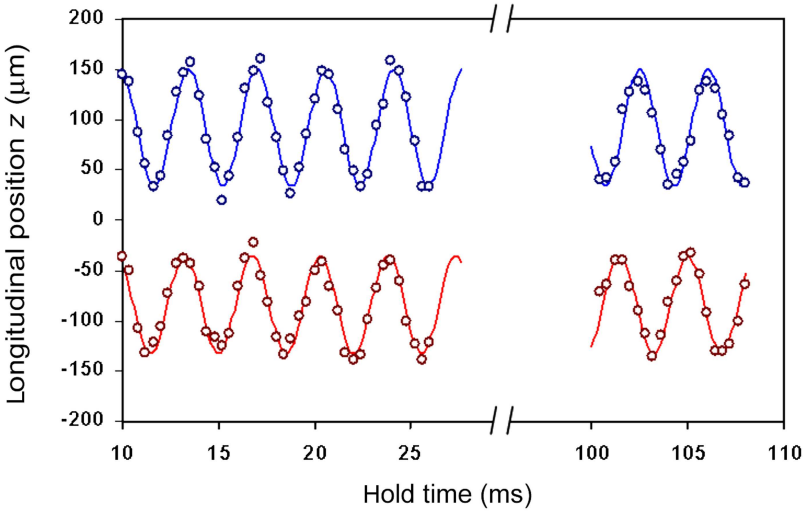

Fig. 5.11: (Colour) Measurement of radial centre of mass oscillations for the double BEC confined in the magnetic film microtrap for the (upper dataset) right potential well and the (lower dataset) left potential well. Oscillations are induced by suddenly changing B_{bias} by approximately 5% then back again over 4 ms. The cloud position y is then measured after 15 ms ballistic expansion. For presentation the centre points of the oscillations are subtracted and the two data sets are offset by ± 100 μm. The fit oscillation frequencies are (right well) $\omega_r = 2\pi \times 281$ Hz and (left well) $\omega_r = 2\pi \times 283$ Hz.

B_0 is measured by applying a weak, continuous rf field and observing trap loss. The minimum frequency that gives loss corresponds to the value of the magnetic field at the trap minimum B_0. The measurement of trap frequency $\omega_r(y_0)$ in combination with the trap bottom B_0 unambiguously determines the local magnetic field gradient through Equation (2.10). The data for the magnetic field strength and magnetic field gradient produced by the film as a function of B_{bias} is then fit self-consistently to the expected dependence for the uniformly magnetised film, including the effect of gravitational sag (Figure 5.12). We find good agreement between the best-fit value for $\delta M \sim 0.18$ A and the expected value given from SQUID analysis $\delta M \sim 0.20$ A justifying the use of the simple model. Moreover, from the fit we infer the distance between the magnetic film edge and the blank substrate edge to be ~ 30 μm and the calibrated value of the absolute magnetic field is $B_{bias} = (0.174\ I_{bias} - 0.130)$ mT. The field offset (0.13 mT) is assumed to originate partially from the Earth's geomagnetic field and from the residual

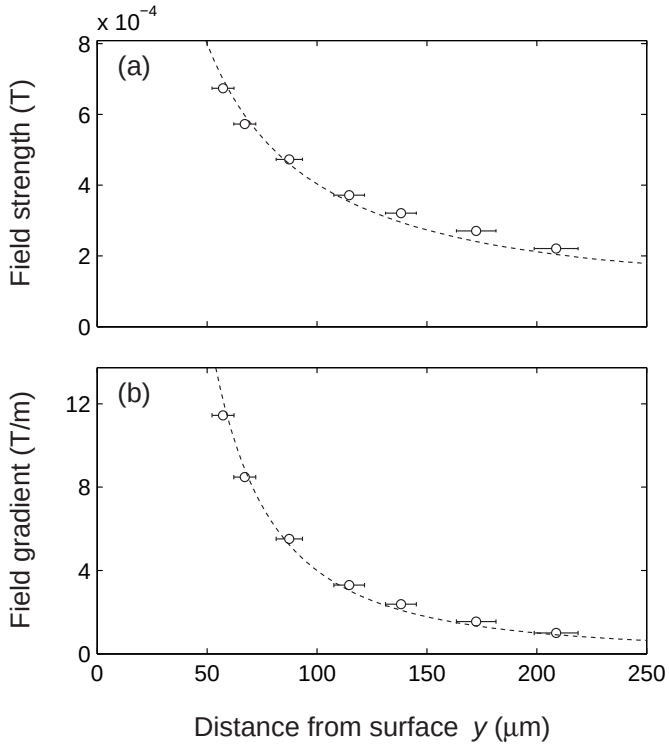

Fig. 5.12: The magnetic field strength (a) and magnetic field gradient (b) produced by the magnetic film both follow the predictions of a simple model for $\delta M = 0.2$ A (dotted lines).

magnetisation of some unidentified mounting components.

Trap lifetime and heating rate. In addition to characterising the magnetic film microtrap we perform measurements on ultracold thermal clouds to determine the trap lifetime and heating rate near the film surface. Thermal atom clouds just above the BEC transition temperature are used in the following measurements to minimise any density dependent loss or heating [49].

The lifetime measurement involved simply loading the magnetic film microtrap, performing a secondary evaporative cooling stage followed by a 50 ms ramp of B_{bias} to position the trapped atoms at the desired distance from the film surface. At this position the atoms are held for a variable time and then released from the trap by switching off B_{bias}. After a few milliseconds of expansion the cloud is imaged and the absorption is integrated to give the total remaining atom number. The atom number is

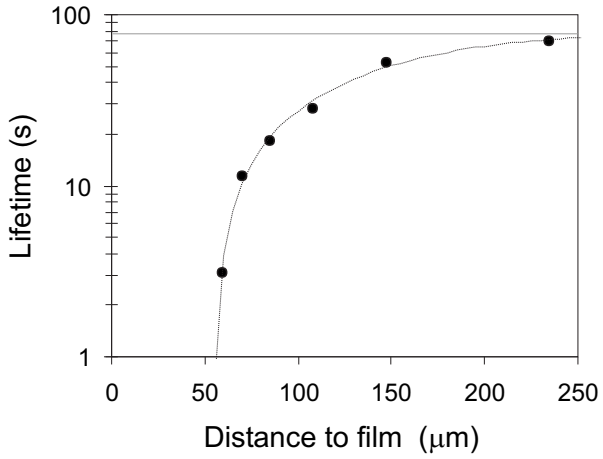

Fig. 5.13: Trap lifetime for ultracold thermal atoms in the magnetic film microtrap as a function of distance to the film surface. For large distances ($y_0 > 200$ μm) the lifetime is ≈ 72 s, presumably limited by background collisional loss. Closer to the surface ($y_0 \sim 50$ μm), strong loss is observed which may be attributed to the proximity of the protruding gold surface.

fit to a single exponential decay as a function of hold time and the extracted decay time constant is plotted in Figure 5.13. At large distances from the film surface ($y > 200$ μm) we measure an extremely long trap lifetime of 72 s which is attributed mainly to losses due to background collisions. The asymptotic behaviour to very short lifetimes for close proximity to the film surface ($y_0 \sim 50$ μm) may be due to interactions with the protruding gold coated 'blank' substrate expected at $y \sim 30$ μm, although density dependent loss caused by the associated increase in trap frequency at these distances cannot be excluded. The observed loss near the surface may also be caused by spin-flip transitions due to thermal Johnson noise in the conducting gold overlayer [24].

In addition to trap loss, in-trap heating ultimately limits the lifetime of a trapped BEC. Here we estimate the heating rate due to technical noise by positioning the magnetic film microtrap at $y = 210$ μm where the radial trap frequency is measured to be $\omega_r = 2\pi \times 120$ Hz. The trap depth is limited by B_{bias} and is approximately 0.22 mT (150 μK). For each hold time we release the cloud by switching off B_{bias} and measure the axial size as a function of expansion time from which we extract the cloud

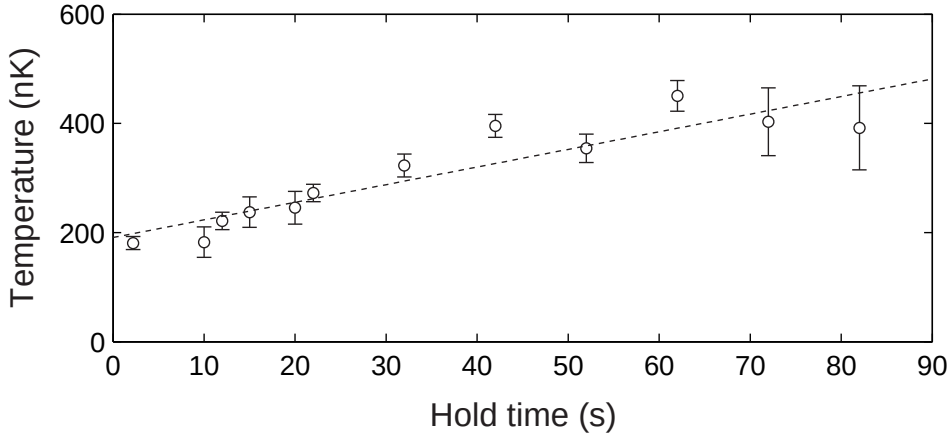

Fig. 5.14: Heating rate of an ultracold thermal cloud trapped in the magnetic film trap positioned 210 μm from the film surface. The temperature increases approximately linearly with hold time over ~ 80 s indicating a remarkably low heating rate of 3.2 ± 0.5 nK/s.

temperature. The cloud temperature increases approximately linearly in time and corresponds to a remarkably low heating rate of 3.2 nK/s [79]. To our knowledge this is the lowest heating rate observed with an atom chip to date and is almost two orders of magnitude lower than the heating rate found using our Z-wire trap under similar conditions, measured as 270 nK/s. Other measurements indicate that the heating rate increases as the trap is positioned closer to the surface. The measured heating rate for the magnetic film microtrap at a position of $y_0 = 90$ μm, where the trap frequency $\omega_r = 2\pi \times 700$ Hz, is found to be 23 nK/s, although the ballistic expansion measurements become complicated due to the proximity to the magnetic film. Efforts to trap atoms in the $|F = 1, m_F = -1\rangle$ magnetic state and to resonantly outcouple atoms to $m_F = 0$ will allow a more systematic study of the low heating rates observed using the magnetic film microtrap.

Chapter 6

The effect of magnetisation inhomogeneity

In this chapter a study is presented on the longitudinal fragmentation of trapped atoms confined near the surface of the magnetic film. An anomalous spatially varying component of the magnetic field oriented along the trap axis is found to corrugate the trap potential resulting in fragmentation of the atomic cloud. To accurately profile the magnetic potential we have developed a new technique which incorporates radio frequency spectroscopy and high resolution optical imaging of the atoms. A comparison of the fragmentation observed near the magnetic film surface with that near the adjacent non-magnetic gold surface indicates the variations originate from long range inhomogeneity in the film magnetisation rather than imperfections of the film edge. A model which takes into account two-dimensional random variations of the film magnetisation is developed and compared with the observations. Finally, the properties of the magnetic film are studied using a home-built scanning magneto-resistance microscope, after the atom chip is removed from the vacuum chamber. The magneto-resistance measurements are in agreement with the results obtained using rf spectroscopy and indicate that the homogeneity of the magnetic film may be improved for lower bake-out temperatures. Results of this chapter have also been accepted for publication in Physical Review A (2007) [80].

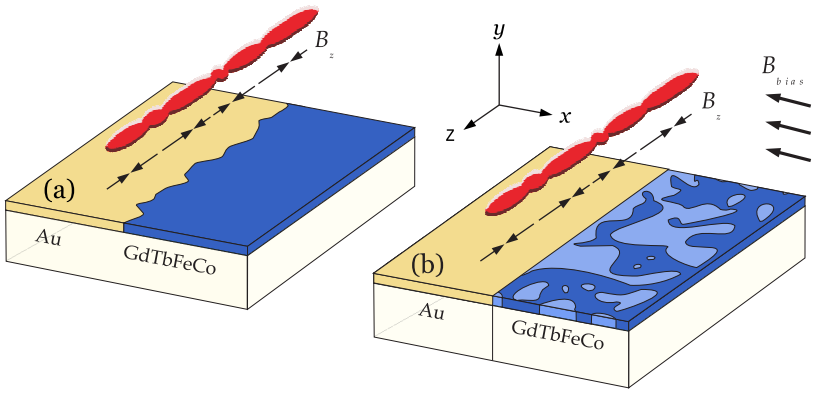

Fig. 6.1: (Colour) Schematic diagram of a permanent magnetic film atom chip. (a) Fluctuations of the magnetic film edge or (b) inhomogeneity in the film magnetisation cause small variations of the magnetic field along the trap axis, resulting in fragmentation of ultracold atom clouds.

6.1 Fragmentation on atom chips

Early experiments with atom chips revealed that clouds of ultracold atoms tend to fragment into clumps when brought in close proximity to current-carrying wires. Fragmentation was originally observed for ultracold atoms confined in magnetic microtraps located less than 100 μm from electroplated wires [8, 17], near machined silver foil wires [60], and recently also permanent magnetic materials [27, 28]. Experiments with current-carrying wires first identified small anomalous spatial magnetic field variations parallel to the trap axis, caused by tiny deviations in the current flow [81,82]. These variations corrugate the bottom of the magnetic potential at a level that can significantly affect the density distribution of the ultracold atom cloud. The variations were ultimately traced to roughness of the wire edges [18, 19] and have subsequently been reduced through the use of high quality lithographic and metal vapour deposition techniques as well as focused ion beam milling to produce extremely straight wires [20, 21]. Recently, dynamic methods to suppress fragmentation have been applied with some success by modulating the wire current [22]. Although the origin and reduction of fragmentation near current-carrying wires has been the topic of

numerous experimental and theoretical studies, no similar understanding yet exists for fragmentation near permanent magnetic materials. This study is the first quantitative analysis of fragmentation observed near the surface of a permanent magnetic film atom chip. In this case corrugations of the magnetic field may originate from structural imperfections in the film such as roughness of the film edge or imperfect patterning (Figure 6.1a) or additionally may be caused by inhomogeneity in the film magnetisation itself (Figure 6.1b).

6.2 Spatially resolved rf spectroscopy

Ultracold atoms are ideally suited as small and highly sensitive probes of small variations in potential energy due to the associated narrow energy distribution. This property has been exploited in several precision measurements of small forces near surfaces [78, 83]. In particular, a new magnetic field microscope has been demonstrated where the equilibrium distribution of an elongated BEC was used to image the magnetic field landscape near a 'test' wire, both with high sensitivity (300 pT) and high spatial resolution (3 μm) [14]. In this work we extend these ideas by accurately measuring the magnetic field landscape near the permanent magnetic film surface using spatially resolved radio frequency (rf) spectroscopy of trapped atoms.

In the past rf spectroscopy has been used to spectroscopically determine the energy distribution of a thermal atom cloud [84, 85], measure the spatial distribution of a harmonically confined condensate through rf outcoupling [86], study collisional shifts in ultracold fermionic gases [87] and to measure the pairing gap in a strongly interacting fermionic gas [88]. We show that spatially resolved rf spectroscopy of trapped atoms is well suited for mapping the magnetic field near the permanent magnetic film atom chip and can also be applied to other magnetic field sources. The basic concept of the technique is shown in Figure 6.2. The density distribution of a cloud of ultracold atoms in thermal equilibrium with the confining potential is shown in blue. A radio frequency field of frequency ν outcouples atoms from the magnetic potential at regions where the Zeeman energy splitting is equal to $h\nu$. The radio frequency is swept from a

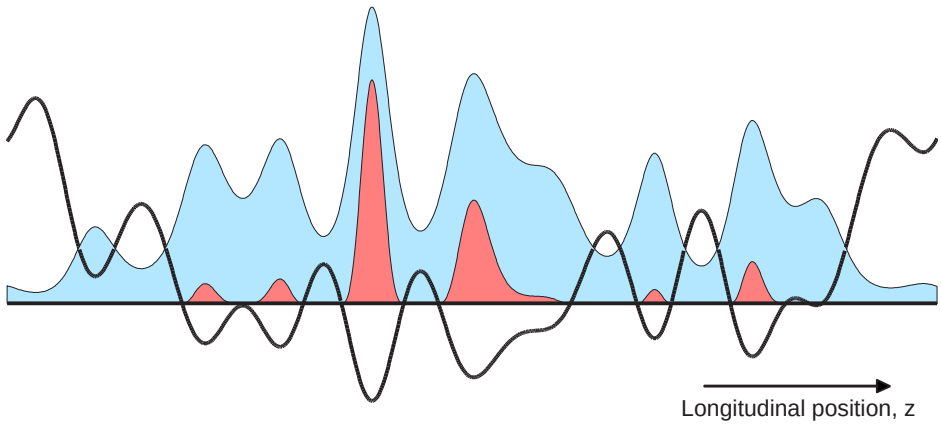

Fig. 6.2: (Colour) Technique of radio frequency spectroscopy used to measure the random magnetic potential. The corrugated longitudinal potential (solid black line) causes the fragmentation. The equilibrium distribution of atomic density is shown as a blue shaded area. A radio frequency field (resonant frequency indicated by the solid horizontal line) truncates the thermal distribution (red shaded area) such that regions of the potential above the resonant frequency remain unpopulated.

large value ν_i, corresponding to high magnetic field strength, to a final radio frequency ν_f. The sweep ensures that all atoms with energy larger than $m_F h\nu_f$ are lost from the trap which truncates the thermal distribution (Figure 6.2 shaded red). Immediately after the sweep an optical absorption image records the truncated density distribution. The process is then repeated for several values of ν_f. For each position z there is a value of ν_f for which the atomic density suddenly decreases to zero, corresponding to the radio frequency that is resonant with the local minimum of the magnetic potential.

The main advantages of spatially resolved rf spectroscopy are:

- the measured magnetic field strength is intrinsically calibrated and does not require accurate knowledge of the temperature or energy distribution of the atom cloud,

- the magnetic contribution to the total potential can be distinguished from gravitational tilt or electrostatic forces near the surface by comparing the rf spectrum to the equilibrium distribution of trapped atoms, and

- there is no strict requirement of thermal equilibrium across the whole potential, which is difficult to achieve when probing spatially large regions of the magnetic field or strongly corrugated potentials.

6.2.1 Experimental procedure

The preparation of an ultracold cloud of atoms confined near the permanent magnetic film follows the description given in the previous chapter. In summary, atoms are collected in a MMOT and subsequently transferred to the magnetic trap formed by the Z-shaped current-carrying wire and a bias magnetic field B_{bias}. A preliminary rf evaporative cooling stage with a logarithmic radio frequency sweep from 20 MHz to 2 MHz reduces the cloud temperature below 5 μK and the total number of atoms to 1×10^6. The cloud is then adiabatically transferred to the magnetic film microtrap over 250 ms by reducing the current through the Z-wire to zero. The values of B_{bias} can be tuned from 0.2 mT to 0.8 mT so that the transverse trap frequency varies between $2\pi \times 410$ Hz and $2\pi \times 1500$ Hz. The trap position ranges from 200 μm and 50 μm from the film surface, directly below the edge. The end-wires are operated at 0.5 A such that the trap depth is $\sim$100 μK and the thermal cloud extends along 5 mm of the atom chip surface.

A second rf field of frequency ν is then applied through the end-wires from an additional rf source which resonantly outcouples atoms from the trap at positions which satisfy the resonant condition

$$g_F \mu_B |B(x, y, z)| = h\nu, \tag{6.1}$$

where g_F is the Landé g factor, μ_B is the Bohr magneton and h is Planck's constant. For ^{87}Rb atoms in $|F = 2\rangle$, the calibration parameter is $g_F \mu_B / h = 7.0$ kHz/μT. The rf field is swept over 4 s using a single logarithmic frequency ramp from $\nu_i = 2$ MHz to a final cut-off frequency ν_f that ranges from 1.4 MHz to 0.5 MHz. The ramp rate varies between 700 kHz/s and 170 kHz/s. The amplitude of the rf field is

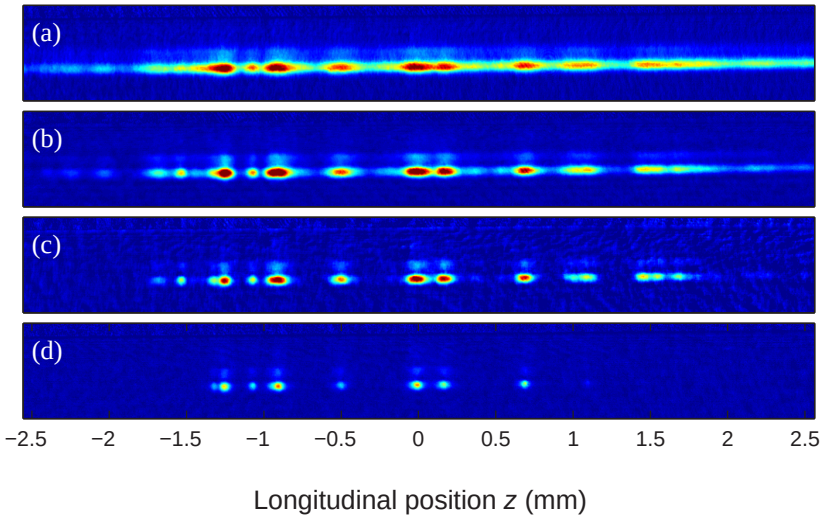

Fig. 6.3: (Colour) Absorption images of the atomic density in the magnetic film microtrap located $y = 67$ μm from the surface. As the rf cut-off ν_f is decreased, the structure of the potential is revealed: (a) ν_f=1238 kHz, (b) ν_f=890 kHz, (c) ν_f=766 kHz, (d) ν_f=695 kHz.

140 nT corresponding to a Rabi frequency of $2\pi \times 0.53$ kHz. The duration of the sweep should be long compared to the time required for resonant atoms to be outcoupled from the the trap region (between 1 and 2 ms) and for regions of the potential where $g_F \mu_B |B| \geq h\nu_f$ to remain unpopulated. This is confirmed by sweeping to a low value of ν_f and ensuring that all atoms are lost from the trap. The sweep duration should however not be long compared to the trap lifetime or the rethermalisation time. During the early stages of the rf sweep we find the cloud temperature decreases slightly due to collision assisted evaporative cooling. However toward the end of the sweep the resonant frequency approaches that corresponding to the local trap bottom and the cloud becomes significantly truncated by the rf field after which the cloud temperature remains fixed. Immediately after the sweep B_{bias} is switched off for 1 ms before imaging during which the atom cloud moves a distance of > 100 μm from the surface and expands in the radial direction. A resonant absorption image is then recorded with a spatial resolution of 5 μm. Expansion of the atomic cloud in the longitudinal direction can be neglected on this timescale and the absorption image provides an accurate

measurement of the in-trap density distribution. The rapid switch-off also transfers a small fraction of atoms to the $m_F = +1$ state which are displaced less by the magnetic field gradient and can be excluded from the analysis.

A series of measurements were performed to reconstruct the magnetic field landscape at a fixed distance from the surface. First the approximate field strength at the minimum of the magnetic potential is found. Then an appropriate range of values for ν_f is selected, such that for large values of ν_f the truncated distribution remains mostly unfragmented, with atoms occupying all regions of the potential, while for low values of ν_f atoms remain only in the lowest of the potential wells. This process is repeated 40 times, once for each value of ν_f. A subset of absorption images for different values of ν_f is shown in Figure 6.3. The absorption images are then integrated over y to give the one-dimensional line density, $n(z)$, and are compiled into a two-dimensional data set, $n(z, \nu_f)$ (Figure 6.4a). Qualitatively we observe noticeable fragmentation when ν_f is decreased below 1.3 MHz. For $\nu_f < 0.9$ MHz, the density distribution is truncated by the rf field and the atomic density decreases to zero in several areas. Reducing ν_f further results in well separated clumps of atoms which are found in only the lowest potential wells. The locations of trapped atoms then represent positions of potential minima, and furthermore the value of ν_f for which the local atomic density reduces to zero is easily related to the local magnetic field strength through the resonant condition given by Equation (6.1).

6.2.2 Data analysis

For quantitative analysis of the data we assume the full three-dimensional potential can be separated into two parts, consisting of the radial confining potential and the corrugated longitudinal potential (Section 2.2)

$$U(r, z) = \frac{1}{2} m \omega_r^2 r^2 + m_F g_F \mu_B |B_0 + B(z)|, \tag{6.2}$$

where m is the mass of ^{87}Rb, ω_r is the radial trap frequency and the coordinate $r = \sqrt{x^2 + y^2}$. This assumption is valid as the amplitude of the corrugated magnetic field component is small compared to the absolute offset field B_0. The atomic distribution in the trap immediately after the rf sweep is described by a truncated thermal Boltzmann distribution [85, 89] given by

$$n(r,z) = \frac{n_0}{(2\pi m k_B T)^{3/2}} \int_0^{E_{max}} \exp\left(-\left[\frac{\boldsymbol{p}^2}{2m} + U(r,z)\right]/k_B T\right) d\boldsymbol{p}, \tag{6.3}$$

where n_0 is the peak atomic density and $E_{max} = m_F h\nu_f - U(r,z)$ is the trap depth fixed by the frequency of the rf field. Integrating Equation (6.3) over r and introducing a spatially dependent truncation parameter $\beta = m_F(h\nu_f - g_F\mu_B|B(z)+B_0|)/k_B T$ gives

$$n(z) = n_\infty(z)\left(\mathrm{erf}(\sqrt{\beta}) - 2\sqrt{\beta/\pi}\mathrm{e}^{-\beta}(1 + 2\beta/3)\right), \tag{6.4}$$

where $n_\infty(z)$ is the integrated atomic density before truncation.

The magnetic potential landscape can simply be found by fitting Equation (6.4) in one dimension for each position z. We find however a systematic deviation from the truncated Boltzmann distribution for some of the data when the in-trap density becomes large (for example, at the bottom of the potential wells). In one dimension this effect becomes problematic and the fit fails to accurately reconstruct the shape of the potential wells. Instead, to extract the magnetic potential from the experimental data we first divide $n(z, \nu_f)$ spatially into 64 windows, each with a width of 16 pixels (80 μm). Each window is then fit in two-dimensions to the truncated Boltzmann distribution given by Equation (6.4) using a large scale least-squares minimisation routine. Each window consists of 640 data points (40×16) and the fit is allowed 33 free parameters: a single truncation temperature T, 16 values for $n_\infty(z)$ and 16 values for $B_z(z)$. The fitting procedure is performed for each window and concatenated to obtain the full B_z profile. Because T is allowed to vary discontinuously we find the reconstructed magnetic field profile often contains artificial discontinuities at the boundaries between adjacent windows. To avoid this problem we repeat the entire fitting procedure for several values

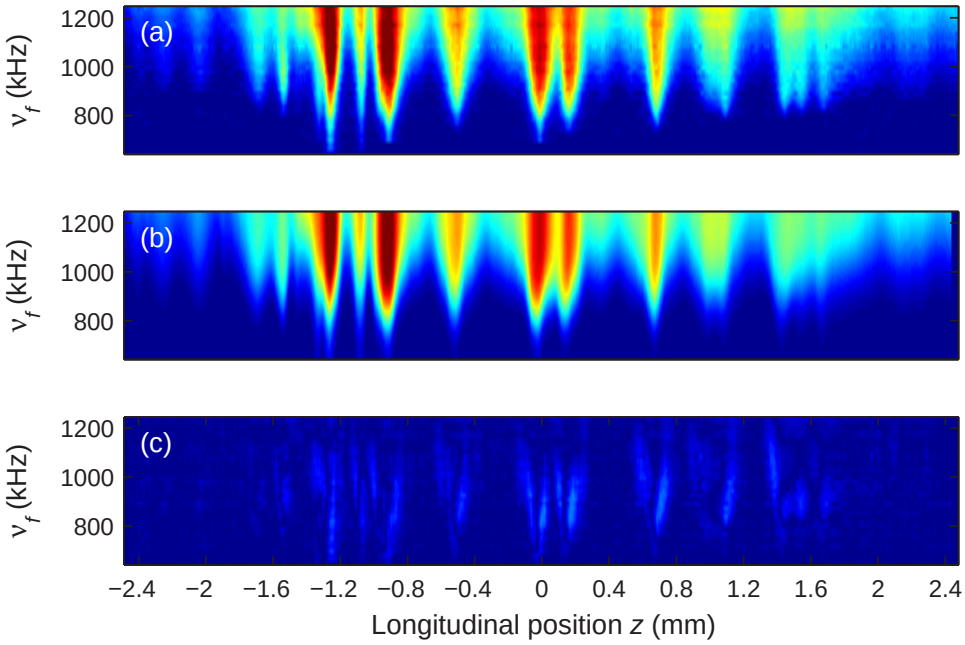

Fig. 6.4: (Colour) (a) The two-dimensional pseudo-colour density plot of number density is obtained using spatially resolved rf spectroscopy for $y = 67$ μm and is fit (b) to the truncated Boltzmann distribution. The fit residual (c) indicates some deviation from the truncated Boltzmann distribution in each of the potential wells most likely caused by high atomic density.

of the window offset (varied between 1 and 16 pixels) and average the results. This method basically constrains T to vary smoothly over a length scale comparable to the extent of a typical potential well (~ 80 μm) but takes advantage of the two-dimensional nature of the data set.

Typical fit results and fit residuals are shown in Figures 6.4b,c while the fit parameters are presented in Figure 6.5. After reconstructing the magnetic field profile the magnetic field offset B_0 and the effect of the end-wires is subtracted. The statistical uncertainty in the measurement is very low and mainly attributed to fluctuations of external magnetic fields (approximately 0.1 μT). With appropriate magnetic shielding, the expected sensitivity of the technique is limited by the power broadened rf linewidth required to effectively outcouple the atoms, which at low temperatures can be the order of 10 Hz ($\sim$0.7 nT). Longitudinal magnetic field profiles are given for several distances

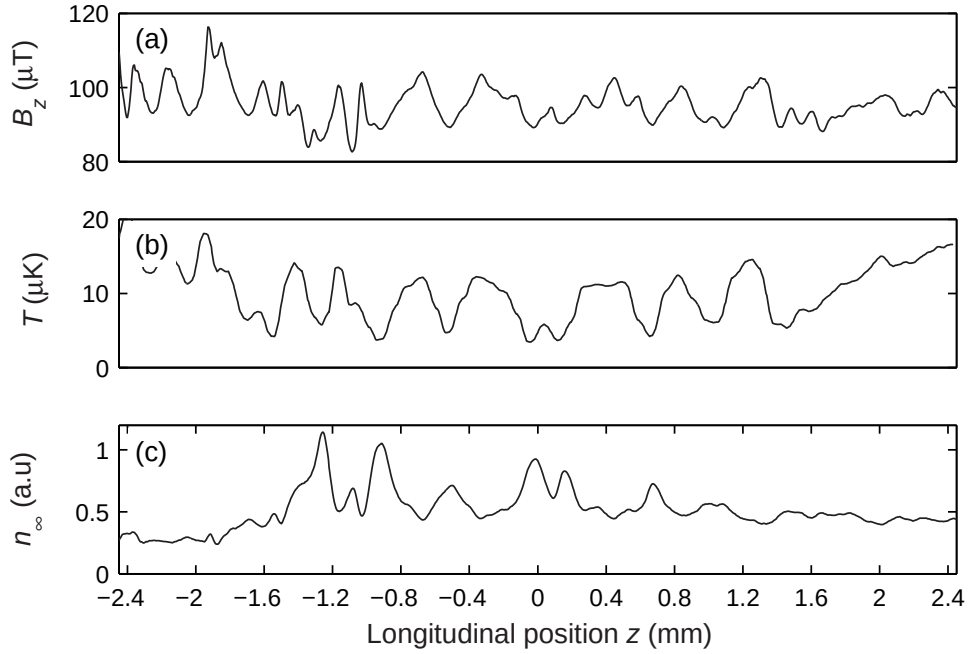

Fig. 6.5: Fit parameters for the data set of Figure 6.4. In (a) the extracted $B_z(z)$ profile is shown, while (b) and (c) correspond to the fitted truncation temperature T and the initial line density, $n_\infty(z)$, respectively.

from the film in Figure 6.6. The amplitude and the structure of the corrugations are constant from day to day; however the amplitude increases as the trap is positioned closer to the surface. The *rms* amplitude of the corrugation approximately follows a power law dependence given by y^{-a}, where $a = 1.8 \pm 0.3$. For $y > 100$ μm the potential has a characteristic period of about 390 μm, significantly longer than commonly observed near electroplated wires. Closer to the film, additional corrugations appear with a characteristic period of about 170 μm.

In order to determine the origin of the corrugations a second bias field is applied in the y direction to bring the trap closer to the surface while keeping a fixed distance from the edge of the magnetic film. Two imaging beams and CCD cameras are used to simultaneously record the longitudinal density distribution and the transverse position of the cloud. A cloud of atoms positioned 50 μm from the surface of the magnetic film and 100 μm from the edge is significantly fragmented (Figure 6.7a),

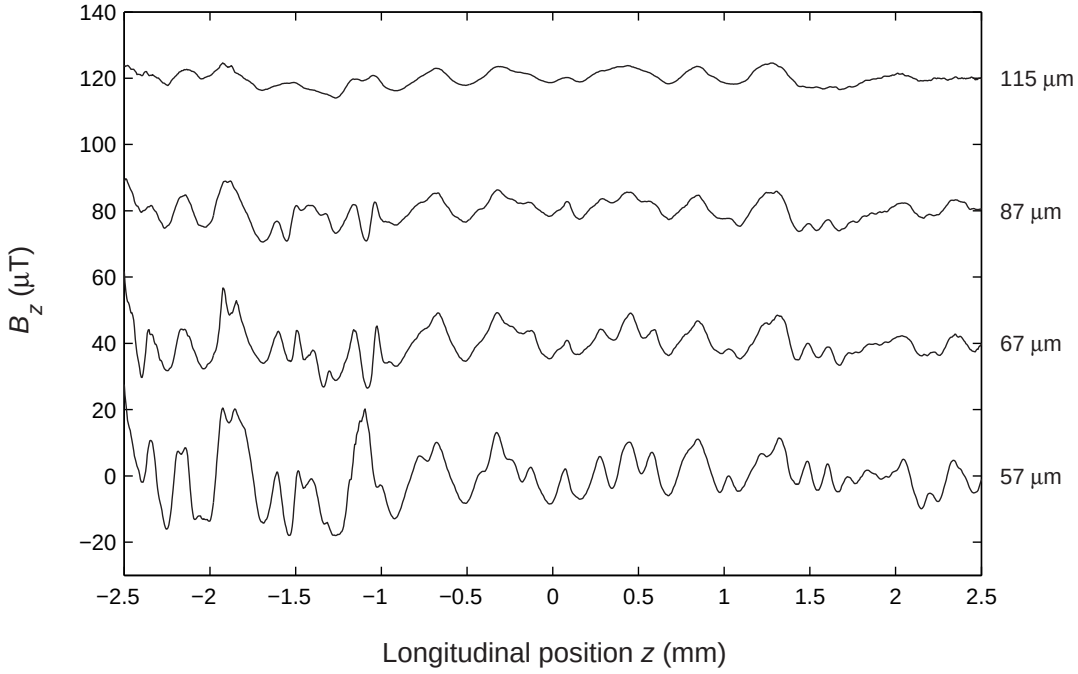

Fig. 6.6: Magnetic field profiles measured using spatially resolved radio frequency spectroscopy for $y = 115$ μm, 87 μm, 67 μm and 57 μm from the film surface. The offset magnetic field ($\sim$100 μT) and the effect of weak longitudinal confinement has been subtracted. Each profile is shifted by 40 μT for presentation.

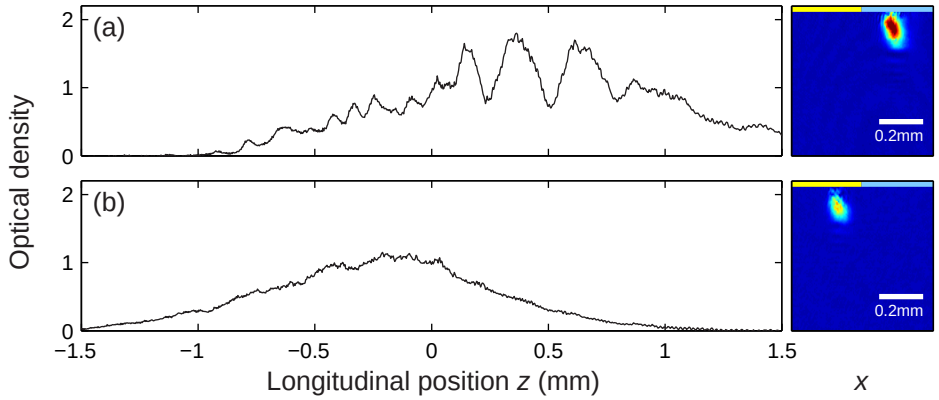

Fig. 6.7: (Colour) Absorption profiles of trapped thermal clouds of atoms positions (a) over the body of the magnetic film and (b) over the non-magnetic gold surface. The figures to the right show the transverse position of the cloud with respect to the magnetic film edge.

while a cloud positioned 50 μm above the non-magnetic gold film exhibits significantly reduced atomic density variations (Figure 6.7b). This observation confirms that the magnetic field variations originate from the bulk magnetic material itself as opposed to imperfections along the edge of the film.

6.3 Model of random magnetisation

We have developed a model to describe the effect of two-dimensional spatial variations in the magnetisation of the film. Inhomogeneity in the magnetisation leads to the appearance of a random magnetic field near the surface. We are most interested in the B_z component of the random magnetic field oriented parallel to the long axis of the trap which corrugates the bottom of the potential. The other two components have a negligible effect on cloud fragmentation as they are cancelled by the applied bias field B_{bias} and simply shift the position of the minimum slightly. The field produced by the magnetic film is found by evaluating the magnetic scalar potential [54]

$$\Phi(x,y,z) = -\frac{\mu_0}{4\pi}\int_V d^3r' \frac{\nabla' \cdot \boldsymbol{M}(\boldsymbol{r}')}{|\boldsymbol{r}-\boldsymbol{r}'|} + \frac{\mu_0}{4\pi}\oint_S \frac{\boldsymbol{M}(\boldsymbol{r}')}{|\boldsymbol{r}-\boldsymbol{r}'|} da' \tag{6.5}$$

for a magnetic film lying in the $x-z$ plane and with an edge at $x=0$. The magnetisation is assumed to be directed perpendicular to the film plane ($\boldsymbol{M} = \{0, M_y, 0\}$) and does not vary throughout the film thickness ($\partial \boldsymbol{M}/\partial y = 0$). The magnetic scalar potential given by Equation (6.5) therefore reduces to a surface integral that simply involves the difference between the top and bottom surfaces of the film. Consider a thin magnetic film with magnetisation expressed as a two-dimensional Fourier transform

$$M_y(x',z') = \iint_{-\infty}^{+\infty} N(k_x,k_z) \mathrm{e}^{i2\pi(k_x x' + k_z z')} dk_x dk_z. \tag{6.6}$$

The magnetic scalar potential is written as

$$\Phi(x,y,z) = \frac{\mu_0}{4\pi}\int_0^{+\infty}dx'\int_{-\infty}^{+\infty}dz'\iint_{-\infty}^{+\infty}dk_x dk_z \frac{N(k_x,k_z)\ \mathrm{e}^{i2\pi(k_x x'+k_z z')}}{\sqrt{(x-x')^2+(y-y')^2+(z-z')^2}}\Bigg|_{y'=-\delta}^{y'=0}$$
$$= \mu_0 \iint_{-\infty}^{+\infty} dk_x dk_z N(k_x,k_z)\ \mathrm{e}^{i2\pi(k_x x+k_z z)} I(k_z,x,y), \tag{6.7}$$

where $F(x)\big|_{x=b}^{x=a} = F(a) - F(b)$, δ is the film thickness, and $I(k_z,x,y)$ is given by

$$I(k_z,x,y) = \int_{-x}^{+\infty} dx'' \mathrm{e}^{i2\pi k_x x''} K_0\left(2\pi k_z\sqrt{x''^2+(y-y')^2}\right)\Bigg|_{y'=-\delta}^{y'=0}, \tag{6.8}$$

where $x'' = (x'-x)$, and K_n is the modified Bessel function of the second kind of order n. The z-component of the magnetic field is then easily evaluated as

$$B_z = -\frac{\partial\Phi}{\partial z} = \iint_{-\infty}^{+\infty} dk_x dk_z N(k_x,k_z)\ \mathrm{e}^{i2\pi(k_x x+k_z z)} g_z(k_x,k_z), \tag{6.9}$$

where the field transfer function of the half plane magnetic film is denoted by $g_z(k_x,k_z) = -i\mu_0 k_z I(k_z,x,y)$.

The field transfer function provides the ratio between the Fourier components of the magnetic field and the film magnetisation and acts like a low pass filter, reducing the effect of high frequency magnetisation components. For a thin magnetic film ($\delta << y$) the Bessel function in Equation (6.8) can be expanded as a Taylor series (where $dK_0(x)/dx = -K_1(x)$) to give

$$g_z(k_x,k_z) = -i\delta 2\pi\mu_0 k_z^2 y \int_{-x}^{\infty} dx'' \mathrm{e}^{i2\pi k_x x''} \frac{K_1\left(2\pi k_z\sqrt{x''^2-y^2}\right)}{\sqrt{x''^2-y^2}}. \tag{6.10}$$

In the case of white noise variations of the film magnetization, $N(k_x,k_z)$=$N_0\ \mathrm{e}^{i\Theta_n(k_x,k_z)}$. The random phase factor Θ_n is dealt with by calculating the ensemble average of the field squared, $\langle B_z^* B_z\rangle_n$. The ensemble average only affects the

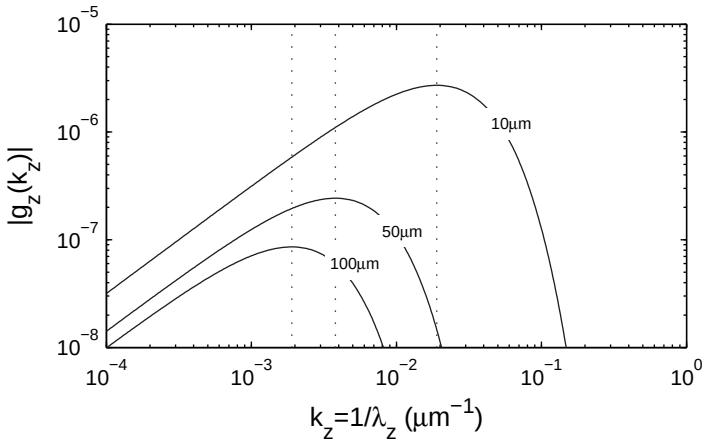

Fig. 6.8: The field transfer function, $g_z(k_z)$, for $x = 0$ plotted as a function of the wave-vector k_z for distances of 100 μm, 50 μm and 10 μm from the surface. In all cases the film thickness is $\delta = 0.9$ μm. The field transfer function reaches a maximum value for $k_z = 0.19/y$ and decays exponentially for both short and long wavevectors.

random phase factor such that $\langle \mathrm{e}^{i\Theta_n(k)}\mathrm{e}^{-i\Theta_n(k')}\rangle_n = \delta(k-k')(1/L^2)$. For the edge of the film $x = 0$ it is possible to integrate over k_x and obtain an analytic expression for the field transfer function squared

$$|g_z(k_z)|^2 = \pi^2\mu_0^2\delta^2 k_z^3 K_1(4\pi k_z y). \tag{6.11}$$

In Figure 6.8 the field transfer function is plotted for distances of $y = 100$ μm, 50 μm and 10 μm from the film surface. This indicates that components of the corrugated potential dominate the field noise for $k_z = 0.19/y$ such that the principle corrugation length scale decreases with decreasing distance to the surface.

In general it is possible to obtain a result for the x-dependent magnetic field roughness squared which is given by

$$\begin{aligned}\langle B_z^* B_z\rangle_n &= (N_0/L)^2 \iint_{-\infty}^{+\infty} dk_x dk_z |g_z(k_x,k_z)|^2 \\ &= \frac{3}{\pi}\left(\frac{\mu_0\delta\Delta M}{16y^2}\right)^2\left[1+\frac{15}{8}\alpha-\frac{5}{4}\alpha^3+\frac{3}{8}\alpha^5\right],\end{aligned} \tag{6.12}$$

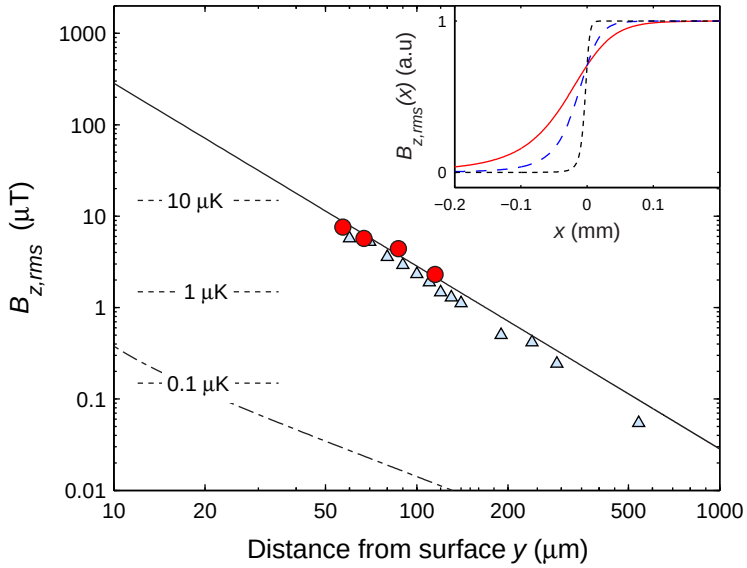

Fig. 6.9: (Colour) Dependence of the magnetic field roughness $B_{z,rms}$ on distance from the film surface. The dashed line corresponds to a homogeneous film with a fluctuating edge as measured by a profilometer. The solid line is a fit to the experimental data using Equation (6.12) which corresponds to white noise magnetisation variations within the body of the film. The triangles indicate the results of an independent measurement using a scanning magneto-resistive microscope. The inset shows the x dependence of the magnetic field noise for 100 μm (solid line), 50 μm (dashed line) and 10 μm (dotted line) from the surface.

where $\alpha = x/\sqrt{x^2+y^2}$ and $\Delta M = \sqrt{\left\langle \left(M_y - \langle M_y \rangle\right)^2 \right\rangle}$ is the rms magnetisation inhomogeneity.

The model predicts that at the edge of the film ($x = 0$) the corrugated magnetic field component decays with a y^{-2} dependence which is consistent with the experimental result of $y^{-1.8\pm0.3}$. This can be compared with the rapid decay expected for white noise fluctuations of the edge of a current-carrying wire which scales as $y^{-2.5}$ [18]. The model also predicts the additional decay of the corrugated magnetic field component away from the edge for $x < 0$ through the dependence on α. In Figure 6.9, experimental measurements of the magnetic field from the previous section are compared with the model, with relevant energy scales for ^{87}Rb atoms in the $|F = 2, m_F = +2\rangle$ state indicated with dotted lines. Edge fluctuations of a similarly prepared substrate were measured previously using a scanning stylus profilometer (Section 3.2.1). This is

expected to produce a field corrugation with an amplitude three orders of magnitude smaller than the observations.

The characteristic feature size and distribution of the magnetic inhomogeneity has been approximated by MFM measurements of a previously demagnetised magnetic film (Section 3.3.2). We find the typical domain structure has close to white noise characteristics with a feature size of $d = 5$ μm. A fit of Equation (6.12) to the experimental data indicates $\Delta M \simeq 0.3 M_s$ where M_s is the saturation magnetisation of the film. If the inhomogeneity is assumed to originate from the reversal of a small number of magnetic domains ($M_y(x', z') = \pm M_s$) at uncorrelated positions then the mean magnetisation of the film M_r can be simply related to the magnetic inhomogeneity ΔM by noting that $\langle M_y \rangle = M_r$ and $\langle M_y^2 \rangle = M_s^2$ to find $M_r/M_s = \sqrt{1 - \Delta M^2/M_s^2}$. By assuming domain reversal is the main cause of the observed inhomogeneity we can conclude that the mean magnetisation of the film is $M_r \approx 0.95 M_s$.

6.4 Scanning magneto-resistive microscopy

To further study the properties of the magnetic film and determine the cause of the observed magnetic inhomogeneity the atom chip was removed from the vacuum chamber. Subsequent analysis is performed using an ultra-sensitive low-field magnetic sensor based on magnetic tunneling junction technology [90]. These devices are developed predominately for modern hard-disk read heads which are available with active areas as small as $\sim$100$\times$100 nm^2 and with magnetic field sensitivities in the nT range. A magnetic tunneling junction sensor consists of two ferromagnetic layers separated by an ultra-thin insulating interlayer. One magnetic layer has fixed magnetisation while the other responds to the local magnetic field. The interlayer resistance depends on the relative magnetisation of the neighbouring magnetic layers and is typically maximum for antiparallel alignment. These devices provide an absolute measure of the magnetic field with high sensitivity and high spatial resolution and are ideal for studying the magnetic fields produced by microfabricated current-carrying wires or patterned magnetic materials on atom chips. Here the sensor is incorporated

into a home-built scanning magnetic field microscope and used to study the corrugated field produced by the magnetic film atom chip.

Our scanning magneto-resistive microscope incorporates a magnetic tunnel junction probe (MicroMagnetics STJ-020), polished to allow very close approaches to the surface ($\sim$5 μm). The active area of the sensor is approximately 5×5 μm^2 and it detects the magnetic field oriented along the sensor tip (vertical direction). The sensor is interfaced using an Anderson loop [91] as an alternative to the Wheatstone bridge, to convert small changes in the sensor resistance to a signal voltage. The output is then amplified using a signal amplification board (MicroMagnetics AL-05) with a gain of 2500 and a bandwidth of 1 MHz. The quoted noise levels at low frequencies are $1 - 5$ nT/$\sqrt{\text{Hz}}$ and above 200 Hz are $0.5 - 2$ nT/$\sqrt{\text{Hz}}$.

The probe is mounted above a computer controlled linear translation stage for positioning the sample along z. Translation along x and the height of the probe above the sample y is adjusted using two manual micrometer stages. A camera is oriented parallel to the sample in order to position the probe with respect to the edge of the film and to determine the probe-surface distance. The height of the sensor is determined by landing the probe on the sample surface and recording the $y = 0$ micrometer value. The amplifier output is calibrated against a commercial Hall probe sensor in a uniform field and gives a value of 20 V/mT. To measure a magnetic field profile, the z position is scanned at a rate of 0.1 mm/s, low-pass filtered and averaged over 30 passes using a digital oscilloscope. The output field noise level in the absence of the atom chip is approximately 0.5 μT.

To further improve the signal to noise ratio we use ac modulation and a lock-in amplifier. The tip of the probe is oscillated along z at the mechanical resonance frequency of 18 kHz using a piezo actuator. At this frequency the $1/f$ noise level of the sensor is significantly reduced; however the output of the lock-in amplifier is then proportional to the first derivative of the magnetic field. We calibrate the output using a known magnetic field gradient which indicates the oscillation amplitude is 50 μm. Using this technique the noise level is 5 times lower (0.1 μT) than for the dc method

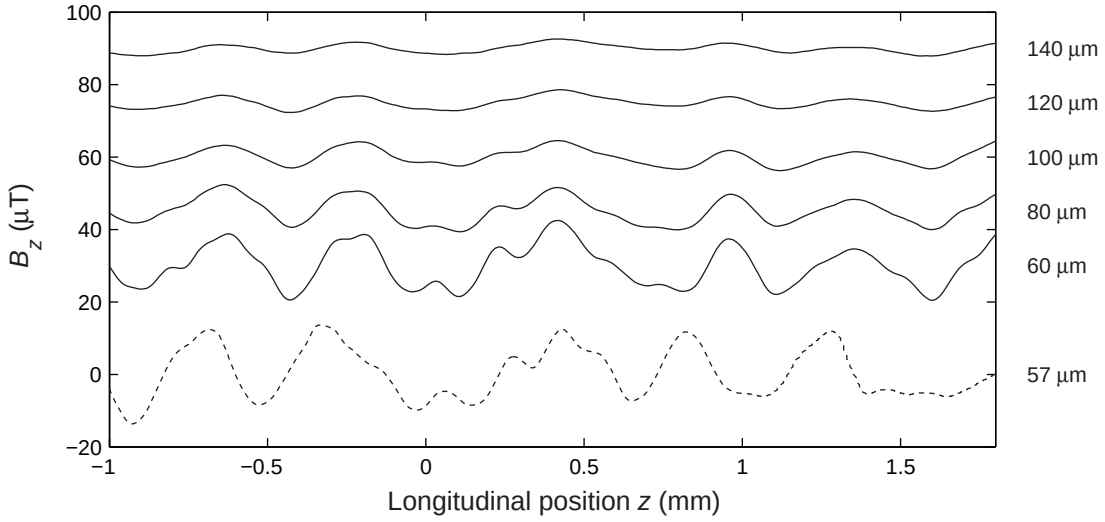

Fig. 6.10: Measurements of the magnetic field corrugation B_z vs distance from the film surface measured using a magnetic tunneling junction (MTJ) sensor. Shown are scans performed 60 μm, 80 μm, 100 μm, 120 μm and 140 μm from the surface (solid lines). Each profile is shifted by 15 μT for presentation. Also shown is a measurement performed using spatially resolved rf spectroscopy of the ultracold atoms (dotted line). The relative longitudinal offset between the two measurements is initially unknown and is adjusted for optimum agreement.

with an equivalent measurement time. We expect even better results using the lock-in method for current-carrying wires as the magnetic field itself can be modulated at kHz frequencies.

A series of magnetic field scans of the magnetic film are shown in Figure 6.10, which have been recorded by Dr. Michael Volk following the removal of the atom chip from the vacuum chamber. The scans of the magnetic field were performed along z over a region of 3.5 mm for heights y ranging from 500 μm down to 60 μm, the minimum distance limited by the adjacent protruding gold coated glass slide. Due to the large magnetic field produced at the film edge it was necessary to carefully align the measurement direction and substract a third order polynomial from the data. The same basic behaviour (i.e., the y dependence of the amplitude and characteristic period) of the corrugated magnetic field can be seen in both the magneto-resistive measurements (Figure 6.10) and the previous results from rf spectroscopy of ultracold

atoms (Figure 6.6). Also shown in Figure 6.10 are two profiles measured at $y \approx 60$ μm using both methods indicating a remarkable agreement between rf spectroscopy of ultracold atoms and the magneto-resistive sensor. It should be noted however that a quantitative comparison is difficult as the two methods are sensitive to different components of the corrugated magnetic field: the magneto-resistive sensing direction is perpendicular to the surface while the trap bottom is defined by the in-plane component of the magnetic field. The results of the magneto-resistance study are also included in Figure 6.9 and support the random magnetisation model and the y^{-2} decay of the corrugated magnetic field amplitude.

Measurements on similar films using the magneto-optical Kerr effect and magneto-resistance microscopy have indicated that elevated temperatures during vacuum bake-out have an influence on the magnetic properties of the GdTbFeCo films. A general finding is that for baking temperatures above 100 °C the remanence ratio begins to decrease and the magnetic field at the surface becomes significantly corrugated. We have also found this effect is especially high near the edge of the film. For baking temperatures ≤ 100 °C the magnetic properties appear to be stable, sustaining periods of elevated temperature for several days without effect. This may be correlated with the optimum deposition temperature (100 °C) or with reports of reduced perpendicular anisotropy found for similar films after annealing at temperatures above 100 °C [92,93]. Since these findings, the magnetic film atom chip has been re-magnetised and returned to the apparatus for future experimental studies. After remagnetisation the residual magnetic inhomogeneity was reduced by a factor of 10.

Chapter 7

Bose-Einstein condensates in a double-well potential

7.1 Introduction

This chapter deals with experiments involving Bose-Einstein condensates in a double-well (dw) potential. The dw is identified at the central region of the corrugated magnetic potential studied in the previous chapter (Figure 6.6). The shape of the dw, including the barrier height and well separation depends on the distance from the film surface. A single BEC can be produced far from the film surface and then dynamically split by moving the trap closer to the surface. After splitting we find the population of atoms in each well is extremely sensitive to the symmetry of the dw potential. This property of the BEC is used to realise a precision gradiometer, which measures small magnetic field gradients and can be applied to sense tiny gravitational forces on a small scale [94]. We carefully control the symmetry through current in the end-wires and calibrate the applied magnetic field gradient using rf spectroscopy of separated Bose-Einstein condensates. The fractional atom number difference is measured as a function of the applied asymmetry and the sensor is found to have a single-shot sensitivity to magnetic field gradients of 17 pT/μm or changes in gravitational forces of $\delta g/g = 1.1 \times 10^{-4}$ over a 70 μm spatial area. The experimental results and the ultimate sensitivity can be predicted by a simple model assuming a Thomas-Fermi

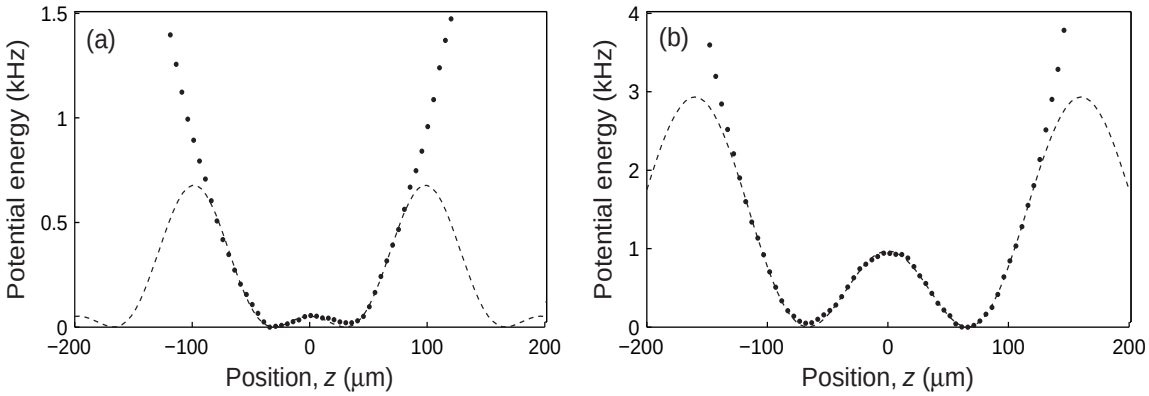

Fig. 7.1: Reconstructed double well potential (dots) for distances (a) 180 μm (b) 130 μm from the film surface. Fits to the model potential of Equation (7.2) are also shown (dashed line) indicating for (a) $bh = 20$ Hz, $ws = 60$ μm and $\beta = 0.63$ and (b) $bh = 1$ kHz, $ws = 130$ μm and $\beta = 0.27$. The fitted model does not include the effect of the end wires which provide additional confinement for large $|z|$.

density distribution for the split condensate. The results in this chapter have also been published in Physical Review Letters (2007) [95].

7.2 The double-well potential

In the previous chapter it was shown how inhomogeneity of the permanent magnetic film after bake-out leads to a corrugated magnetic potential, causing fragmentation of ultracold clouds of atoms. The *rms* amplitude of the corrugation increases as the atoms are brought closer to the surface and the short wavelength components of the potential become more pronounced. In this chapter it is shown how a single Bose-Einstein condensate can be split in the corrugated potential and how the resulting density distribution is extremely sensitive to minute magnetic field gradients and gravitational forces. We focus in particular on the central region of the corrugation which resembles a double-well potential. The exact shape of the double-well potential has only a minor influence over the splitting dynamics and the final density distribution. A simplistic but surprisingly accurate approximation to the double-well region in this experiment involves the combination of two periodic components with amplitudes which decay

from the surface at differing rates [96]:

$$V_{dw}(z) = a_1\cos(2\pi z/\lambda_1) - a_2\cos(2\pi z/\lambda_2) + \mathit{offset}, \tag{7.1}$$

where the field amplitudes a_1 and a_2 are dependent on the distance from the surface y and the wavevectors $2\pi/\lambda_{1,2}$. For simplicity we consider $\lambda_2 = 2\lambda_1$ and rewrite the dw potential in the convenient form

$$V_{dw}(z) = 2a_1\big(\beta - \cos(\pi z/\lambda_1)\big)^2, \tag{7.2}$$

where $\beta = |a_2/4a_1|$ is a distance-dependent splitting parameter which determines the overall shape of the potential which can controlled in a time-dependent way. For large distances from the surface $\beta \geq 1$, and the potential involves a single well. At the coalescence point $\beta = 1$ the single-well potential is approximately quartic in shape. For $\beta < 1$ two approximately harmonic wells appear and it is possible to define the barrier height bh and the double-well separation ws as useful characteristics:

$$bh = 2a_1(\beta - 1)^2 \qquad ws = \frac{2\lambda_1}{\pi}\arccos(\beta). \tag{7.3}$$

The position of the trap and therefore also the parameter β is controlled by varying the applied field B_{bias}. By increasing B_{bias} it is possible to smoothly transform the potential from a single well to a double well to split the BEC in two parts.

Since the magnetic field topology originates from random magnetisation variations we cannot pre-determine the exact shape of the dw potential. Instead we first perform a systematic characterisation of the dw region using ultracold atoms. Spatially resolved rf spectroscopy alone is not suitable for this purpose as some features of the magnetic potential (such as the potential barrier) can be significantly smaller than the 0.1 μT background ac magnetic field variations in the laboratory. Instead we use the equilibrium distribution of atoms confined in the dw region, a technique which is insensitive to fluctuations of the absolute magnetic field strength.

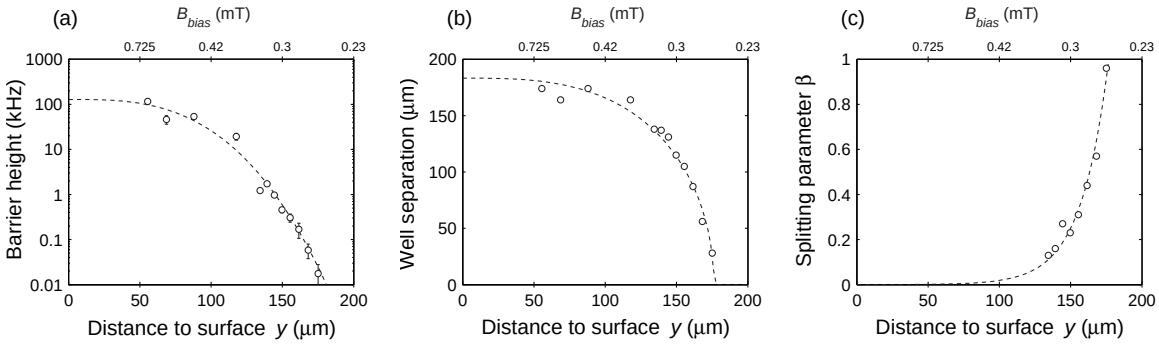

Fig. 7.2: Characterisation of the double well as a function of trap-surface separation. The barrier height (a), the well separation (b) and the splitting parameter β (c) are shown. Figures (a) and (b) also include four data points extracted from the less precise but absolute spatially resolved rf spectroscopy data of chapter 6.

To determine the overall shape of the dw potential we prepare an ultracold thermal atom cloud approximately 175 μm from the film surface. We then slowly ramp B_{bias} over 500 ms to move the cloud to the desired position. After a short time to ensure thermal equilibrium we take an in-trap absorption image. The cloud temperature is also determined through a sequence of ballistic expansion images. The approximate form of the dw potential including the barrier height and well separation can then be inferred from a comparison with the Boltzmann distribution function $V(z) = -k_B T \ln(n(z)) + const.$ The experimental data for two distances from the film surface showing the shape of the dw potential are shown in Figure 7.1. Throughout this chapter the units of energy (μ/h,V/h) are indicated in kHz.

We fit Equation (7.2) to the measured potential around the minimum of the dw for a range of distances and extract the parameters of the potential such as the barrier height bh, the well separation ws and the splitting parameter β. This is repeated for a number of distances from the surface as shown in Figure 7.2. The coalescence point ($\beta = 1$) occurs 175 μm from the surface for a value of B_{bias} =0.261 mT. The radial trap frequency at this position is $\omega_r = 2\pi \times 177$ Hz. Increasing B_{bias} further moves the trap closer to the surface and splits the trap longitudinally. The characterisation shows that the barrier height can be increased from 0 to > 100 kHz, the well separation ranges from

0 to 170 μm and the splitting parameter β decreases from 1 to ~ 0 (Figure 7.2). The dw potential used in the following experiments is found for $B_{bias} = 0.271$ mT which corresponds to a distance of 170 μm, a radial trap frequency of $\omega_r = 2\pi \times 160$ Hz, a barrier height of $bh = 130$ Hz, a well separation of $ws = 70$ μm and a splitting parameter $\beta \approx 0.5$.

Another parameter of interest is the potential energy gradient ΔV which introduces an asymmetric component of the potential denoted $\Delta V z$ which is assumed to vary linearly with z over the range of interest. This additional component introduces a difference in potential energy across the two wells equal to $ws\Delta V$ and causes a marked lop-sidedness in the density distribution. The symmetry of the dw potential is ultimately determined by the symmetry of the corrugated magnetic potential as well as any external magnetic field gradients or gravitational tilt of the apparatus. These asymmetries can however be compensated for or adjusted by introducing a small current imbalance δI to the end-wires on the atom chip. The magnetic field gradient produced at the midpoint between the end-wires (approximately the position of the dw) separated by a distance d is proportional to δI and is given by

$$\left.\frac{\delta B_z}{\delta z}\right|_{z=d/2} = \frac{8\ \mu_0\ \delta I d\ y}{\pi(d^2+4y^2)^2}. \tag{7.4}$$

For our experimental parameters $d = 9$ mm and accounting for the location of the wires with respect to the chip surface $y \sim 0.7$ mm, which gives an approximate scaling of 2.9 pT μm^{-1}mA^{-1} which for ^{87}Rb atoms in $m_F = +2$ is equivalent to $\Delta V/h \approx 41$ mHz μm^{-1} per milliampere.

To account for any finite length effects or imperfections in the machined wires we also calibrate $\Delta V/h$ as a function of δI directly through rf spectroscopy of Bose-Einstein condensates. This is performed by first preparing two BECs separated by $ws = 170$ μm in the dw potential at a distance of 90 μm. At this position the barrier height is significantly larger than the chemical potential of either condensate. We then ramp on a relatively large current imbalance of 1 A to the end wires over a duration of 500 ms. The distribution of atoms in the dw does not significantly change. A

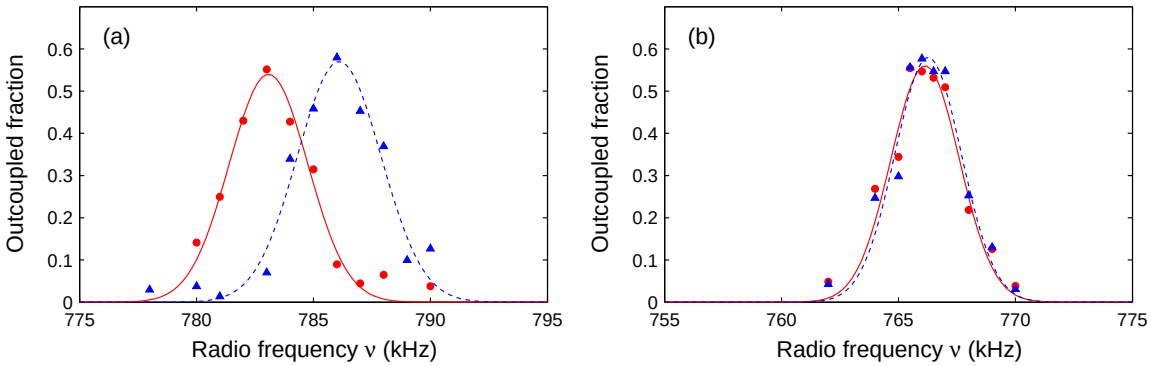

Fig. 7.3: (Colour) Pulsed rf spectra of two condensates in the dw potential for two asymmetries. In (a) a 1 A current imbalance is applied to the end-wires such that the left well (red circles) has a lower magnetic potential energy than the right well (blue triangles). The asymmetry is determined by fitting peak functions (dotted lines) to the spectra where $ws\Delta V/h = m_F(\nu_R - \nu_L) = 6$ kHz. This is then compared to the case with no field gradient (b) to calibrate the effect of the end wires.

fixed frequency rf pulse is then applied for 1 ms to resonantly outcouple atoms from either well depending on the local magnetic potential energy $\nu = g_F\mu_B B/h$. After the pulse the remaining number of atoms in each well is determined through an absorption image. The process is repeated for many values of the rf to build up a spectrum of the two condensates (Figure 7.3a). The whole procedure is repeated without the current imbalance (Figure 7.3b) to determine the magnetic field gradient as a function of δI. These results are shown in Figure 7.3. From the spectra we infer a value for $\Delta V/h$ of 32 mHz μm^{-1} per milliampere in reasonable agreement with the expectation.

7.3 Splitting Bose-Einstein condensates

Focus is now placed on the time-dependent splitting of a Bose-Einstein condensate in the asymmetric double well. With the effect of the end wires calibrated using rf spectroscopy it is possible to examine the sensitivity of the splitting process to small controlled values of ΔV. It is expected that the imbalance in well populations increases with the relevant energy scale $\Delta V/\mu$, where μ is the chemical potential of the condensate. The sensitivity also depends on the splitting time t_s and is maximum for

large t_s.

A small condensate consisting of 4×10^4 atoms is produced in the single-well potential near the coalescence point located 175 μm from the surface. The uniform field B_{bias} is then ramped from 0.261 mT to 0.271 mT over 2 s. At the new position 170 μm from the surface the barrier height is $bh = 130$ Hz, the well separation is $ws = 70$ μm and the splitting parameter is $\beta \approx 0.5$. The ratio of the chemical potential to the barrier height is $\mu/bh \simeq 4$. At this point the BEC is double-peaked and the lop-sided distribution of atoms depends on the symmetry of the dw potential. To provide better discrimination between the left and right wells at the end of the ramp it is possible to rapidly increase B_{bias} over 10 ms to further separate the BEC into two parts. This is too fast for the relative populations to change significantly and simply splits the BEC in two. In this way the potential barrier itself defines the left-right boundary rather than an arbitrary reference point on the CCD camera. The two BECs are then released from the trap for 2 ms before imaging to avoid saturation effects and to minimise the influence of any residual low-density thermal component. The absorption image is then integrated to determine the number of atoms in the left and right condensates and the population imbalance is evaluated:

$$\frac{\Delta N}{N} = \frac{N_L - N_R}{N_L + N_R}. \tag{7.5}$$

In Figure 7.4 the measured population imbalance is shown as a function of the dw asymmetry which is carefully controlled through the end-wire current imbalance ranging between $\delta I \pm 120$ mA. Each of the 35 individual measurements takes approximately 30 s and are collected randomly in time to minimise the effect of any systematic drift of the apparatus. A linear fit to the data indicates $\Delta N/N = 1.18 \times 10^{-3} ws \Delta V/h$ for $ws = 70$ μm. From the distribution of the data we determine the shot-to-shot noise level to be about 2.8% which gives a single-shot sensitivity to the potential energy difference between wells of 16.7 Hz, and 4.7 Hz over the 35 measurements. Taking into account the well separation this corresponds to a single-shot sensitivity to potential energy gradients of 240 mHz μm^{-1}. We note that the sensitivity

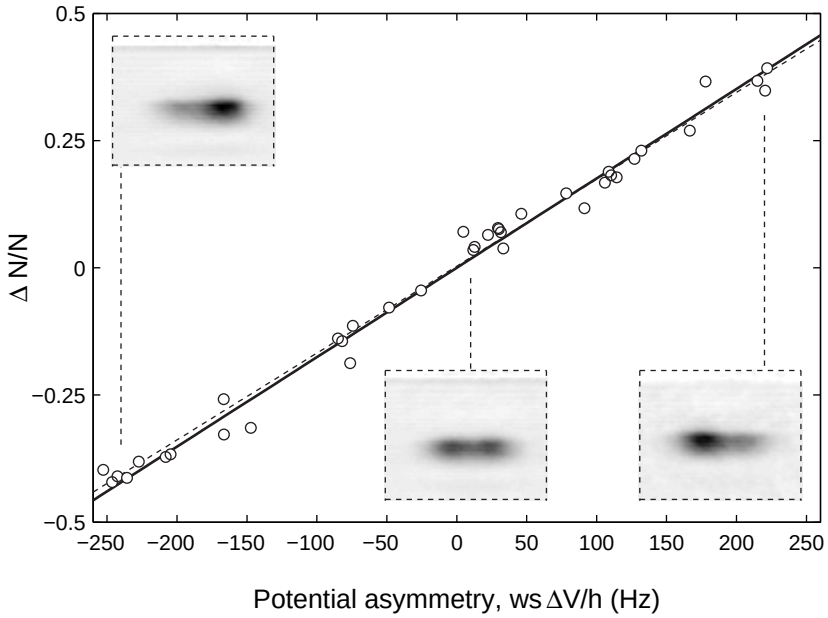

Fig. 7.4: Fractional atom number difference versus the double-well potential asymmetry. The asymmetry is controlled by varying the end wire current imbalance δI. The experimental data points (open circles) and the line of best fit (dashed line) compare well with the expectations based on the Thomas-Fermi model (solid line).

is significantly improved over that obtained using rf spectroscopy which is limited by fluctuating magnetic field variations at the $\sim$ 1 kHz level. Moreover, since $\Delta N/N$ depends on the total potential energy, the splitting is also sensitive to non-magnetic field contributions such as gravity. The expected single-shot sensitivity to changes in gravity for ^{87}Rb atoms is $\delta g/g = 1.1\times10^{-4}$ over a 70 μm region, which is equivalent to a mere 8 nm height difference across the two wells. At present this sensitivity to potential gradients surpasses reports of on-chip BEC interferometers which are currently limited by relatively short phase coherence times.

7.4 Steady state model

To provide further understanding of the experiment and to provide information about the possible limitations of this technique we developed a model. Assuming the splitting time is large compared to the inverse asymmetry $t_s \gg (ws\Delta V)^{-1}$, the Bose-Einstein

condensate remains in the lowest mode of the potential and the distribution of atoms in the dw should be equivalent to the ground state probability density [97]. For an interacting condensate with large N this is well approximated by the Thomas-Fermi distribution (Section 2.4):

$$n(r,z) = \frac{1}{g}(\mu - V(r,z)), \tag{7.6}$$

which is defined for $\mu > V(r,z)$ and is zero elsewhere. The chemical potential μ is determined from the normalisation condition $N = 2\pi \int n(r,z)\ rdrdz$. We first separate the full potential $V(r,z)$ in terms of the harmonic radial confinement and the dw potential with an asymmetric term (Section 2.2)

$$V(r,z) = \frac{1}{2}m\omega_r^2 r^2 + V_{dw}(z), \tag{7.7}$$

where $V_{dw}(z) = 2a_1\big(\beta - \cos(\pi z/\lambda_1)\big)^2 + \Delta V z$. This is then integrated over the radial dimension r to give the linear probability density, where the limits of integration are defined by $0 : r_{max}$

$$r_{max} = \sqrt{\frac{2(\mu - V_{dw}(z))}{m\omega_r^2}}. \tag{7.8}$$

The integrated Thomas Fermi (TF) distribution is then

$$n(z) = \frac{\pi}{gm\omega_r^2}\left(a_1\Big(1 + 2\beta^2 - 4\beta\cos(\pi z/\lambda_1) + \cos(2\pi z/\lambda_1)\Big) + \Delta V z - \mu\right)^2, \tag{7.9}$$

which is valid for $\mu > V_{dw}(z)$ and zero elsewhere. In the absence of an asymmetry ($\Delta V = 0$) the limits of the TF distribution are easily defined:

$$z_{max,0} = \frac{\lambda_1}{\pi}\arccos\big(1 - (\beta - 1)(k - 1)\big), \tag{7.10}$$

where the parameter $k = \sqrt{\frac{\mu}{bh}}$ accounts for the amplitude of the chemical potential above the dw barrier. To include the effect of the asymmetric term and define the

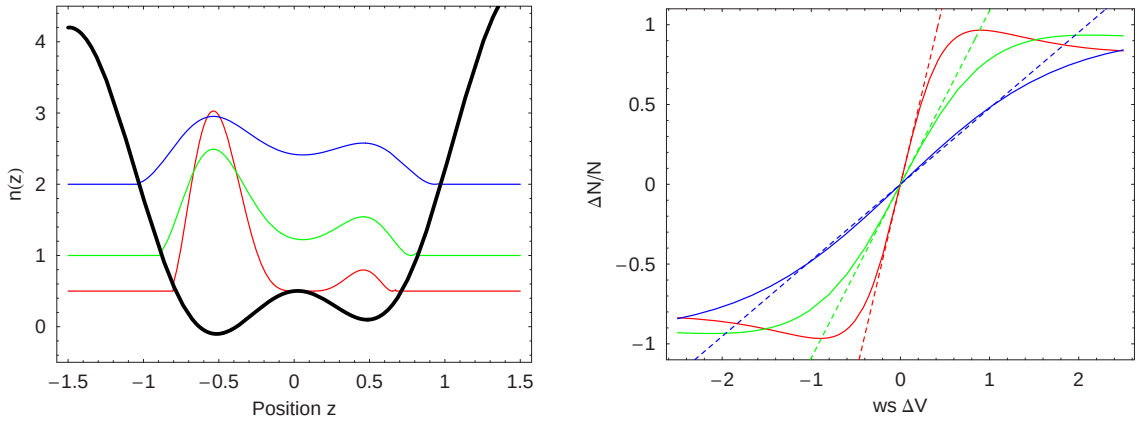

Fig. 7.5: (Colour) The asymmetric double well is modelled by the combination of two Fourier components (a). The three curves correspond to $\mu = 2$ (blue), $\mu = 1$ (green) and $\mu = 0.5$ (red). From this model we can determine the dependence of the fractional number difference $\Delta N/N$ on the asymmetry ΔV (b). The dotted lines correspond to the linear approximation for small $\Delta N/N$ given by Eq. (7.13).

general TF limits it is necessary to expand $n(z)$ to first order in z for $z \to z_{max,0}$. This expansion is equivalent to assuming the asymmetry is small compared to other relevant energy scales. The limits $z_{max,L}$ and $z_{max,R}$ including the effect of the asymmetry are then simply the zero crossing points for the linear approximation to $n(z \approx z_{max,0})$:

$$z_{max,L/R} = \frac{z_{max,0}}{2} \frac{k(\beta-1)\Delta V\lambda_1 \mp 4\pi\mu\sqrt{(\beta-1)(k-1)\Big(2-(\beta-1)(k-1)\Big)}}{k(\beta-1)\Delta V\lambda_1 \pm 4\pi\mu\sqrt{(\beta-1)(k-1)\Big(2-(\beta-1)(k-1)\Big)}}. \quad (7.11)$$

In Figure 7.5a, a series of TF distributions with different values of the chemical potential μ are calculated for a dw potential with $\beta = 0.5, bh = 0.5, ws = 1$. For μ large compared to the asymmetry ($\mu \gg \Delta V ws$) the distribution is mostly symmetric ($\Delta N/N \sim 0$); however for small μ the distribution becomes dramatically lop-sided. Once the TF limits are defined the probability density distribution can be further integrated to

determine the left and right well populations:

$$N_L = \int_{z_{max,L}}^{0} n(z)\, dz \qquad N_R = \int_{0}^{z_{max,R}} n(z)\, dz, \tag{7.12}$$

where the population imbalance $\frac{\Delta N}{N}$ is defined by Equation 7.5. The full analytic solution for $\frac{\Delta N}{N}$ is quite cumbersome; however for fixed β and after performing Taylor series expansions for $k \approx 1$ and small ΔV it is possible to write a solution in analytic form. For $\beta = 0.5$ (split case) the steady state model gives

$$\left.\frac{\Delta N}{N}\right|_{\beta=\frac{1}{2}} \approx 1.18\left(\frac{ws\Delta V}{\mu}\right)\Big(1 - 0.20(k-1)\Big). \tag{7.13}$$

The results of the model are shown in Figure 7.5b for varying μ. As is shown, the gradient of $\frac{\Delta N}{N}$ which determines the sensitivity of the population imbalance to the splitting is largest for small μ. The approximations for small ΔV and $k \approx 1$ are also shown with dotted lines.

From the analytic solution we see that the population imbalance is proportional to the well separation ws and to the ratio of the asymmetry to the chemical potential $\Delta V/\mu$. Additionally there is a particularly weak dependence on k which suggests that the barrier height (or more appropriately the ratio of the chemical potential to the barrier height) plays only a minor role in determining the overall sensitivity of the dw sensor. The parameter β plays a similarly minor role. This implies that the exact form of the dw potential has only a minor influence over the final result, and therefore the key conclusions from this section can also be applied to other forms of the dw potential. In our experiments the separation between the two wells ws is significantly larger that for recent double-well experiments by other groups using adiabatic rf potentials (typically 5-6 μm) [15, 98] and the effect of tunnelling between the two wells is significantly suppressed. High sensitivity to potential gradients is achieved due to the large well separation and the small chemical potential μ.

Chapter 8

Conclusion

8.1 Summary

This thesis deals with Bose-Einstein condensates produced near the surface of a permanently magnetised film. The work emphasises the application of magnetic films for atom chip devices and highlights the future applications of ultracold atoms and Bose-Einstein condensates for profiling magnetic fields near surfaces and for sensing potential gradients on a small scale.

The work initially involved the development and characterisation of high quality perpendicularly magnetised GdTbFeCo films for the atom chip which is described in detail in Chapter 3. To attain sufficient magnetisation and thickness we deposited a multilayered film with excellent magnetic properties. To summarise: total GdTbFeCo thickness $\delta = 900$ nm, square shape hysteresis loop, remanent magnetisation $\mu_0 M_r = 0.278$ T, remanence ratio $M_r/M_s = 0.91$, coercivity $\mu_0 H_c = 0.320$ T, and an effective current of $I_{eff} = 0.2$ A. The magnetic film is combined with a machined silver-foil wire structure to form a hybrid atom chip that incorporates the flexibility of current-carrying wires with the unique advantages of permanent magnetic films. The wire structure designed to carry currents in excess of 30 A was produced in-house, using a commercial PCB milling machine which has proven to be a convenient method to rapidly develop atom chips at low cost.

To produce Bose-Einstein condensates it was necessary to construct an ultrahigh

vacuum apparatus, an optical system for laser cooling and a computer system for controlling the experiment. These technical aspects of the research are described in Chapter 4. This involved a single vacuum chamber design and and pulsed alkali metal dispensers as a rubidium source. The diode laser system is a relatively compact and robust scheme for constructing a mirror magneto-optical trap and is also used for optical imaging of the trapped atoms. The computer system and control software used for synchronising the experiment and for analysing the data is also described. Typically within minutes of turning on the laser system we can reliably produce Bose-Einstein condensates.

Chapter 5 describes the experimental stages required to produce a Bose-Einstein condensate using the atom chip. We collect 4×10^8 ^{87}Rb atoms in the mirror magneto-optical trap which are then transferred to the atom chip using the current-carrying wires. The polarisation gradient cooling and optical pumping stages prior to magnetic trapping are also described. A 10 s logarithmic radio frequency sweep is used to evaporatively cool the atoms to the BEC transition. Bose-Einstein condensates with $> 10^5$ atoms can be produced in the current-carrying wire magnetic trap or in the magnetic film microtrap, opening new possibilities for directly comparing the two types of traps. In particular we have observed heating rates as low as 3 nK/s for atom clouds in the magnetic film microtrap, two orders of magnitude lower than our own observations in the wire based trap. The BEC is then used as a probe to characterise the field of the film through measurements of the centre of mass oscillation frequencies and the cloud position as a function of B_{bias}

One of the most dramatic findings of this work is the observation of small magnetic field variations produced near the film surface that corrugate the trapping potential. This became the topic of Chapter 6, a comprehensive study on the homogeneity of the magnetic film which involved the use of ultracold atoms as a sensitive, high resolution magnetic field probe. The technique of spatially resolved radio frequency spectroscopy has been developed to accurately map the magnetic field variations and can be compared with independent measurements utilising a magneto-resistive

probe. In addition, an analytic model which describes the effect of magnetisation inhomogeneity on magnetic microtraps is in good agreement with our experimental results, and serves as a tool for assessing the quality of magnetic materials for atom chips.

Armed with a detailed map of the magnetic field landscape we shifted our attention to one region of the film where the corrugation forms a double-well potential. In Chapter 7 we show how the parameters of the double well such as the well separation and the barrier height can be precisely controlled by moving the atoms with respect to the surface. It is demonstrated that a single BEC can be adiabatically split using the double well and the relative population of atoms in each well is a measure of the potential asymmetry The extremely narrow energy distribution of a BEC is ideal for detecting minute magnetic field gradients or changes in gravity with a spatial resolution on the micron scale. We have demonstrated an equivalent sensitivity in the $\frac{\delta g}{g} \approx 1 \times 10^{-4}$ regime over a 70 μm area. Straight-forward extensions of the technique may make measurements in the 1×10^{-7} regime possible. The method is non-interferometric in nature and does not suffer from the problems that currently limit the practical use of integrated BEC interferometers.

8.2 Future directions

Combining magnetic films with microwires. The next generation of atom chips will incorporate more complex structures for manipulating ultracold atoms and may combine patterned magnetic films, microfabricated wires and optical potentials near the chip surface. Truly integrated devices will require all trapping fields to be produced on the atom chip itself to avoid the use of external bias magnetic fields. We are currently designing dual layer atom chips incorporating a patterned magnetic film layer with a microfabricated surface of gold conductors. The patterned magnetic film provides the overall confining potential while small current flow through the conductors will be used to manipulate the potential in a time dependent manner. This type of dual layer atom chip may have promising applications when combined with rf induced dressed state

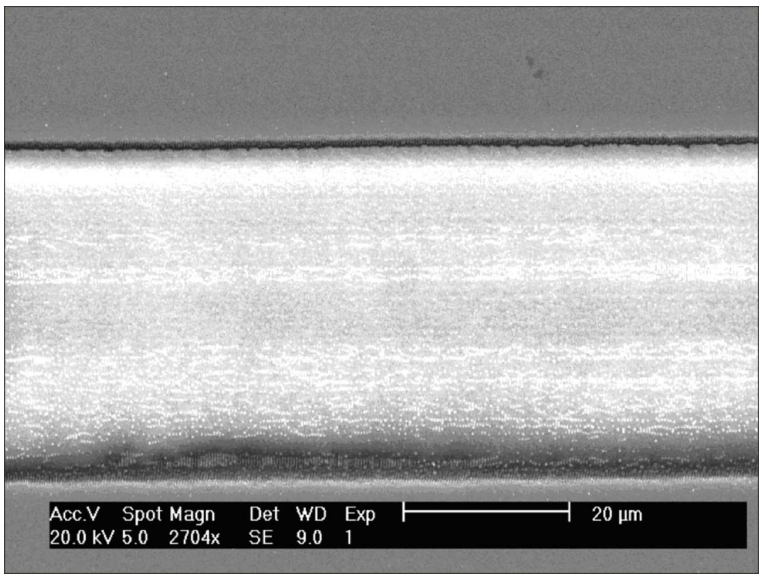

Fig. 8.1: Scanning electron micrograph of a 40 μm channel patterned in a 100 nm thick GdTbFeCo magnetic film using femtosecond laser ablation. The magnetic material (dark grey) is removed cleanly with minimal damage to the glass substrate (light grey) and the film edge is smooth and without debris.

potentials, a technique already used to perform double-well atom interferometry [15,98].

A novel approach for fabricating atom chips is femtosecond laser ablation of metals (Figure 8.1). Our apparatus uses pulses of 100 fs duration at 400 nm to pattern metal in a vacuum environment The ablation threshold depends strongly on the material and is significantly lower for gold as compared to GdTbFeCo. For high pulse energies both the gold and GdTbFeCo layers are ablated while for lower pulse energies we expect to selectively ablate the gold layer without damaging the GdTbFeCo underlayer, to produce a dual layer structure. Femtosecond laser patterning has the potential to produce elements with sub-micron feature sizes, high aspect ratios and smooth edges, with minimal damage to the surrounding areas to create intricate trapping potentials. This technique provides a high level of flexibility and convenience to rapidly produce arbitrary trapping geometries, faster and cheaper than conventional lithographic techniques.

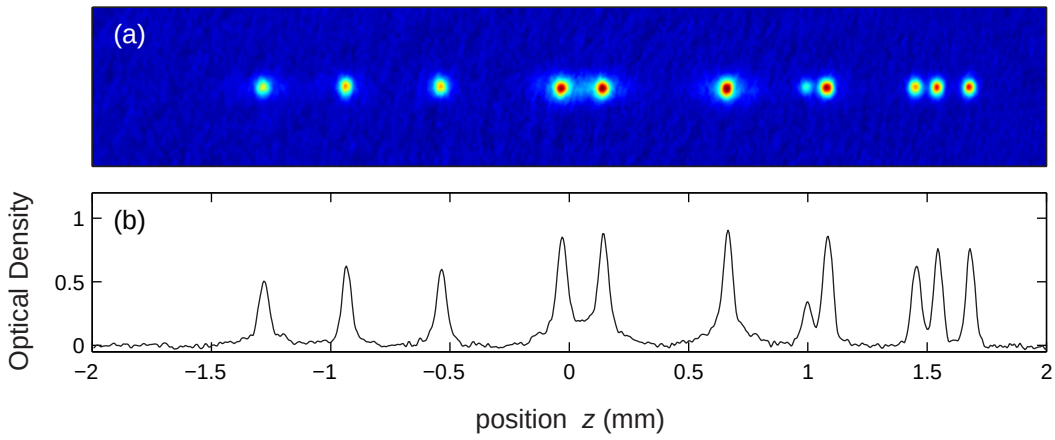

Fig. 8.2: (Colour) An array of 11 Bose-Einstein condensates simultaneously produced in the random potential created by the magnetic film. The absorption image (a) is recorded after 15 ms of ballistic expansion. (b) Density profiles taken along the axis of the array.

Arrays of Bose-Einstein condensates. An important application for permanent magnet atom chips is the realisation of large arrays of microtraps. While Bose-Einstein condensates have already been produced using periodic magnetic structures [26, 31], these structures have not yet been exploited to realise an array of Bose-Einstein condensates. In our work we have shown how the corrugated magnetic potential caused by magnetisation inhomogeneity may be used to produce multiple Bose-Einstein condensates in a linear array (Figure 8.2). Recent theoretical proposals have also highlighted the possibility of creating two-dimensional arrays of microtraps using permanent magnet structures [99, 100]. Such structures with small enough periods should allow for interesting quantum tunnelling experiments, and by varying the barrier heights (for example by tuning the distance from the surface) it may be possible to realise the BEC-superfluid to Mott-insulator phase transition [101]. Arrays of permanent magnet microtraps have potentially important implications for proposals of quantum information processing using neutral atoms.

Sensing forces on the micrometer scale. The most immediate practical application of Bose-Einstein condensates is toward metrology and precision sensing of small forces on a small spatial scale. This is already gaining wide-spread interest with a number

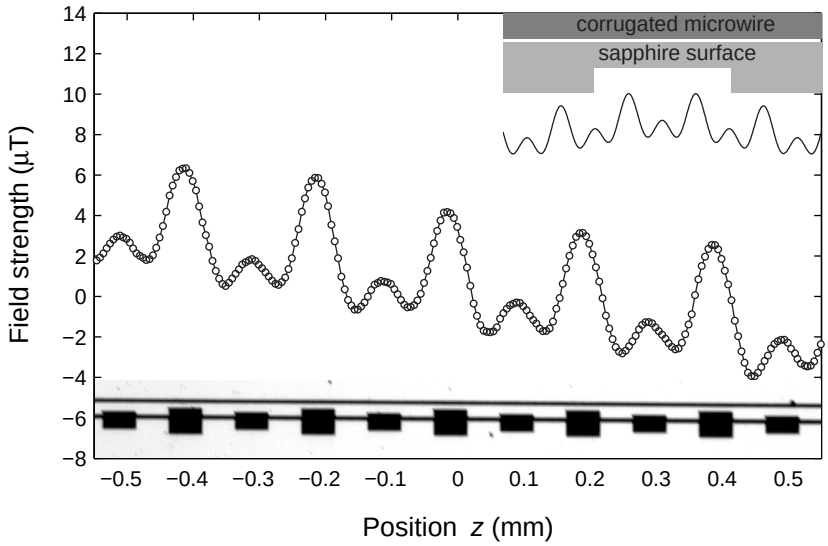

Fig. 8.3: Scanning magneto-resistance scan of a magnetic double well array. The double-well potentials are formed by corrugating a gold current carrying wire using the femtosecond laser ablation method. The lower inset is an optical microscope image of the wire structure where the insulating grooves show up as black. The upper inset shows how the Casimir-Polder attractive potential produced by a structured surface affects the symmetry of the potentials and may be precisely measured using the double-well sensor.

of BEC experiments [78, 102, 103] but may be even more powerful in combination with atom chips to precisely control the position of a BEC near a surface [14, 83, 95]. An obvious extension to the work in this thesis is to apply the double-well sensor studied in Chapter 7 to sense potential gradients close to the atom chip surface. One may conceive a simple structured surface to investigate the potential produced by the Casimir-Polder force or ultimately search for non Newtonian gravitational forces within a few micrometers of a surface [94]. To improve the sensitivity of our scheme we are currently fabricating arrays of double well potentials by corrugating a current-carrying wire (Figure 8.3) using femtosecond laser ablation. Further improvements to the sensitivity of this technique may be obtained by reducing atomic shot-noise through atom number squeezing, an effect recently observed in a similar double-well system [98].

Bibliography

[1] E. A. Cornell and C. E. Wieman, "Nobel lecture: Bose-Einstein condensation in a dilute gas, the first 70 years and some recent experiments," *Rev. Mod. Phys.*, vol. **74**, pp. 875–893, 2002.

[2] W. Ketterle, "Nobel Lecture: When atoms behave as waves: Bose-Einstein condensation and the atom laser," *Rev. Mod. Phys.*, vol. **74**, pp. 1131–1151, 2002.

[3] J. D. Weinstein and K. G. Libberecht, "Microscopic magnetic traps for neutral atoms," *Phys. Rev. A*, vol. **52**, pp. 4004–4009, 1995.

[4] J. Reichel, W. Hänsel, and T. W. Hänsch, "Atomic micromanipulation with magnetic surface traps," *Phys. Rev. Lett.*, vol. **83**, pp. 3398–4301, 1999.

[5] R. Folman, P. Krüger, D. Cassettari, B. Hessmo, T. Maier, and J. Schmiedmayer, "Controlling cold atoms using nanofabricated surfaces: atom chips," *Phys. Rev. Lett.*, vol. **84**, pp. 4749–4752, 2000.

[6] W. Hänsel, P. Hommelhoff, T. W. Hänsch, and J. Reichel, "Bose-Einstein condensation on a microelectronic chip," *Nature Physics*, vol. **413**, p. 498, 2001.

[7] H. Ott, J. Fortágh, G. Schlotterbeck, A. Grossmann, and C. Zimmermann, "Bose-Einstein condensation in a surface microtrap," *Phys. Rev. Lett.*, vol. **87**, p. 230401, 2001.

[8] A. E. Leanhardt, A. P. Chikkatur, D. Kielpinski, Y. Shin, T. L. Gustavson, W. Ketterle, and D. E. Pritchard, "Propagation of Bose-Einstein condensates in a magnetic waveguide," *Phys. Rev. Lett.*, vol. **89**, p. 040401, 2002.

[9] P. Hommelhoff, W. Hänsel, T. Steinmetz, T. W. Hänsch, and J. Reichel, "Transporting, splitting and merging of atomic ensembles in a chip trap," *New. J. Phys.*, vol. **7**, p. 3, 2005.

[10] A. Günther, M. Kemmler, S. Kraft, C. J. Vale, C. Zimmermann, and J. Fortágh, "Combined chips for atom optics," *Phys. Rev. A*, vol. **71**, p. 063619, 2005.

[11] S. Du, M. B. Squires, Y. Imai, L. Czaia, R. A. Saravanan, V. Bright, J. Reichel, T. W. Hänsch, and D. Z. Anderson, "Atom-chip Bose-Einstein condensation in a portable vacuum cell," *Phys. Rev. A*, vol. **70**, p. 053606, 2004.

[12] S. Aubin, S. Myrskog, M. H. T. Extavour, L. J. LeBlanc, D. McKay, A. Stummer, and J. H. Thywissen, "Rapid sympathetic cooling to Fermi degeneracy on a chip," *Nature Physics*, vol. **2**, pp. 384–387, 2006.

[13] I. Teper, Y.-J. Lin, and V. Vuletić, "Resonator-aided single-atom detection on a microfabricated chip," *Phys. Rev. Lett.*, vol. **97**, p. 023002, 2006.

[14] S. Wildermuth, S. Hofferberth, I. Lesanovsky, E. Haller, L. M. Andersson, S. Groth, I. Bar-Joseph, P. Krüger, and J. Schmiedmayer, "Bose-Einstein condensates: microscopic magnetic field imaging," *Nature Physics*, vol. **435**, p. 440, 2005.

[15] T. Schumm, S. Hofferberth, L. M. Andersson, S. Wildermuth, S. Groth, I. Bar-Joseph, J. Schmiedmayer, and P. Krüger, "Matter wave interferometry in a double well on an atom chip," *Nature Physics*, vol. **1**, p. 57, 2005.

[16] Y. Shin, C. Sanner, G. B. Jo, T. A. Pasquini, M. Saba, W. Ketterle, D. E. Pritchard, M. Vengalattore, and M. Prentiss, "Interference of Bose Einstein condensates split with an atom chip," *Phys. Rev. A*, vol. **72**, p. 021604(R), 2005.

[17] J. Fortágh, H. Ott, S. Kraft, A. Günther, and C. Zimmermann, "Surface effects in magnetic microtraps," *Phys. Rev. A*, vol. **66**, p. 041604, 2002.

[18] D.-W. Wang, M. D. Lukin, and E. Demler, "Disordered Bose-Einstein condensates in quasi-one-dimensional magnetic microtraps," *Phys. Rev. Lett.*, vol. **92**, p. 076802, 2004.

[19] J. Estève, C. Aussibal, T. Schumm, C. Figl, D. Mailly, I. Bouchoule, C. I. Westbrook, and A. Aspect, "Role of wire imperfections in micromagnetic traps for atoms," *Phys. Rev. A*, vol. **70**, p. 043629, 2004.

[20] P. Krüger, L. M. Andersson, S. Wildermuth, S. Hofferberth, E. H. S. Aigner, S. Groth, I. Bar-Joseph, and J. Schmiedmayer, "Disorder potentials near lithographically fabricated atom chips," *preprint cond-mat/0504686*, 2004.

[21] L. D. Pietra, S. Aigner, C. vom Hagen, S. Groth, I. Bar-Joseph, H. J. Lezec, and J. Schmiedmayer, "Designing potentials by sculpturing wires," *preprint cond-mat/0604619*, 2006.

[22] J.-B. Trebbia, C. L. Garrido Alzar, R. Cornelussen, C. I. Westbrook, and I. Bouchoule, "Roughness supression in an AC atom chip," *preprint quant-ph/0701207*, 2007.

[23] C. Henkel, S. Pötting, and M. Wilkens, "Loss and heating of particles in small and noisy traps," *Appl. Phys. B*, vol. **69**, pp. 379–387, 1999.

[24] M. P. A. Jones, C. J. Vale, D. Sahagun, B. V. Hall, and E. A. Hinds, "Spin coupling between cold atoms and the thermal fluctuations of a metal surface," *Phys. Rev. Lett.*, vol. **91**, p. 080401, 2003.

[25] V. Dikovsky, Y. Japha, C. Henkel, and R. Folman, "Reduction of magnetic noise in atom chips by material optimization," *Eur. Phys. J. D*, vol. **35**, pp. 87–95, 2005.

[26] C. D. J. Sinclair, J. A. Retter, E. A. Curtis, B. V. Hall, I. L. Garcia, S. Eriksson, B. E. Sauer, and E. A. Hinds, "Cold atoms in videotape micro-traps," *Eur. Phys. J. D*, vol. **35**, pp. 105–110, 2005.

[27] C. D. J. Sinclair, E. A. Curtis, I. L. Garcia, J. A. Retter, B. V. Hall, S. Eriksson, B. E. Sauer, and E. A. Hinds, "Bose-Einstein condensation on a permanent-magnet atom chip," *Phys. Rev. A*, vol. **72**, p. 031603R, 2005.

[28] B. V. Hall, S. Whitlock, F. Scharnberg, P. Hannaford, and A. Sidorov, "Bose-Einstein condensates on a permanent magnetic film atom chip," in *Laser Spectroscopy XVII* (E. A. Hinds, A. Ferguson, and E. Riis, eds.), World Scientific, Singapore, 2005. Online version available at cond-mat/0509091.

[29] B. V. Hall, S. Whitlock, F. Scharnberg, P. Hannaford, and A. Sidorov, "A permanent magnetic film atom chip for Bose-Einstein condensation," *J. Phys. B: At. Mol. Opt. Phys.*, vol. **39**, p. 27, 2006.

[30] J. Y. Wang, S. Whitlock, F. Scharnberg, D. S. Gough, A. I. Sidorov, R. J. McLean, and P. Hannaford, "Perpendicularly magnetized, grooved GdTbFeCo microstructures for atom optics," *J. Phys. D: Appl. Phys.*, vol. **38**, pp. 4015–4020, 2005.

[31] M. Boyd, E. W. Streed, P. Medley, G. K. Campbell, J. Mun, W. Ketterle, and D. E. Pritchard, "Atom trapping with a thin magnetic film," *preprint cond-mat/0608370*, 2006.

[32] A. Jaakkola, A. Shevchenko, K. Lindfors, M. Hautakorpi, E. Il'yashenko, T. H. Johansen, and M. Kaivola, "Reconfigurable atom chip on a transparent ferrite-garnet film," *Eur. Phys. J. D*, vol. **35**, p. 81, 2005.

[33] M. Vengalattore, R. S. Conroy, W. Rooijakkers, and M. Prentiss, "Ferromagnets for integrated atom optics," *J. Appl. Phys.*, vol. **95**, pp. 4404–4407, 2004.

[34] W. Paul, "Electromagnetic traps for charged and neutral particles," *Rev. Mod. Phys.*, vol. **62**, pp. 531–540, 1990.

[35] A. L. Migdall, J. V. Prodan, W. D. Phillips, T. H. Bergeman, and H. J. Metcalf, "First observation of magnetically trapped neutral atoms," *Phys. Rev. Lett.*, vol. **54**, pp. 2596–2599, 1985.

[36] H. J. Metcalf and P. van der Straten, *Laser cooling and trapping*. Springer, New York, 1999.

[37] T. Bergeman, G. Erez, and H. Metcalf, "Magnetostatic trapping fields for neutral atoms," *Phys. Rev. A*, vol. **35**, pp. 1535–1546, 1987.

[38] W. Ketterle, D. S. Durfee, and D. M. Stamper-Kurn, "Making, probing and understanding Bose-Einstein condensates," in *Bose-Einstein condensation in atomic gases, Proceedings of the International School of Physics "Enrico Fermi", Course CXL* (M. Inguscio, S. Stringari, and C. E. Wieman, eds.), pp. 67–176, IOS Press, Amsterdam, 1999. Online version available at cond-mat/9904034.

[39] T. H. Bergeman, P. McNicholl, J. Kycla, H. Metcalf, and N. L. Balazs, "Quantized motion of atoms in a quadrupole magnetostatic trap," *J. Opt. Soc. Am. B*, vol. **6**, pp. 2249–2256, 1989.

[40] K. B. Davis, M.-O. Mewes, M. A. Joffe, M. R. Andrews, and W. Ketterle, "Evaporative cooling of sodium atoms," *Phys. Rev. Lett.*, vol. **74**, pp. 5202–5205, 1995.

[41] W. Petrich, M. H. Anderson, J. R. Ensher, and E. A. Cornell, "Stable, tightly confining magnetic trap for evaporative cooling of neutral atoms," *Phys. Rev. Lett.*, vol. **74**, pp. 3352–3355, 1995.

[42] D. S. Naik, S. R. Muniz, and C. Raman, "Metastable Bose-Einstein condensate in a linear potential," *Phys. Rev. A*, vol. **72**, p. 051606(R), 2005.

[43] D. E. Pritchard, "Cooling neutral atoms in a magnetic trap for precision spectroscopy," *Phys. Rev. Lett.*, vol. **51**, pp. 1336–1339, 1989.

[44] C. V. Sukumar and D. M. Brink, "Spin-flip transitions in a magnetic trap," *Phys. Rev. A*, vol. **56**, pp. 2451–2454, 1997.

[45] J. P. Burke Jr., J. L. Bohn, B. D. Esry, and C. H. Greene, "Prospects for mixed isotope Bose-Einstein condensates in rubidium," *Phys. Rev. Lett.*, vol. **80**, pp. 2097–2100, 1998.

[46] S. Bali, K. M. O'Hara, M. E. Gehm, S. R. Granade, and J. E. Thomas, "Quantum-diffractive background gas collisions in atom-trap heating and loss," *Phys. Rev. A*, vol. **60**, pp. R29–R32, 1999.

[47] J. Södin, D. Guèry-Odelin, P. Desbiolles, F. Chevy, H. Inamori, and J. Dalibard, "Three-body decay of a rubidium Bose-Einstein condensate," *Appl. Phys. B*, vol. **69**, pp. 257–261, 1999.

[48] E. A. Burt, R. W. Ghrist, C. J. Myatt, M. J. Holland, E. A. Cornell, and C. E. Wieman, "Coherence, correlations, and collisions: what one learns about Bose-Einstein condensates from their decay," *Phys. Rev. Lett.*, vol. **79**, pp. 337–340, 1997.

[49] E. A. Cornell, J. R. Ensher, and C. E. Wieman, "Experiments in dilute atomic Bose-Einstein condensation," in *Bose-Einstein condensation in atomic gases, Proceedings of the International School of Physics 'Enrico Fermi', Course CXL* (M. Inguscio, S. Stringari, and C. E. Wieman, eds.), pp. 15–66, IOS Press, Amsterdam, 1999. Online version available at cond-mat/9903109.

[50] A. Haase, D. Cassettari, B. Hessmo, and J. Schmiedmayer, "Trapping neutral atoms with a wire," *Phys. Rev. A*, vol. **64**, p. 043405, 2001.

[51] R. Folman, P. Krüger, J. Schmiedmayer, J. Denschlag, and C. Henkel, "Microscopic atom optics: from wires to an atom chip," *Adv. At. Mol. Opt. Phys.*, vol. **48**, p. 263, 2002.

[52] J. Fortágh and C. Zimmermann, "Magnetic microtraps for ultracold atoms," *Rev. Mod. Phys.*, vol. **79**, pp. 235–289, 2007.

[53] A. I. Sidorov, R. J. McLean, F. Scharnberg, D. S. Gough, T. J. Davis, B. A. Sexton, G. I. Opat, and P. Hannaford, "Permanent magnet microstructures for atom optics," *Acta Phys. Pol. B*, vol. **33**, pp. 2137–2155, 2002.

[54] J. D. Jackson, *Classical electrodynamics, 3rd Edition.* John Wiley and Sons, New York, 1998.

[55] F. Dalfovo, S. Giorgini, L. P. Pitaevskii, and S. Stringari, "Theory of Bose-Einstein condensation in trapped gases," *Rev. Mod. Phys.*, vol. **71**, pp. 463–512, 1999.

[56] C. J. Pethick and H. Smith, *Bose-Einstein condensation in dilute gases.* Cambridge University Press, Cambridge, 2001.

[57] L. P. Pitaevskii and S. Stringari, *Bose-Einstein condensation.* Clarendon Press, Oxford, 2003.

[58] W. Ketterle and N. J. van Druten, "Bose-Einstein condensation of a finite number of particles trapped in one or three dimensions," *Phys. Rev. A*, vol. **54**, pp. 656–660, 1996.

[59] M. H. Kryder, "Magneto-optical storage materials," *Annu. Rev. Mater. Sci.*, vol. **23**, pp. 411–436, 1993.

[60] C. J. Vale, B. Upcroft, M. J. Davis, N. R. Heckenberg, and H. Rubinsztein-Dunlop, "Foil-based atom chip for Bose-Einstein condensates," *J. Phys. B: At. Mol. Opt. Phys.*, vol. **37**, pp. 2959–2967, 2004.

[61] P. Chaudhari, J. J. Cuomo, and R. J. Gambino, "Amorphous metallic films for magneto-optic applications," *Appl. Phys. Lett.*, vol. **22**, pp. 337–339, 1973.

[62] B. R. Brown, "Optical data storage potential of six materials," *Appl. Opt.*, vol. **13**, pp. 761–766, 1974.

[63] S. Tsunashima, "Magneto-optical recording," *J. Phys. D: Appl. Phys.*, vol. **34**, pp. R87–R102, 2001.

[64] R. J. Gambino and T. Suzuki, *Magneto-optical recording materials.* John Wiley and Sons, New York, 1997.

[65] M. H. Kryder, H.-P. Shieh, and D. K. Hairston, "Control of parameters in rare earth-transition metal alloys for magneto-optical recording media," *IEEE. Trans. Magn.*, vol. **23**, pp. 165–167, 1987.

[66] F. Scharnberg, *Bose-Einstein condensation in micro-potentials for atom interferometry.* PhD thesis, Swinburne University of Technology, 2007.

[67] C. P. Pearman, C. S. Adams, S. G. Cox, P. F. Griffin, D. A. Smith, and I. G. Hughes, "Polarization spectroscopy of a closed atomic transition: applications to laser frequency locking," *J. Phys. B: At. Mol. Opt. Phys.*, vol. **35**, pp. 5141–5151, 2002.

[68] D. A. Steck, "Rubidium 87 D Line data," 2001. available online at http://steck.us/alkalidata.

[69] A. S. Arnold, *Preparation and manipulation of an* ^{87}*Rb Bose-Einstein condensate.* PhD thesis, University of Sussex, 1999.

[70] C. J. Dedman, K. G. H. Baldwin, and M. Colla, "Fast switching of magnetic fields in a magneto-optic trap," *Rev. Sci. Inst.*, vol. **72**, pp. 4055–4058, 2001.

[71] K. Lindquist, M. Stephens, and C. Wieman, "Experimental and theoretical study of the vapor-cell Zeeman optical trap," *Phys. Rev. Lett.*, vol. **46**, pp. 4082–4090, 1992.

[72] J. Fortágh, A. Grossmann, T. W. Hänsch, and C. Zimmermann, "Fast loading of a magneto-optical trap from a pulsed thermal source," *J. Appl. Phys.*, vol. **84**, pp. 6499–6501, 1998.

[73] J. Dalibard and C. Cohen-Tannoudji, "Laser cooling below the Doppler limit by polarization gradients: simple theoretical models," *J. Opt. Soc. Am: B*, vol. **6**, pp. 2023–2045, 1989.

[74] W. Ketterle and N. J. van Druten, *Advances in Atomic Molecular and Optical Physics*, vol. **37**, ch. Evaporative cooling of atoms, pp. 181–236. Academic Press, New York, 1996.

[75] J. Reichel, "Microchip traps and Bose-Einstein condensation," *Appl. Phys. B*, vol. **75**, pp. 469–487, 2002.

[76] M. Yamashita, M. Koashi, T. Mukai, M. Mitsunaga, N. Imoto, and T. Mukai, "Optimization of evaporative cooling towards a large number of Bose-Einstein-condensed atoms," *Phys. Rev. A*, vol. **67**, p. 023601, 2003.

[77] T. Mukai and M. Yamashita, "Efficient rapid production of a Bose-Einstein condensate by overcoming serious three-body loss," *Phys. Rev. A*, vol. **70**, p. 013615, 2004.

[78] D. M. Harber, J. M. Obrecht, J. M. McGuirk, and E. A. Cornell, "Measurement of the Casimir-Polder force through center-of-mass oscillations of a Bose-Einstein condensate," *Phys. Rev. A*, vol. **72**, p. 033610, 2005.

[79] S. Whitlock, R. Anderson, B. V. Hall, P. Hannaford, and A. I. Sidorov, "Bose-Einstein condensates on a permanent magnetic film atom chip," *The Physicist*, vol. **43**-1, p. 8, 2006.

[80] S. Whitlock, B. V. Hall, T. Roach, R. Anderson, M. Volk, P. Hannaford, and A. I. Sidorov, "Effect of magnetisation inhomogeneity on magnetic microtraps for atoms," *Phys. Rev. A*, vol. **75**, p. 043602, 2007.

[81] S. Kraft, A. A. Günther, H. Ott, D. Wharam, C. Zimmermann, and J. Fortágh, "Anomalous longitudinal magnetic field near the surface of copper conductors," *J. Phys. B: At. Mol. Opt. Phys.*, vol. **35**, p. L469, 2002.

[82] A. E. Leanhardt, Y. Shin, A. P. Chikkatur, D. Kielpinski, W. Ketterle, and D. E. Pritchard, "Bose-Einstein condensates near a microfabricated surface," *Phys. Rev. Lett.*, vol. **90**, p. 100404, 2003.

[83] Y.-J. Lin, I. Teper, C. Chin, and V. Vuletić, "Impact of the Casimir-Polder potential and Johnson noise on Bose-Einstein condensate stability near surfaces," *Phys. Rev. Lett.*, vol. **92**, p. 050404, 2004.

[84] A. G. Martin, K. Helmerson, V. S. Bagnato, G. P. Lafyatis, and D. E. Pritchard, "rf spectroscopy of trapped neutral atoms," *Phys. Rev. Lett.*, vol. **61**, pp. 2431–2434, 1988.

[85] K. Helmerson, A. Martin, and D. E. Pritchard, "Laser and rf spectroscopy of magnetically trapped neutral atoms," *J. Opt. Soc. Am. B: Opt. Phys.*, vol. **9**, pp. 483–492, 1992.

[86] I. Bloch, T. W. Hänsch, and T. Esslinger, "Atom laser with a cw output coupler," *Phys. Rev. Lett.*, vol. **82**, pp. 3008–3011, 1999.

[87] S. Gupta, Z. Hadzibabic, M. W. Zwierlein, C. A. Stan, K. Dieckmann, C. H. Schunch, E. G. M. van Kempen, B. J. Verhaar, and W. Ketterle, "rf spectroscopy of fermions," *Science*, vol. **300**, pp. 1723–1726, 2003.

[88] C. Chin, M. Bartenstein, A. Altmeyer, S. Riedl, S. Jochim, J. H. Denschlag, and R. Grimm, "Observation of the pairing gap in a strongly interacting Fermi gas," *Science*, vol. **305**, pp. 1128–1130, 2004.

[89] O. J. Luiten, M. W. Reynolds, and J. T. M. Walraven, "Kinetic theory of the evaporative cooling of a trapped gas," *Phys. Rev. A*, vol. **53**, pp. 381–389, 1995.

[90] J. S. Moodera, L. R. Kinder, T. M. Wong, and R. Meservey, "Large magnetoresistance at room temperature in ferromagnetic thin film tunnel junctions," *Phys. Rev. Lett.*, vol. **74**, pp. 3273–3276, 1995.

[91] K. F. Anderson, "The constant current loop: a new paradigm for resistance signal conditioning," *NASA technical memorandum*, vol. TM-104260, 1992.

[92] F. E. Luborsky, "Kinetics for changes in anisotropy, coercivity and argon content of TM-RE films," *J. Appl. Phys.*, vol. **57**, p. 3592, 1985.

[93] Y. J. Wang and Q. W. Leng, "Thermal stability and the origin of perpendicular anisotropy in amorphous Tb-Fe-Co films," *Phys. Rev. B*, vol. **41**, p. 651, 1990.

[94] S. Dimopoulos and A. A. Geraci, "Probing submicron forces by interferometry of Bose-Einstein condensed atoms," *Phys. Rev. D*, vol. **68**, p. 124021, 2003.

[95] B. V. Hall, S. Whitlock, R. Anderson, P. Hannaford, and A. I. Sidorov, "Condensate splitting in an asymmetric double well for atom chip based sensors," *Phys. Rev. Lett.*, vol. **98**, p. 030402, 2007.

[96] J. Fortágh, *Bose-Einstein kondensate in magnetischen mikrofallen.* PhD thesis, Eberhard Karls Universität Tübingen, 2003.

[97] A. I. Sidorov, B. J. Dalton, S. Whitlock, and F. Scharnberg, "Asymmetric double-well potential for single-atom interferometry," *Phys. Rev. A*, vol. **74**, p. 023612, 2006.

[98] G. B. Jo, Y. Shin, S. Will, T. A. Pasquini, M. Saba, W. Ketterle, D. E. Pritchard, M. Vengalattore, and M. Prentiss, "Long phase coherence time and number squeezing of two Bose-Einstein condensates on an atom chip," *preprint cond-mat/0608585*, 2006.

[99] S. Ghanbari, T. D. Kieu, A. Sidorov, and P. Hannaford, "Permanent magnetic lattices for ultracold atoms and quantum degenerate gases," *J. Phys. B: At. Mol. Opt. Phys.*, vol. **39**, pp. 847–860, 2006.

[100] R. Gerritsma and R. J. C. Spreeuw, "Topological constraints on magnetostatic traps," *Phys. Rev. A*, vol. **74**, p. 043405, 2006.

[101] M. Greiner, O. Mandel, T. Esslinger, T. W. Hänsch, and I. Bloch, "Quantum phase transition from a superfluid to a Mott insulator in a gas of ultracold atoms," *Nature Physics*, vol. **415**, pp. 39–44, 2002.

[102] I. Carusotto, L. Pitaevskii, S. Stringari, G. Modugno, and M. Inguscio, "Sensitive measurement of forces at the micron scale using Bloch oscillations of ultracold atoms," *Phys. Rev. Lett.*, vol. **95**, p. 093202, 2005.

[103] M. Vengalattore, J. M. Higbie, S. R. Leslie, J. Guzman, L. E. Sadler, and D. M. Stamper-Kurn, "High-resolution magnetometry with a spinor Bose-Einstein condensate," *preprint cond-mat/0612685*, 2006.

Publications of the Author

Contents of this thesis have been published in:

Chapter 3.

J. Y. Wang, S. Whitlock, F. Scharnberg, D. S. Gough, A. I Sidorov, R. J. McLean and P. Hannaford, "Perpendicularly magnetized, grooved GdTbFeCo microstructures for atom optics," *Journal of Physics D: Applied Physics*, vol. **38**, pp. 4015-4020 (2005).

Chapter 5.

B. V. Hall, S. Whitlock, F. Scharnberg, P. Hannaford and A. Sidorov, "Bose-Einstein condensates on a permanent magnetic film atom chip," in *Laser Spectroscopy XVII* (E. A. Hinds, A. Ferguson and E. Riis, eds.), World Scientific, Singapore, (2005). Online version available at cond-mat/0509091

B. V. Hall, S. Whitlock, F. Scharnberg, P. Hannaford and A. Sidorov, "A permanent magnetic film atom chip for Bose-Einstein condensation," *Journal of Physics B: Atomic, Molecular Optical Physics*, vol. **39**, pp. 27-36 (2006).

S. Whitlock, R. Anderson, B. V. Hall, P. Hannaford and A. I. Sidorov, "A permanent magnetic film atom chip for Bose-Einstein condensation," *The Physicist*, vol. **1**, no. 1, p. 8 (2006).

Chapter 6.

S. Whitlock, B. V. Hall, T. Roach, R. Anderson, M. Volk, P. Hannaford and A. I. Sidorov, "Effect of magnetisation inhomogeneity on magnetic microtraps for atoms," *Phys. Rev. A*, vol. **75**, p. 043602 (2007).

Chapter 7.

B. V. Hall, S. Whitlock, R. Anderson, P. Hannaford and A. I. Sidorov, "Condensate splitting in an asymmetric double well for atom chip based sensors," *Phys. Rev. Lett.*, vol. **98**, p. 030402 (2007).

Other publications of the author

A. I. Sidorov, B. J. Dalton, S. Whitlock and F. Scharnberg, "Asymmetric double-well potential for single-atom interferometry," *Physical Review A*, vol. **74**, p. 023612 (2006).

S. Whitlock, D. A. Forbes and M. A. Beasley, "UBRI photometry of globular clusters in the Leo group galaxy NGC 3379," *Monthly Notices of the Royal Astronomical Society*, vol. **345**, pp. 949-959 (2003).